FACULTY
OF MATHEMATICS
AND PHYSICS
Charles University

DOCTORAL THESIS

Artem Shelemin

Plasma polymers in the nanostructured and nanocomposite coatings

Department of Macromolecular Physics

Supervisor of the doctoral thesis: Prof. RNDr. Hynek Biederman, DrSc.

Study programme: Physics

Specialization: Biophysics, Chemical and Macromolecular Physics

Prague 2017

I declare that I carried out this doctoral thesis independently, and only with the cited sources, literature and other professional sources.

I understand that my work relates to the rights and obligations under the Act No. 121/2000 Coll., the Copyright Act, as amended, in particular the fact that the Charles University in Prague has the right to conclude a license agreement on the use of this work as a school work pursuant to Section 60 paragraph 1 of the Copyright Act.

In Prague, 18th of May 2017

Acknowledgments

In this part of the thesis, I would like to express my gratitude to people who helped and supported me during the PhD study.

I am thankful to my supervisor Prof. RNDr. Hynek Biederman, Dr.Sc. for sharing valuable knowledge and experience with experimental work. I am very indebted to Doc. Ing. Andrey Shukurov, PhD and Doc. RNDr. Ondřej Kylián, PhD for inestimable help and advice in the preparation of this thesis. I am very obliged to other members of our group: Dr. Jan Hanuš, Doc. Danka Slavínská CSc, Dr. Jaroslav Kousal and Dr. Pavel Solař who advised me on various aspects of work. Also, I would like to thank our young colleagues and good friends Ing. Mykhailo Vaidulych, Mgr. Daniil Nikitin, Mgr. Anna Kuzminova, Mgr. Pavel Pleskunov.

And finally, I am very grateful to my dear wife Svitlana for patience, understanding and resolute faith in me.

Název prace: Plazmové polymery v nanostrukturovaných a nanokompozitních vrstvách

Autor: Artem Shelemin

Katedra: Katedra makromolekulárni fyziky

Vedoucí doktorské práce: Prof. RNDr. Hynek Biederman, DrSc.

Abstract: V této práci jsou shrnuty výsledky dosažené během mého studia nanostrukturovaných a nanokompozitních vrstev plazmových polymerů. Bylo vyvinuto a studováno několik alternativních experimentálních postupů, které využívají plazmové technologie jak za sníženého tlaku (plynové agregační zdroje, depozice pod velkým úhlem), tak i za atmosférického tlaku (dielektrický bariérový výboj a plazmová tryska). V rámci práce byly připravovány nanočástice kovů a oxidů kovů Ti/TiOx a AlOx i nanočástice plazmových polymerů SiO-x(CH) a Nylon 6,6. Byla provedena podrobná charakterizace morfologie připravovaných povlaků pomocí metod AFM a SEM i jejich chemického složení, které bylo studováno pomocí metod XPS a FTIR.

Klíčová slova: plazmový polymer, nanočástice, tenká vrstva, nanostruktury

Title: Plasma polymers in the nanostructured and nanocomposite coatings

Author: Artem Shelemin

Department / Institute: Department of the Macromolecular Physics

Supervisor of the doctoral thesis: Prof. RNDr. Hynek Biederman, DrSc.

Abstract: The thesis represents the main results of my research work aimed to study nanostructured and nanocomposite films of plasma polymer. A few alternative experimental approaches were developed and investigated which ranged from low pressure (gas aggregation cluster sources and glancing angle deposition) to atmospheric pressure (dielectric barrier discharge and plasma jet) plasma processing. The metal/metal oxide Ti/TiO_x, AlO_x and plasma polymer SiO_x(CH), Nylon 6,6 nanoparticles were prepared. The analysis of morphology of deposited plasma polymer coatings was performed by AFM and SEM. The chemical composition of films was studied by XPS and FTIR.

Keywords: plasma polymer, nanoparticle, thin film, nanostructures

Contents

1. INTRODUCTION/ PREFACE

1.1. Plasma polymers and plasma polymerization processes

Plasma polymers were first mentioned in the end of the 19th and in the first half of the 20th century [1–6]. The first attempts of deliberate deposition of plasma polymer films were done by König and Brockers in the 1950s [7,8]. Later, Goodman, Bradley and Hames published their research where they showed that plasma polymers can be used as dielectric films in electrical devices [9,10]. These publications revealed the potential applicability of plasma polymers that attracted the interest of many scientific groups around the world to this field. The development of the plasma polymerization field is described in more detail in the monographies [11,12].

It is known that the initiation of the polymerization process takes place due to the interaction of monomer molecules with plasma. The plasma is a quasineutral medium containing free electrons, ions and neutral species. In this work, the non-equilibrium low temperature plasma has been used. The term 'non-equilibrium' indicates the significant difference in thermal state of particles. Due to the lower mass, the electrons almost do not lose their energy during collisions with bigger species. As a result, their temperature can reach ~10^4 K and higher while the neutral particles are maintained under about the room temperature. The low temperature plasma is characterized by a weak degree of ionization which means that the amount of charged particles is much smaller than that of neutrals (approximately 1 charged particle per million of neutrals).

The interaction of highly energetic electrons with monomer molecules induces different processes including excitation, ionization and dissociation. Since much less energy is required to break the chemical bonds in an organic molecule than to its ionization, the amount of free radicals in plasma volume is much higher than that of ions (up to 10^5). These activated organic species recombine between themselves and form disordered polymer networks. The chains in plasma polymer are short, very branched and interconnected with high amount of crosslinks. A large number of radicals may remain unreacted and it makes plasma polymer films sensitive to aging.

From the beginning of the research of plasma polymers, the numerous discussions were carried out about what kind of interactions between plasma and monomer is responsible for the initiation of plasma polymerization and growth of thin films. According to a pioneer work of William and Hayes [13], the collision of electrons with monomer molecules near a cathode region leads to the creation of ions which in turn intensively bombard the monomer molecules adsorbed on the surface of the cathode, thus activating them. The activated molecules then react with monomers and, in a result, polymer chains are created. On the other hand, Denaro [14] and Carchano [15] proposed that the activation of the monomer molecules occurs through their collisions with energetic electrons. Westwood [16] experimentally tested the influence of charged particles on the initial stage of plasma polymerization process and offered an idea that ions play the major role . In contrast to the above theories where the surface processes were considered as dominant, Poll et al. [17] assumed that the interaction of particles both on the surface and in the volume may contribute to the growth of polymer films and both strongly depend on the experimental conditions. This idea was then expanded by Lam et al. [18] and Tibbit et al. [19], who suggested a three step mechanism of plasma polymerization:

Initiation: $M + e \rightarrow 2R_1 + e$

Propagation: $R_n + M \rightarrow R_{n+1}$

Termination: $R_m + R_n \rightarrow P_{m+n}$ *or* $P_m + P_n$

(*M* – monomer molecule; *R* – radical; P – neutral molecule or polymer)

According to this model, the collision of the monomer molecule with energetic electron leads to the creation of free radicals both in the plasma volume and on adjacent surfaces. The addition of the monomer molecules to active centers leads to propagation of the polymer chain. The growth process of polymer continues until activated molecules will not recombine with each other. Taking into account the work of Poll et al., Yasuda and Hsu proposed even more complex model, which is schematically described in the Figure 1[18]. Besides the main steps mentioned above, plasma polymerization involves also the ablation processes which are induced by the continuous bombardment of the growing film by charged species from plasma. Ablated molecular fragments can be then reinitiated or simply removed from the gas phase by pumping.

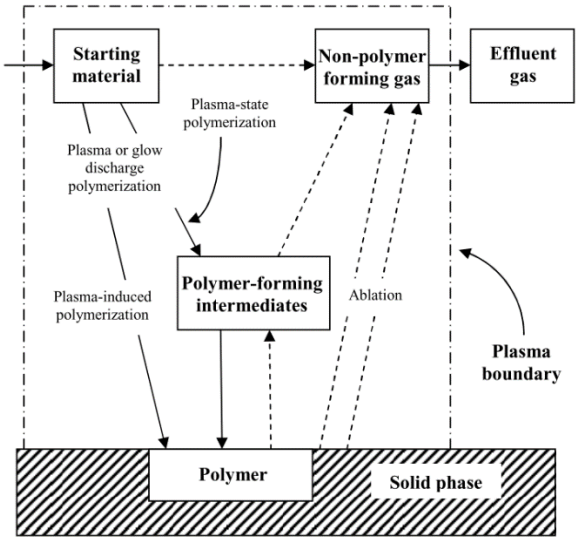

Figure 1. The scheme of the plasma polymerization process proposed by Yasuda and Hzu (*adapted from* [12]*).*

Yasuda also considered the multistep character of plasma polymerization. As evidenced in the Figure 2, he distinguished the contribution from mono and biradicals as main reactive species participating in the polymer growth. Here, the reaction a, d, e) corresponds to the propagation of polymer chain whereas b, c) reaction describe the possible mechanism of termination. More details can be learned from [12,20].

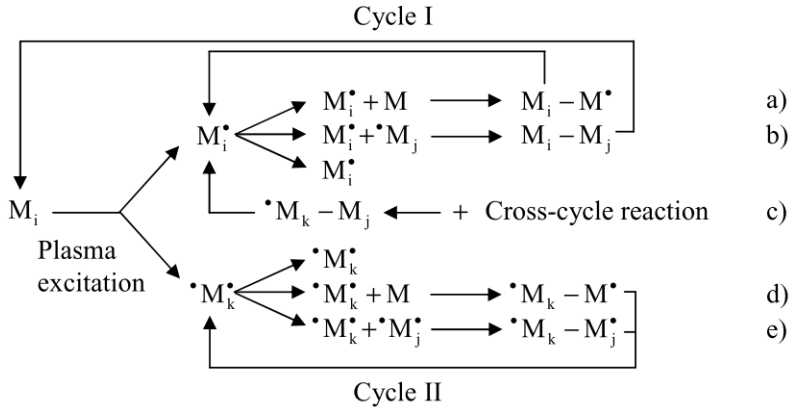

Figure 2. Multistep plasma polymerization process suggested by Yasuda. Here M• and •M• are mono- and difunctional molecules *(adapted from* [12]*).*

Originally, the deposition of plasma polymer films was performed under low pressure using liquid monomers as precursors. In this case, vapors of the precursor

are transported to the vacuum chamber with or without a flow of a carrier gas and undergo the influence of plasma. The number of possible monomers is quite large and mostly limited by their saturated vapor pressure. Plasma polymerization can be carried out with different configuration of experimental setups including the reactors with internal electrodes, with external electrodes or electrodeless (microwave) systems.

An alternative method of the fabrication of plasma polymer films was introduced in the 1970s. It is based on radio frequency (RF) magnetron sputtering of a polymer target. The sputtering procedure usually takes place under the relatively low pressure of few Pa in the atmosphere of inert (Ar, He) or reactive gases (N_2, H_2). The deposition of plasma polymer films by RF sputtering is also compatible with other low pressure based techniques especially with magnetron sputtering of metals which can be employed for the deposition of composite thin films [21–23]. The first sputtered polymer was polytetrafluorethylene (PTFE) [24]. Due to the good thermal stability, high dielectric strength and low friction coefficient, thin films of sputtered PTFE were considered very perspective for many applications. PTFE-sputtered thin films were probably the most studied plasma polymers prepared using RF sputtering [25–33]. Polyethylene [25,34], polypropylene [35], polyisobuthylene [36], polyimide [37], polydimethylsiloxane [38] and nylon 6.6 [39,40] were also studied. A certain disadvantage of RF magnetron sputtering of polymers is related to their bad thermal conductivity which can lead to overheating of the polymeric target under high applied power. The long exploitation of the target under such conditions can induce the degradation of the polymer and even the damage of the material.

Another deposition method of plasma polymer films is atmospheric pressure plasma polymerization. Low cost, the possibility to operate in the ambient air, easy scale-up and in-line capabilities are the main advantages of atmospheric discharges [41–43]. This technique has become popular in the industry, mostly for the surface treatment purposes. In the last decade, the possibility to use the atmospheric pressure plasma as a deposition method was intensively studied. Among the different sources of atmospheric plasma, dielectric barrier discharge (DBD) and plasma jet are probably most thoroughly investigated. The dielectric barrier discharge is initiated between two metal electrodes separated by an insulating barrier. According to the geometrical shape of the dielectric material, the planar and cylindrical configurations of DBD are distinguished (Figure 3).

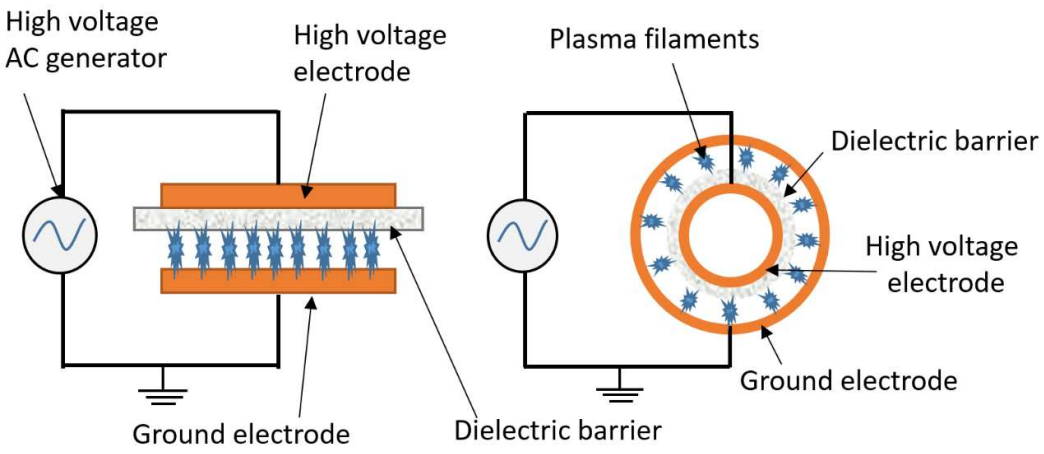

Figure 3. Planar (left picture) and cylindrical (right picture) configuration of dielectric barrier discharge.

The particular property of this discharge is the filamentary character of plasma which influences the properties of prepared coatings. This obstacle can be overcome by using helium as a carrier gas. Due to the high energy and long lifetime of metastable states of He atoms it is possible to obtain the diffusive glow discharge under the atmospheric pressure. The range of coatings prepared by atmospheric pressure plasma is quite large and continuously increases. SiO_2 [44,45] and TiO_2 thin films [46,47] are the most studied inorganic coatings. Among polymeric films obtained by DBD, polyethylene [48], C_xH_y from acytelene [49], polystyrene [50], polymethyl methacrylate [51,52] and PTFE-like [53,54] films can be distinguished.

In contrast to DBD, plasma jet has much more in common with the low pressure glow discharge. It is characterized by low breakdown voltage (0.05-0.2 kV) and relatively high density of charged species (10^{11} – 10^{12} cm^{-3}) [55]. The typical design of the plasma jet consists of a tubular reactor equipped with two electrodes. The application of the RF power to the active electrode induces the ignition of plasma. The high flow rate of the carrier gas through the reactor extracts the ionized gas to the work zone. The homogeneity of plasma mainly depends on the power, the nature and the flow of the carrier gas. There are two main experimental approaches of the preparation of thin films by means of atmospheric pressure plasma jet. The first one uses the precursor in the gaseous state and it was applied for the deposition of siloxane-based [56,57], nitrogen-rich coatings [58,59], fullerenes [60], fluorocarbon [61] and hydrocarbon coatings [62]. The second approach is based on

the utilization of the monomer in the liquid form. For example, Stallard et al. used a nebulizer as a feeding system for the deposition of siloxane-based and polyethylenglycol coatings [63,64]. The possibility to use liquid precursors significantly increases the choice of substances and enables to use such of them which poorly vaporize under normal conditions.

1.2. Gas phase formation of nanoparticles

The range of nanoparticles (NPs) application is really impressive and covers different scientific fields [65–71]. Therefore, the search for a low cost, environmentally friendly deposition method providing also a high production rate is a very actual task in the 21st century. One of the very promising techniques of the NPs deposition is a Gas Aggregation Cluster Source (GAS).

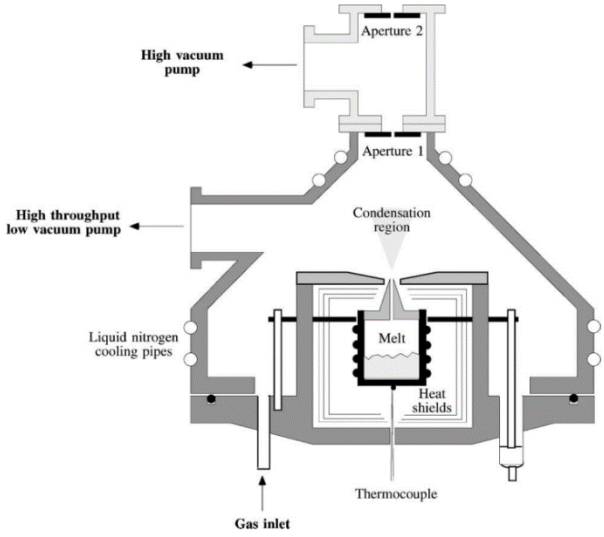

Figure 4. Sattler cluster source (*adapted from* [72]).

A first prototype of the GAS (please see Figure 4) was built by Sattler et al. [73] in 1980. Thermal evaporation was applied to vaporize the tested material. A thermally isolated crucible was fixed in an aggregation chamber cooled with liquid nitrogen and fed with an inert gas of He at high pressure (~100 Pa). Cooling of metal vapors by the carrier gas creates the conditions for supersaturation and leads to the vapor condensation with the formation of nuclei of metallic NPs. The nuclei may

then grow by incorporating more metal atoms from the gas phase or they may disintegrate by releasing atoms from the condensed to the gaseous state. The stability of a nucleus is ruled by the energetic balance between the two processes and described by a thermodynamic parameter known as Kelvin diameter or critical diameter [68].

Further development of the particle structure strongly depends on the density of a nucleus, pressure of inert gas and temperature [74]. The later stage of the NP formation may include the coalescence, by which individual NPs aggregate into a single bigger particle, or coagulation, by which agglomerations of individual NPs are formed.

In the work of Satler, the NPs were formed in the volume above the evaporation source of the material by condensation on the cold He gas and were drawn by the flow of He to a high vacuum chamber connected with a time-of-flight (TOF) spectrometer. The authors were able to obtain the intensive deposition rate and to observe for the first time its dependence on the inert gas inside the aggregation chamber. Since that time, many different cluster sources utilizing evaporation, magnetron sputtering, laser vaporization, arc discharge etc. have been developed [68,72]. Probably, one of the most frequently used of them is the magnetron-based cluster source firstly designed by Haberland et al. in the 1990s [75–77]. The application of low temperature plasma generated by magnetron sputtering also allows to supply metallic vapors into the gas phase where they nucleate. The interaction of NPs with plasma leads to their charging which allows one to manipulate them by the application of the electric field. It was shown that metallic NPs can be size separated in accord with their mass-to-charge ratio.

In 2007, the team of the Department of Macromolecular Physics under the guidance of prof. Biederman built a new modification of the Haberland gas aggregation cluster source (Figure 5) which benefits from a simple, compact and easily transportable design. In this GAS, a magnetron (or an electrode without the magnetic circuit) can be used for plasma generation when driven by DC or RF excitation. Therefore, a large number of materials are available for processing ranging from gaseous to solid precursors (volatile monomers, metal or polymer targets etc).

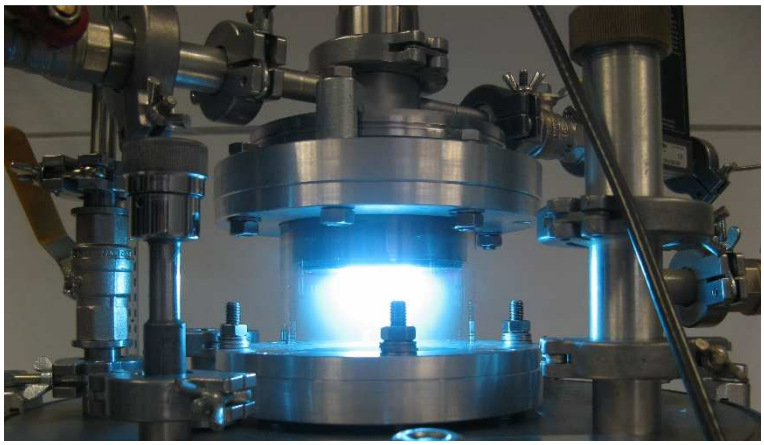

Figure 5. The real photo of the first concept of the gas aggregation source developed at the Department of Macromolecular Physics.

The cluster source is typically mounted onto an additional vacuum chamber in which the deposition of NPs onto substrates can be performed. The GAS does not have an independent pumping system but is evacuated through a small orifice that separates the GAS and the deposition chamber. In contrast to the original Haberland version, there is no NP size separation system which results in typically broader size distribution of the NPs obtained. On the other hand, higher deposition rate is achieved. As can be evidenced in the Figure 5, the first version of the aggregation chamber was made of the tubular glass cylinder. It was established that the deposition rate of NPs produced by that GAS was not stable in time. A possible reason was found in the increase of the temperature of the chamber walls during the long-term operation. Taking that observation into account, the glass reactor was replaced by a stainless steel chamber which was equipped with diagnostic ports and a water cooling system. The continuous flow of tap water carries away the excess heat and keeps the chamber walls at the same temperature which significantly stabilizes the production rate of NPs. The diagnostic ports give the opportunity to control the discharge by monitoring optical emission spectra (OES) or by measuring the electric characteristics with Langmuir probes. The noteworthy feature of the GAS is the ability to govern the morphological and chemical properties of NPs by simple regulation of the main experimental parameters such as magnetron power, working gas mixture, flow and pressure. Moreover, later improvements of the magnetron holder allow also changing the distance between the electrode and the orifice i.e the aggregation length.

In contrast to physical processes of the formation of metallic NPs , the synthesis of polymeric or metal oxide NPs is contributed also by chemical interactions, which influence not only the morphology but also chemistry of NPs [68].

1.2 Composite thin films

The invention of plasma polymers created a new research field in the material engineering. As was discussed in the previous chapters, most of the original studies were focused on the comprehensive investigation of different types of plasma polymers deposited in the form of thin films. They revealed advantageous chemical and physical properties of plasma polymers which have high application potential. The application area of plasma polymers can be extended by using them for the production of composite or structured coatings. Metal/plasma polymer nanocomposites are probably the most well investigated. These coatings are prepared through incorporation of conductive metal NPs into dielectric plasma polymer matrix and reveal distinct electrical and optical properties. The diverse methods of preparation of the nanocomposites have been developed. The first metal/plasma polymer nanocomposite was prepared by Tkachuk et al. in 1973 through plasma polymerization of metalorganic monomer [78]. In the next years, this approach was also tested on the deposition of nanocomposites with Sn [79,80], Fe [81,82], Cu [83] etc. In 1974, N. Boonthanom and M. White presented an alternative method of the deposition of “composite metal polymer film” (cited from the patent [84]) where the polymer (polyethylene) and the metal (copper) were simultaneously evaporated onto the substrate from two independent sources [85]. The coatings were characterized by the homogeneous distribution of NPs throughout the bulk, but the quality of the evaporated polymer film was poor. Just a few years later, Kay et al. [86] came up with an idea to use RF sputtering of metallic target in the atmosphere of an organic gas. This method was successfully applied for the deposition of different gold/fluorocarbon composite coatings [87–90]. In these works, the authors concentrated not only on the deposition procedure but also on the investigation of the functional properties of the final composite. Strong correlation between the metal

volume fraction and the electrical properties was revealed which reflected in a decrease of the resistivity with increasing the amount of metal inclusions in the matrix. Moreover, the coatings were different in color. Due to the particle plasmon resonance, the samples had the characteristic absorption peak in the transmittance optical spectra, the shape and intensity of which depended on the filling factor (Figure 6).

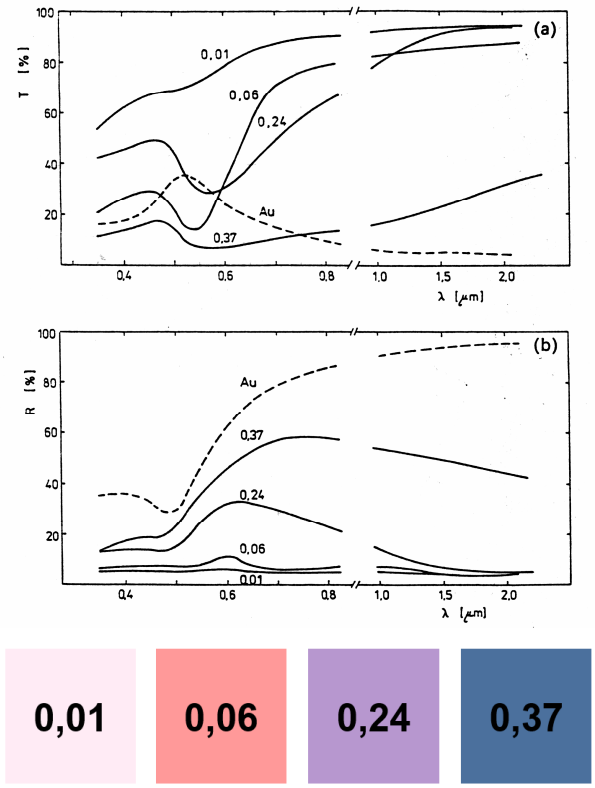

Figure 6. Transmission a) and reflectance b) spectra of gold/fluorocarbon composite coatings with different filling factor (top graphs). Illustration of color of the samples with corresponding filling factor (bottom picture) *(adapted from* [91]*).*

In contrast to the above methods, Biederman and Holland suggested to use magnetron sputtering of composite metal/polymer target or to utilize two independent magnetrons equipped with polymer and metal targets [88]. The sputtering procedure can be performed both in reactive as well as in inert gases [92]. An alternative approach was presented by Lamber in 1995 [93]. There, metallic NPs were independently produced by the Sattler type of the GAS [73] while the organic matrix was deposited by simultaneous plasma polymerization of a liquid monomer. The approach was later used for the deposition of Pd/siloxane [94] and Ag/siloxane

[95] nanocomposites. The construction of a new magnetron-based cluster source had a significant impact on the development of those methods and provided better control over the size and amount of the NPs [96–102].

1.3. Glancing Angle Deposition

The first reports on the utilization of Glancing Angle Deposition (GLAD), i.e. the deposition of nanostructured coatings on substrates inclined at a certain angle toward the source of the depositing material, were presented in the early 20th century [103,104]. The researchers revealed the anisotropy of properties in the films which was not inherent to the same materials prepared at normal deposition. Significant progress of the GLAD technology has been achieved by the end of the last century [105]. The development of the microscopy techniques has allowed to perform the detailed study of the nanostructured films and helped to clarify the important aspects in the mechanism of their formation. The schematic representation of the formation of GLAD films is presented in the Figure 7. The evaporated atoms of a chosen material reach the inclined substrate and depending on its energetic state, they can re-evaporate or adsorb thereon. To initiate the growth of GLAD structures, the adsorbed atoms (or adatoms) have to create stronger bonds between themselves than with the substrate. This type of interaction, known as a Volmer-Weber growth mechanism [106], leads to the formation of small islands which subsequently act as seeds for columnar growth.

If the deposition is performed at glancing angle, some spots on the islands become preferentially exposed to the incoming flux whereas the areas behind them are not reachable for incoming atoms. This mechanism, known as "shadowing effect", is crucial for the GLAD technology [107]. The depositing material is then preferably consumed by the exposed spots resulting in the formation of nanocolumns.

To improve the separation between the nanocolumns, the flux of the depositing material has to be as much as possible collimated. Moreover, GLAD is usually performed at low pressure to minimize the scattering of the incoming atoms from linear trajectory on the atoms/molecules of residual gases. Surface diffusion is

another important aspect that plays an important role in the formation of nanostructured coatings by GLAD. The surface diffusion should be minimized to enhance the shadowing effect and to improve the nanosculpturing. The distinct feature of the GLAD sculptures is the difference between the growth angle β and the angle of the deposition α. In most cases, the columns show smaller inclination with respect to the surface normal as compared to the direction of the incoming material. No general explanation exists which might theoretically describe this phenomenon.

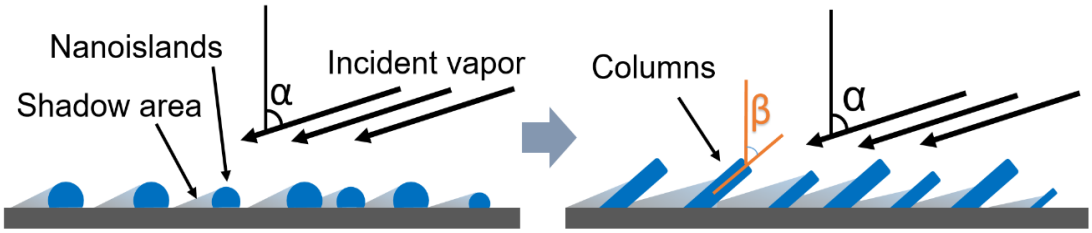

Figure 7. The schematic representation of the formation of GLAD structures (α – deposition angle; β – growth angle).

The number of successfully produced GLAD coatings [108,109] is huge and includes metals, metal oxide or other inorganic compounds. For certain materials that exhibit intensive surface diffusion (polymers or some noble metals) the formation of columnar coatings on the bare substrate can be hindered. Nevertheless, this obstacle can be overcome by using the substrate with preliminary deposited seeds [105]. Nanoparticles produced by GAS are good candidates of choice to play the role of seeds that stimulate the nanostructuring.

Aims of the Doctoral Thesis

The general goal of this thesis was deposition and investigation of various nanostructured and nanocomposite films based on plasma polymers. Different deposition techniques operated both at low and atmospheric pressure were tested. The main experimental approach was based on the utilization of the metal/metal oxide and plasma polymer nanoparticles as building blocks for fabrication of nanostructured coatings. The main objectives of this thesis can be attributed as follows:

1. Application of low pressure and atmospheric pressure plasma techniques for deposition of nanocomposite TiO_x/plasma polymer films and investigation of their properties.
2. The fundamental investigation of the growth mechanism of alumina nanoparticles.
3. Application of plasma polymer nanoparticles for production of biomimetic coatings with multi-scale roughness.
4. Deposition of highly porous plasma polymer nanostructured coatings by means of Glancing Angle Deposition
5. Application of atmospheric plasma jet as an alternative method of deposition nitrogen-rich thin film of plasma polymers.

2. EXPERIMENTAL

2.1. Low pressure plasma deposition techniques

The major part of the deposition techniques used in this work were operated under the low pressure. For this aim, bel-jar type deposition chambers with internal configuration of electrodes were used. The pumping system consisted of consequently connected diffusion and rotary pumps and enabled to obtain the base pressure of 10^{-5} Pa. The transfer of substrates into the deposition chamber was performed through a load-lock system.

2.1.1. Magnetrons

Planar magnetron

A 3-inch planar balanced magnetron, described in Figure 8, was used for sputtering of titanium and aluminum targets for the fabrication of TiO_x and AlO_x NPs. It consists of a water cooled copper head, a magnetic circuit and a grounded stainless steel housing. These are assembled together through a number of insulator gaskets and vacuum sealing o-rings to prevent the electrical contact and possible leakage. Eight neodymium magnets symmetrically fixed on the hexagonal screw-nut are placed into the magnetron head and generate the magnetic field above the top of the target with the intensity of up to 1700 Gauss (G). The power was delivered to the magnetron by a DC generator (Advanced Energy AE MDX 1.5K) working in a constant current mode.

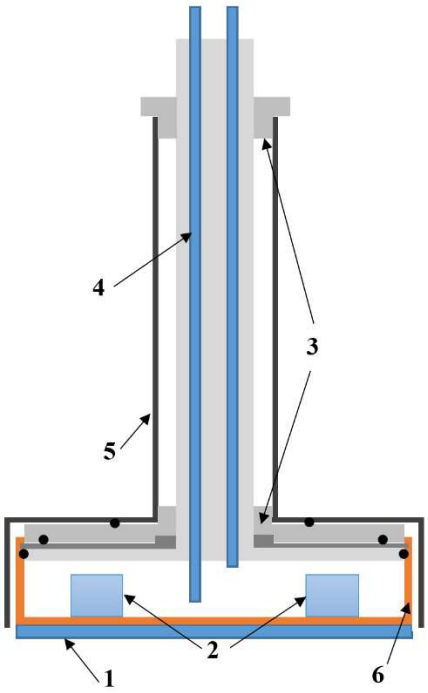

Figure 8. Balanced magnetron used in this work: 1 – target; 2 - neodymium magnets; 3 – vacuum seals; 4 – cooling system; 5 – stainless steel housing; 6 – head of magnetron.

Semi-Cylindrical magnetron

A semi-cylindrical type of the magnetron was exploited for sputtering of a Nylon 6,6 target. The magnetron was built with the aim to increase the amount of sputtered material and thus to promote the formation process of nanoparticles. For this purpose, the cathode was prolonged for 70 mm in the axial direction. A gas inlet was introduced inside the magnetron and entered the plasma zone in the middle of the planar target. The magnetic field was created by the same magnetic circuit as was described above. To ignite the discharge, an RF power generator (Dressler Cesar 600, 13.56 MHz) working in a pulsed regime was used. Sputtering of the polymer target was performed in the atmosphere of Ar.

Magnetron for Glancing Angle Deposition

In the case of Glancing Angle Deposition, the magnetron has to be able to operate at pressures below 1Pa. For low pressure magnetrons, the magnetic field should be enhanced to improve the electron trapping within the magnetic channel

and to intensify the ionization. A special magnetic circuit was designed for GLAD as shown in Figure 9. In this case, six flat magnets (20x10x5 mm) were anchored on the outer part of a steel cylindrical plate, while a cylindrical magnet (15 mm height, 22 mm in diameter) was fixed in the center. To improve the homogeneity of the magnetic field, a 5 mm thick steel ring was placed over the rectangular magnets. Such configuration of magnets allowed to reach the intensity of the magnetic field of 2700 G and to operate the magnetron at pressure of as low as 0.2 Pa.

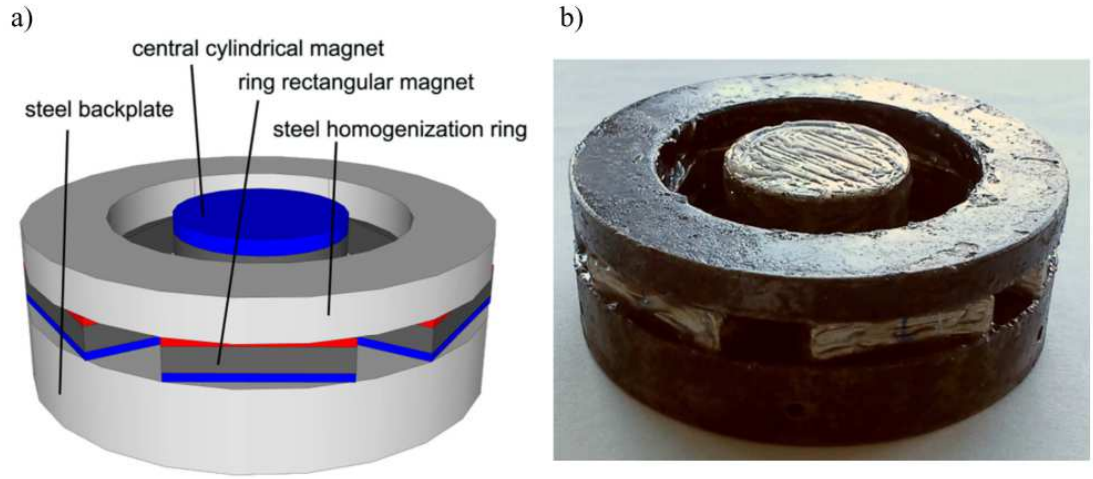

Figure 9. The graphical representation (a) and real image (b) of the magnetic circuit utilized for low pressure deposition of Nylon 6.6 *(adapted from* [110]*).*

Electrode

For plasma polymerization of gaseous precursors, a 3 inch RF water cooled electrode without the magnetic circuit was utilized. To prevent the sputtering of the magnetron head during plasma running, it was equipped with a graphite target with very low sputtering yield.

2.1.2. Gas Aggregation Cluster Sources

Sources based on the planar magnetron/electrode

The Ti/TiO_x nanoparticles were deposited using the Haberland concept gas aggregation cluster source, which was designed and built at our department. It consists of a stainless steel water cooled chamber 110 mm in diameter. A 3-inch

planar magnetron equipped with a 3 mm Ti target was used as a source of material for the formation of NPs. The aggregation chamber is ended by a conically shaped plate with a replaceable orifice (1.5 mm in diameter). The distance between the magnetron and the orifice was constant and equaled to 10 cm. The walls of the cluster source were cooled by water. The GAS was equipped with two diagnostic ports, which were positioned 3 cm from the magnetron plane and used for monitoring of the deposition process by means of optical emission spectroscopy.

The similar source was used for the preparation of plasma polymerized $CHSiO_x$ and SiO_x particles. In this case, an RF electrode was mounted on the aggregation chamber instead of the planar magnetron in such a way that the distance between its top and the orifice could be varied in the range of 4 - 15 cm.

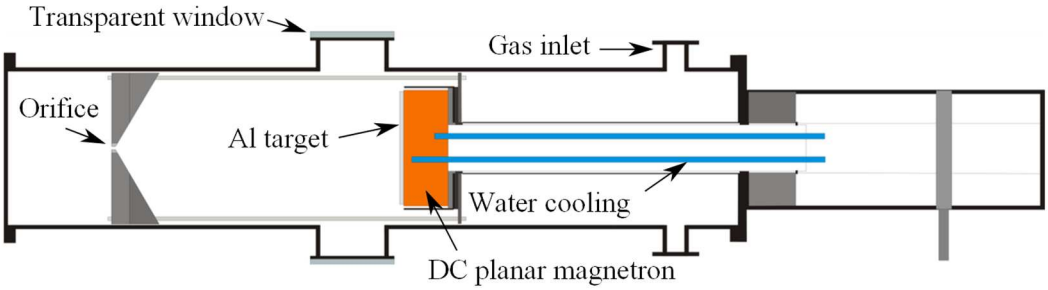

Figure 10. The scheme of the diagnostic type of gas aggregation cluster source.

The formation of AlO_x NPs was studied by a specially designed diagnostic cluster source (Figure 10). In contrast to the previously described model, in this case the magnetron and the orifice holder are interconnected in such a way that the aggregation zone of constant length can independently move with respect to four parallel (40mm) centered diagnostic ports. The diameter of the orifice was 3 mm. DC magnetron sputtering of a 3 mm thick alumina target (purity 99.99%) was used as a source of material. Such configuration enables to study plasma parameters as well as to deposit the nanoparticles at different places inside the aggregation chamber.

Source based on the semi-hollow magnetron

The Nylon-sputtered nanoparticles were deposited by means of the gas aggregation cluster source equipped with the semi-hollow magnetron described above. The detail scheme of this type of GAS is shown in the Figure 11. The semi-hollow magnetron is inserted into the water cooled stainless steel chamber ended by

a lid of conical shape. The orifice diameter was 3 mm. The aggregation chamber is equipped with two ports 40 mm and 16 mm.

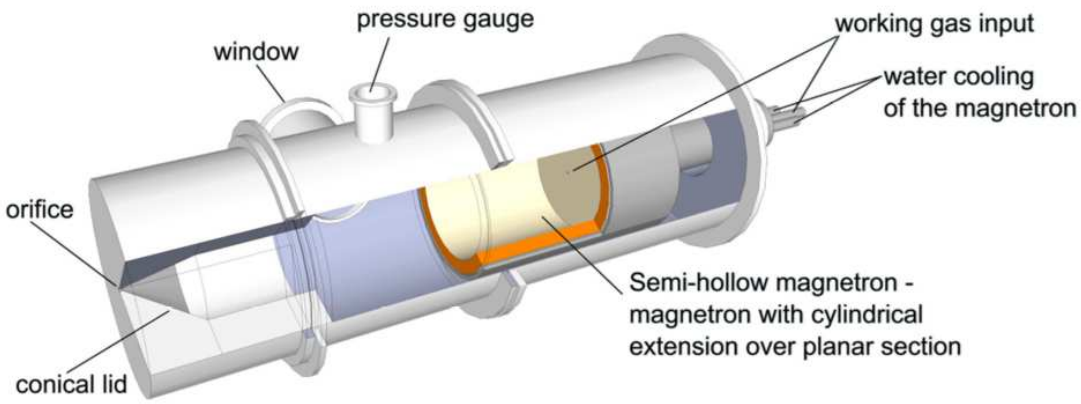

Figure 11. Scheme of the Gas Aggregation Cluster Source equipped with semi-hollow magnetron *(adapted from* [110]*).*

2.2. Atmospheric pressure plasma deposition techniques

2.2.1. Dielectric Barrier Discharge

The overall scheme of the DBD experimental setup used for the deposition of TiO_x nanocomposites is illustrated in the Figure 12. It consists of two stainless steel electrodes separated by an insulator barrier. The upper electrode (20*20*50 mm) is fixed in an electronically controlled holder allowing to move it in the horizontal direction parallel to the counter electrode. The counter electrode, with dimensions of 72x160mm, is grounded. It is covered by the same size 1 mm thick sintered alumina plate. A special mechanism of the holder also enables to change manually the distance between the electrodes in the range between 0 and 10 mm with precision of 0.02 mm. In the given experiment, the electrode gap was fixed at 1.5 mm. The position and velocity of movement of the top electrode are electronically controlled by automatics panel. The electrode configuration enables to dispose four glass substrates (7.5cm*2.5cm) in a row at the 1.5cm distance between each other. Such

experimental approach allowed to prepare several samples in one experimental run without opening the chamber and, as it was found, significantly increased the reproducibility of the obtained results. The whole DBD setup is fixed inside a tightly sealed chamber connected to a membrane pump. All experiments were performed under the constant pressure of 100 kPa. Before each experiment, the whole system was evacuated by the membrane pump. The plasma between the electrodes was generated by a high voltage (peak-to-peak voltage 11kV) low frequency (22 kHz) pulsed power supply. The power delivered to the discharge was measured by a custom-built instrument that enabled monitoring its value in the real time.

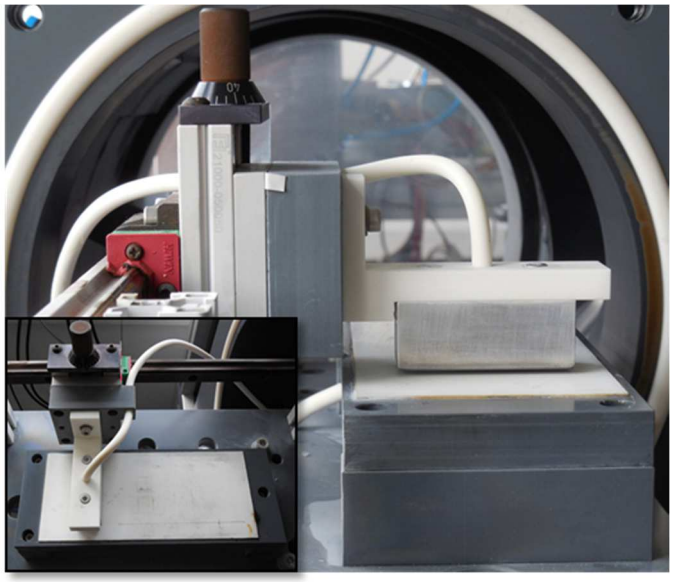

Figure 12. The real photo of DBD electrodes configuration.

The type of the working gas plays a crucial role in the atmospheric pressure DBD deposition. The character of plasma can drastically change in dependence on the gas properties which can influence the properties of the deposited coatings. Therefore, different gases including argon, helium, nitrogen and ambient air were tested. The real photos of the discharge working in the atmosphere of the corresponding gas are shown in Figure 13. Obviously, the best results in terms of homogeneity and stability of plasma were observed in the case of He. The discharge looked very similar to low pressure glow discharge and almost no streamers were observed. However, the discharge in the Ar atmosphere behaved in a different way. In this case, the streamers propagated into all directions and were not homogeneously

distributed on the surface. On the other hand, the character of the discharges working in nitrogen and in ambient air was very similar.

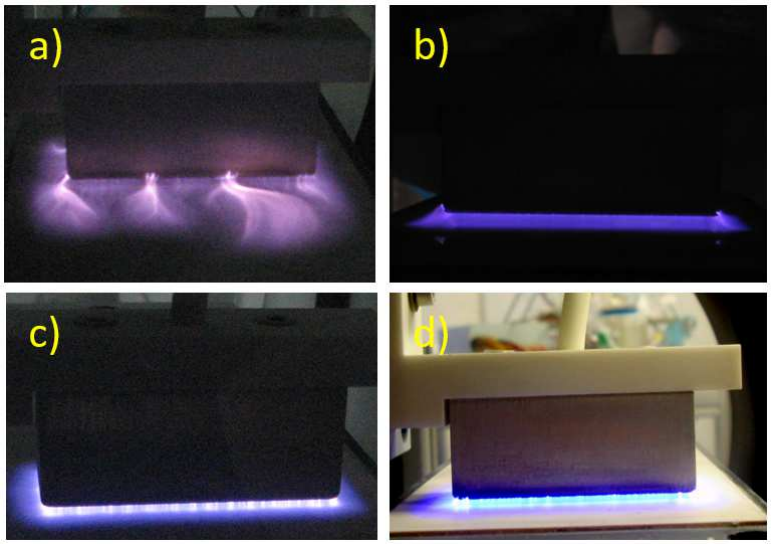

Figure 13. The photos of the dielectric barrier discharge working in the different gases: a)Ar; b)He; c) N_2; d) ambient air.

Taking into account that the atmospheric DBD requires quite large flow of gas (l/min), the use of He was abandoned in this experiment because of its high cost. Nitrogen and ambient air were chosen as carrier gases.

2.2.2. Plasma jet

A specially designed plasma jet manufactured by Dow Corning® under the trade name of SE-2100 Plasma Stream™ was used as the deposition system for nitrogen-rich plasma polymer thin films. A schematic of the plasma jet is shown in Figure 14. In this setup, the precursor is introduced into the discharge by a pneumatic nebulizer in the form of aerosolized droplets. The discharge is sustained by two needle electrodes situated on opposite sides of the entrance path of the nebulizer. Both needle electrodes are on the same potential and powered from a power supply operating at 10–20 kHz and with peak–peak voltage 20–30 kV. The discharge was operated mostly in helium (5slm/min) with the addition of a small amount of nitrogen (70µl/min). Nitrogen was delivered into the plasma in order to stabilize the

discharge and to prevent arcing. The automatically operated holder mechanism allows to perform the depositions both in the static or dynamic regime.

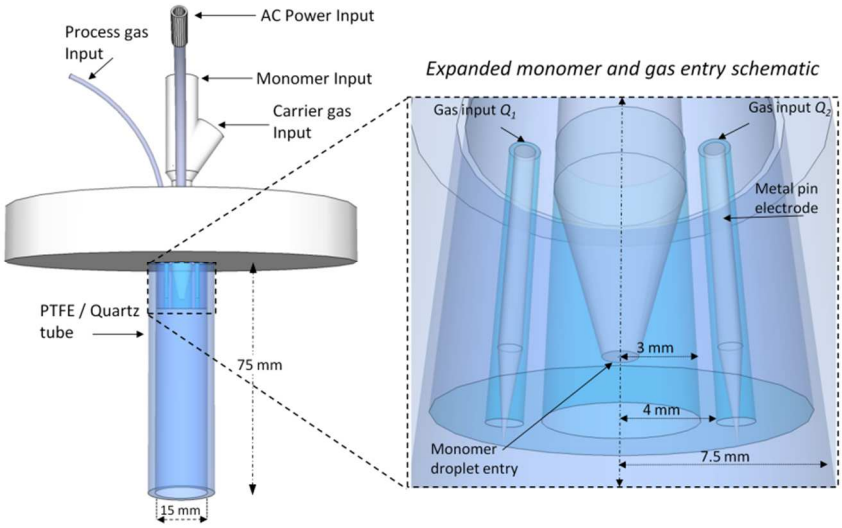

Figure 14. The scheme of the atmospheric pressure plasma jet system *(adapted from* [64]*).*

2.3. Characterization methods

2.3.1. Quartz crystal microbalance

The Quartz Crystal Microbalance (QCM) was used for relative evaluation of the amount of mass deposited on the area unit per time which is expressed in the variation of the resonant frequency of the measuring element – a quartz crystal. A simplified scheme of the QCM setup is described in Figure 15. QCM consists of a specially cut monocrystalline quartz disc (AT or BT cut) with metal (gold or silver) electrodes deposited on its both sides.

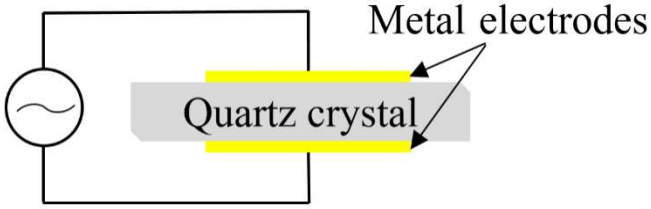

Figure 15. The simplified scheme of the quartz crystal

The application of the alternating electric field across the crystal induces the standing shear wave oscillating at certain frequency. This phenomenon is also known as an inverse piezoelectric effect. The resonance frequency of crystal oscillations is inversely proportional to mass deposited on its surface. The qualitative analysis of that dependence was presented by Günter Sauerbrey in 1959 as follows [111]:

$$\Delta f = -\frac{f_q^2 M_f}{N \rho_q S} \qquad (1)$$

where f_q is fundamental resonant frequency of quartz; M_f is the mass of deposited material; N is frequency constant dependent on the crystal cut (N_{AT} = 1.67*10^5 Hz·cm; N_{BT} = 2.5 * 10^5 Hz·cm); ρ_q is quartz density (2.65 kg/dm^3); S is surface area of the deposited material.

The quartz crystals with fundamental resonant frequency of 5 MHz were used. The QCM was fixed in a special holder and faced the NP beam.

2.3.2. X-ray Photoelectron Spectroscopy

X-ray photoelectron spectroscopy (XPS) is an analytical technique allowing to study both overall elemental chemical composition as well as chemical state of individual elements. Its principle of operation is based on the photoelectric effect. The XPS equipment consists of an X-ray source, a high resolution electron analyzer and a detector mounted on a stainless steel chamber evacuated by oil-free pumps. The XPS measurements are performed under ultra-high vacuum (10^{-7}-10^{-9} torr). That condition allows to minimize the loss of electron energy during their travel to the analyzer and also prevents the oxidation of the X-ray anode surface. The X-ray radiation are produced due to the intensive bombardment of the anode by highly accelerated (10-12 kV) thermoelectric electrons. To prevent the overheating and damage of the anode because of intensive bombardment, it is provided with a water cooling system. In this work, the photons with energy of 1486.6 eV were generated by the Al anode operated at total power of 200W (12kV, 16.8 mA). The irradiation of samples by Al K_α X-Ray beam induces the ejection of electrons from the inner shells of atoms which are then separated by the hemispherical analyzer and finally counted by the detector. The analyzer was operated in the fixed transmission mode. The value of pass energy E_{pass} was established at 40 eV for wide spectra and 10 eV

for high resolution spectra measurements. During the final stage of the XPS procedure, the electrons pass to the detector which amplifies the signal and sends data to PC. Given the energy of incident photon E_{photon} and kinetic energy of electron $E_{kinetic}$, the binding energy $E_{binding}$ can be calculated as:

$$E_{binding} = E_{photon} - E_{kinetic} + Ø \qquad (2)$$

Here, Ø is the spectrometer work function. The data measured by the analyzer and the detector is processed by the special software and presented in a graphical form as amount of electrons vs their binding or kinetic energy. As a result, the characteristic peaks corresponding to the element originated from studied sample are formed. The processing of the measured XPS spectra was performed by commercial software CASA XPS.

2.3.3. Fourier Transform Infrared Spectroscopy

In addition to XPS analysis, the coatings of plasma polymers were also studied by Fourier Transform Infrared Spectroscopy (FTIR). This analytical technique was employed for a qualitative analysis of chemical groups present in the films.

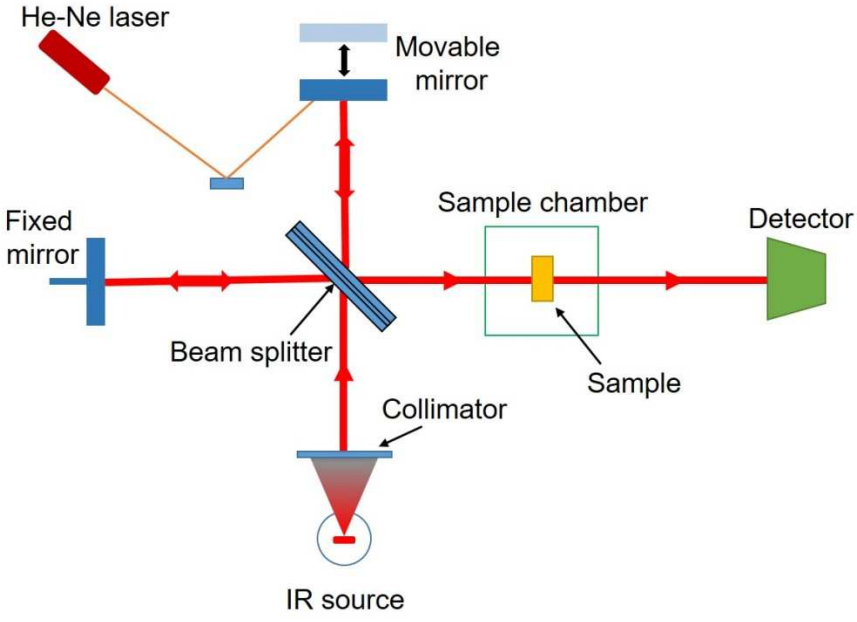

Figure 16. The schematic diagram of FTIR operation.

The operation procedure of the FTIR measurements was as follows (Figure 16). The infrared electromagnetic radiation of a middle region (5000-500 cm^{-1}) was emitted by heated up to 1000℃ silicon carbide rod, passed a collimation system and entered an interferometer. The main elements of the interferometer are a translucent beam splitter and two mirrors. One of the mirrors is fixed, while the other can be moved with high precision. The position of the moveable mirror is monitored with a HeNe laser.

Passing the translucent plate, the focused beam of IR light is splitted into two components. The both rays are reflected off the corresponding mirror and meet each other at the beam splitter, where they merge into one and propagate to the detector. In the given configuration, the sample was positioned between the output of the interferometer and the detector. In dependence on the difference in optical path, which is regulated by the position of the moving mirror, the recombination of the beams results in their constructive or destructive interference. Using the Fourier transformation, the obtained interferogram was processed by software into absorption spectra, where the intensity of the absorbed light is presented as a function of frequency or wavelength. The FTIR measurements are very sensitive to the presence of the residual water vapor. To minimize its amount, the space with sample was blown by dehumidified filtrated air. The samples were measured in the reflected mode. Silicon wafers with evaporated thin film of gold served as substrates. The protocol of the FTIR measurements consisted of 3 scans of reference and subsequent 2 scans of investigated coatings. The obtained spectra were processed by special software SCOPUS.

2.3.4. Ellipsometry

The spectroscopic (192-1690 nm) ellipsometry was used to determine the thickness of deposited coatings. The interaction of polarized electromagnetic wave with specimen results in the changes of its amplitude ψ and phase difference Δ. The corresponding changes of these parameters are closely linked with material properties. Ellipsometry measurements are not influenced by the diffraction limit and allows to work with film thinner than the wavelength of probe source. The

measurements were performed at variable angles from 55° to 75° degree with step of 10°. The analysis of the ellipsometry measurements starts from the creation of a model representing the possible structure of coatings. For this aim, a database containing the large choice of possible materials is available. At the final step, the model is fitted to the experimentally obtained data and thus optical constants and the coating thickness are obtained

2.3.6. Atomic Force Microscopy

Atomic Force Microscopy was used for high resolution analysis of the topography of deposited coatings. Besides the graphical representation of the surface, such statistical parameters as root-mean-square roughness, correlation length, growth and dynamic exponents were also obtained. A cantilever with a very sharp tip at the end plays the role of a probe in AFM measurements. Forces acting between the atoms of the tip and the specimen induce bending of the cantilever. These deflections are monitored by a laser beam reflected from the backside of the cantilever to a segmented photodiode detector. In dependence on the AFM construction, the scanning procedure takes place by XY movement of the cantilever over the sample stage or vice versa. The constant distance between the sample and tip is kept by a feedback system based on a piezoelectric controller. The information from the detector and the feedback system is analyzed by special software and can be represented as an image. In dependence on the nature of forces acting between the tip and the surface, contact, semi-contact or non-contact modes of measurements are distinguished (Figure 17). All the samples in this work were studied by AFM in the semi-contact mode in which the cantilever is oscillated in such a way that it slightly touches the surface in the bottom point of its amplitude. This mode allows obtaining high resolution images of soft and easy-to-damage samples.

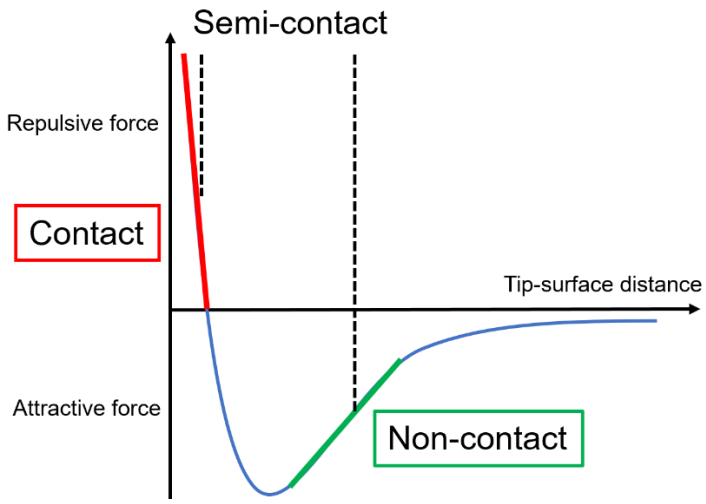

Figure 17. The behavior of interaction force between the samples and tip of cantilever.

2.3.7. Scanning Electron Microscopy

Scanning Electron Microscopy was used to obtain the additional information on the surface structure of deposits. Thermionically generated electrons are focused by a set of condenser lenses and pass through a system of deflection coils which can manipulate with the beam in both axis and thereby perform "scanning". The energy of the electrons can be varied in the range of 0.2 – 40 keV. Depending on the depth of penetration of the incident radiation, the following processes can be induced: secondary electron emission (SE), backscatter electron reflection (BSE) and X-ray emission. Such obtained electrons or photons are then measured by specially equipped detectors positioned close to the sample plane. In contrast to optical microscopy, the higher magnification in SEM is gained by decreasing of the interaction area through better focusing of the beam spot. While the SE and BSE regimes are used to obtain images of the surface, the analysis of the characteristic X-rays emitted from the material gives the additional information about the elemental chemical composition. The SEM measurements are very sensitive to the nature of sample and substrate. In the case of dielectric materials, the intensive electron bombardment of the surface leads to its charging. The emerged electric field impedes the escaping electrons which results in poor quality of the images. If such limitation

occurred, the coatings studied in this work were additionally overcoated by 2 nm film of Pt.

2.3.8. Optical Emission Spectroscopy

Optical emission spectroscopy (OES) was applied for the analysis of plasma during the creation of NPs. Frequent inelastic collisions lead to excitation of atoms/molecules in plasma and to their subsequent relaxation back to the ground state which can be accompanied by emission of photons Analysis of the spectral lines allows to estimate the relative quantity of emissive species in the gas phase. Emission from plasma was collected via an optical fiber and analyzed by an Avantes spectrometer in a wavelength range 240-410 and 650-850 nm with resolution of 0.5 nm.

3. RESULTS AND DISCUSSION

3.1. Ti/TiO_x/plasma polymer nanocomposite coatings

3.1.1. Ti/TiO_x nanoparticles prepared by gas aggregation cluster source

The Ti/TiO_x NPs were deposited by the type of the gas aggregation cluster source, which was described in detail in the experimental part 2.1.2. The deposition rate of NPs was monitored using quartz crystal microbalance positioned at 25 cm from the orifice. The investigation of the influence of the magnetron current and pressure in the aggregation chamber on the deposition process showed the opposite trends. The summarized results of the measurements are described in Figure 18.

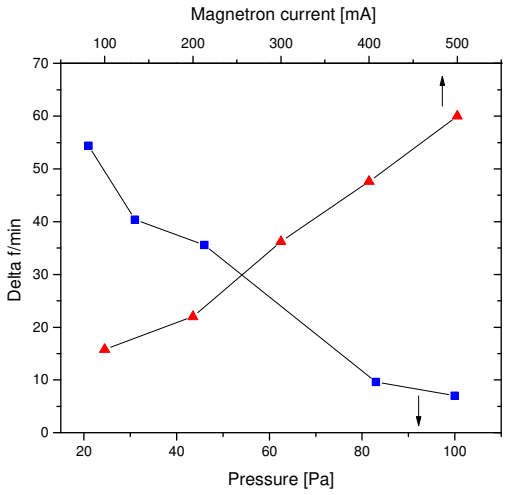

Figure 18. Deposition rate of Ti NPs in dependence on pressure and magnetron current inside the cluster source.

The pressure in the cluster source was adjusted by changing the flow rate of Ar under the constant 1.5 mm diameter of the orifice. It can be seen that the increase of pressure from 17 Pa to 97 Pa led to the significant reduction of the deposition rate. The elevation of the magnetron current had an opposite effect on the deposition rate. Its linear increase was observed with the current increasing from 100 to 500 mA.

The possibility to prepare oxidized titanium (TiO_x) NPs was also investigated. The experimental approach was based on the addition of a precise amount of oxygen

into the aggregation chamber during sputtering of the Ti target. The experimental parameters (pressure – 27 Pa, flow – 1.5 sccm, current – 300 mA) were chosen to provide the relatively high flux of titanium NPs. The amount of added O_2 was adjusted by a preliminary calibrated needle valve. After a certain flow rate of oxygen was set, the deposition rate (QCM) and the magnetron voltage were monitored to establish the moment when both were stabilized. The results are presented in Figure 19.

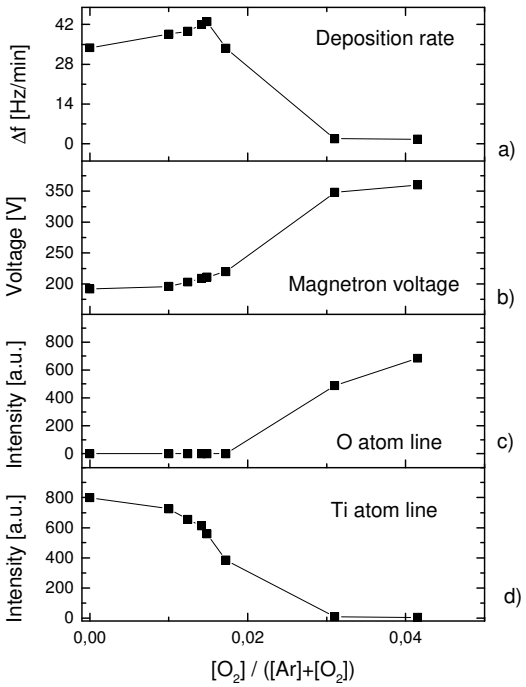

Figure 19. The dependence of a) deposition rate, b) magnetron voltage, c) intensity of Ti I (521 nm) and d) O I spectral line (777nm) in dependence on the oxygen amount in the working mixture.

Introduction of a very small O_2 concentration to the plasma induces a slight increase of the deposition rate up to the maximum value corresponding to 1.5% of oxygen in the mixture. The further increase of O_2 leads to the abrupt decrease of the production rate. At the same time, the magnetron voltage gradually increases with the oxygen percentage. The possible explanation of the observed results can be found in detail analysis of the OES measurements. All optical spectra were taken at the constant 4 cm distance from the magnetron. The most intensive spectral line is detected for Ti I (521nm) and at higher O_2 concentration for oxygen O I (777nm).

The analysis of the OES spectra shows that the increase of the oxygen concentration leads to the decrease of the intensity of Ti and Ar spectral lines. No signal from O I is observed in case of smaller concentration of O_2. At the moment when oxygen becomes detectable by OES, the abrupt elevation of the voltage and the subsequent decline of the deposition rate is observed.

To evaluate the effect of added oxygen on the chemical composition of prepared NPs the X-ray Photoelectron Spectroscopy was used. The XPS analysis was performed for NPs prepared without oxygen and with 1.4 % of oxygen in the mixture. In order to prevent the possible oxidation and contamination of the coatings, both samples were transferred to the XPS chamber without breaking vacuum.

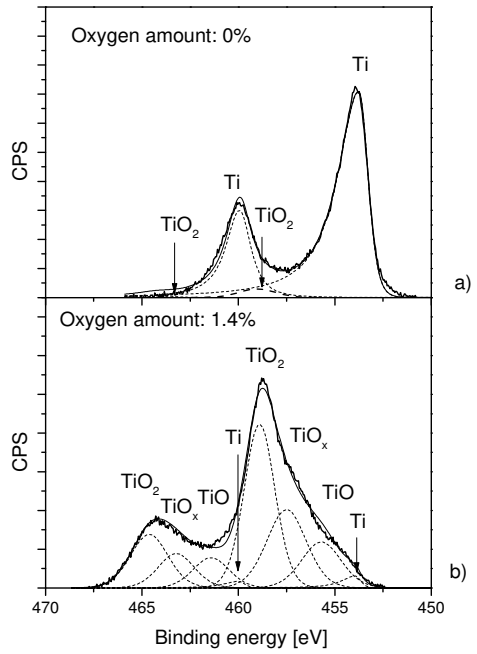

Figure 20. Comparison of the Ti 2p high resolution XPS spectra of coatings deposited in a) pure Ar or b) with 1.4% of O_2 in Ar/O_2 mixture.

The significant difference of the chemical composition of the samples can be estimated by comparing the high resolution Ti 2p spectra, which are presented in Figure 20. In the case of sputtering in Ar, well separated signals from metallic $Ti_{1/2}$ and $Ti_{3/2}$ were detected. The addition of oxygen resulted in the shift of the Ti 2p peaks to higher binding energy. The high resolution analysis revealed that the metallic Ti bonds were predominantly replaced by oxidized Ti. The slight changes were also observed in the morphology of the deposited coatings. The SEM images

and the size distribution histograms of NPs prepared with and without O_2 are shown in Figure 21. The coatings prepared in the oxygen-free mixture consisted of the rectangularly-shaped NPs with the mean size of 35 nm. The mean size of the NPs deposited at 1.4 % of O_2 was smaller, around 27nm, but the total size distribution was broadened.

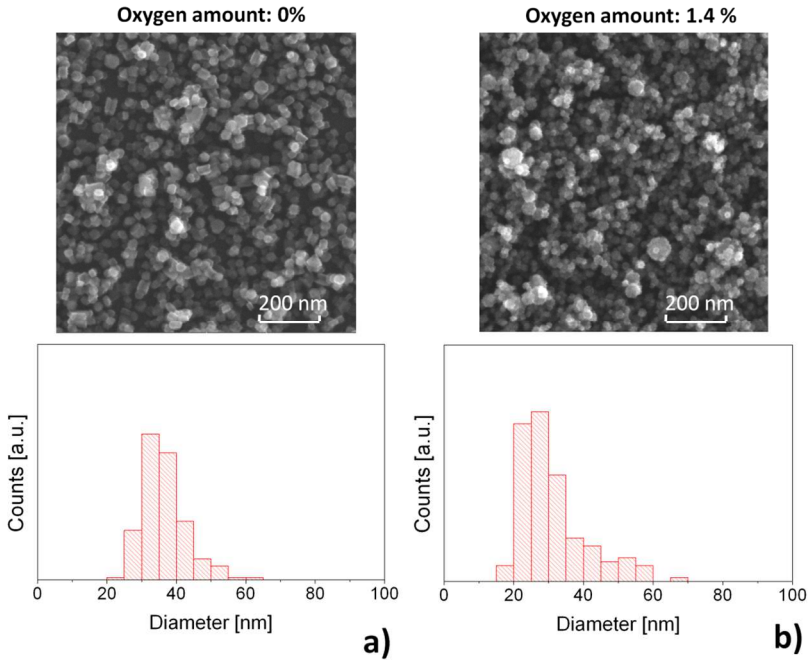

Figure 21. Top view SEM images and corresponding size histograms of NPs fabricated in a) pure Ar or b) Ar/O_2 mixture with 1.4% of O_2.

3.1.2 Ti nanoparticles overcoated by C:H plasma polymer for fabrication of mesoporous coatings

Nanocomposite *n*-hexane/Ti NPs coatings were prepared in two steps. First, Ti NPs were deposited by the GAS described in the experimental section 2.1.2. DC magnetron sputtering of titanium in Ar at pressure of 28Pa and with the magnetron current of 300 mA was used. As a result, the 2.4 $\mu m^{-2}\ s^{-1}$ flux of Ti NPs with the average size of 50 ±7 nm was obtained. The set of the same NP coatings were deposited on polished silicon wafers. In the next step, all the samples were covered by hydrocarbon plasma polymer thin films of different thickness. The 3 inch RF planar electrode equipped with the graphite target was run at the power of 100W for

plasma operation. The deposition of plasma polymer thin films was performed in the *n*-hexane/Ar (1:1) working gas mixture at the total pressure of 3 Pa. The samples with the Ti NPs together with the reference Si wafers were exposed to the plasma deposition for different time.

The investigations of the mechanical properties of the plasma polymer thin films using nanoindentation revealed that the complex modulus of hydrocarbon films was 5-7 GPa and corresponded to soft hydrocarbon (CH_x) plasma polymers.

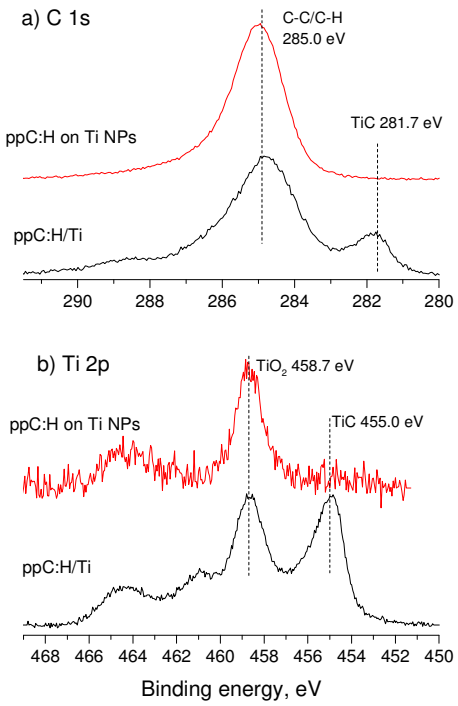

Figure 22. a) C1s and b) Ti2p XPS spectra of the coatings prepared by overcoating of Ti NPs by plasma polymer films (top graph) or simultaneous sputtering of titanium in the *n*-hexane/Ar mixture (bottom graph).

To investigate the chemical interaction between the particles and the plasma polymer matrix, the X-ray photoelectron spectroscopy was applied. Since the XPS technique can be used for analysis only of the top 10 nm of material, only thin layers (9 nm) of plasma polymer were investigated. It can be seen in Figure 22 b) that the position of the Ti $2p_{3/2}$ peak at 458.7 eV is characteristic to the TiO_x compounds and no other chemical bonds with titanium are present. No significant changes are also observed in the C1s spectrum, which is dominated by the C-C, C-H bonds with the

small contribution from slightly oxidized species. Based on the analysis of the high resolution spectra, one can conclude that there are no chemical bonds between the metallic particles and the plasma polymer film. Interestingly, different interaction mechanism was observed in the earlier work on DC magnetron sputtering of Ti in *n*-hexane/Ar mixtures[112]. The XPS analysis of that composite showed the presence of titanium carbide bonds both in Ti 2p and C 1s spectra (bottom curves in Figure 22 a), b)).

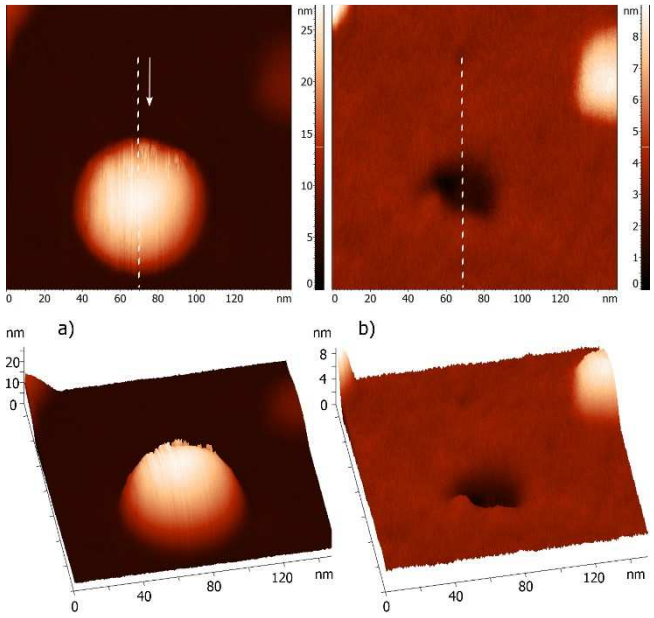

Figure 23. The AFM images of titanium nanoparticle a) before and b) after performance of ploughing procedure.

In order to analyze the conformality of plasma polymer deposition, AFM ploughing was applied. For this aim, a separate Ti NP overcoated by 9 nm of plasma polymer was chosen. Figure 23 shows the top and the 3D AFM images of the NP before and after it has been ploughed by the AFM DLC (diamond like carbon) tip. It can be seen that according to the height scale of the AFM scan, the size of the buried particle is approximately 22 nm. The direction and trajectory of the AFM ploughing are marked by an arrow and a dotted line in Figure 23. The application of the normal force to the surface leads to the displacement of the NP and results in the formation of a circularly-shaped crater. It was detected that it has the hemispherical shape with small irregularities caused by the ploughing procedure.

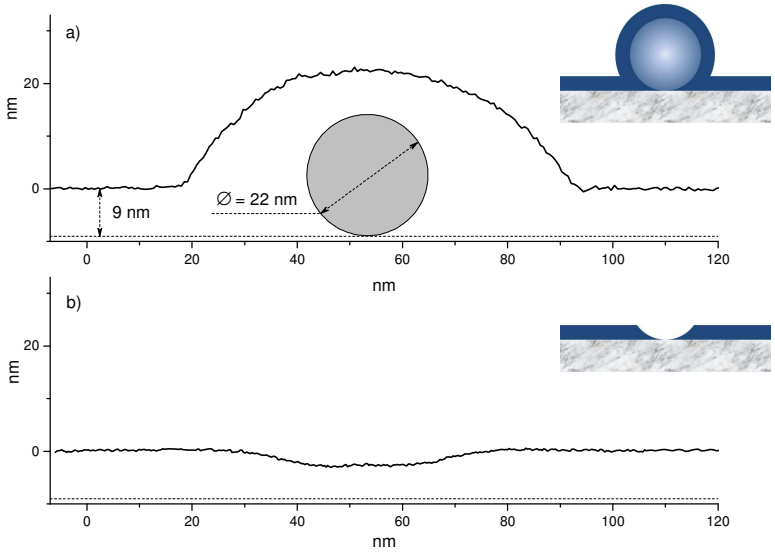

Figure 24. The height profiles taken across the single Ti NP covered by 9 nm of hydrocarbon thin film: a) before and b) after performance the AFM ploughing. The circle under the profile is schematic description of the position of Ti particle.

The shape of the single Ti particle before and after the removing procedure can be also seen in Figure 24, where the schematic pictures along with measured height profiles are described. The results indicate that the plasma polymer-forming species penetrate into the void between the NPs and fill the pores beneath them.

The series of Ti NP coatings (prepared with the same deposition time of 12 min) was coated by plasma polymer thin films for different time from 27 s up to 1080 s. Each of these samples was then subjected to SEM top and cross-section analysis. It can be seen in Figure 25 that the deposition changed the surface morphology. Moreover, the nonlinear behavior of such alterations was observed. In contrast to the 27 and 54 s exposure periods, where almost no structural difference was observed, the fast increase of the thickness of plasma polymer film was detected for all the following samples. This observation supports the previous results and indicates that during the first phase of the deposition of the plasma polymer film, hydrocarbon radicals penetrate into the pores between the NPs filling them with the plasma polymer. After the pore filling is complete, further deposition induces the increase of the effective thickness of coatings.

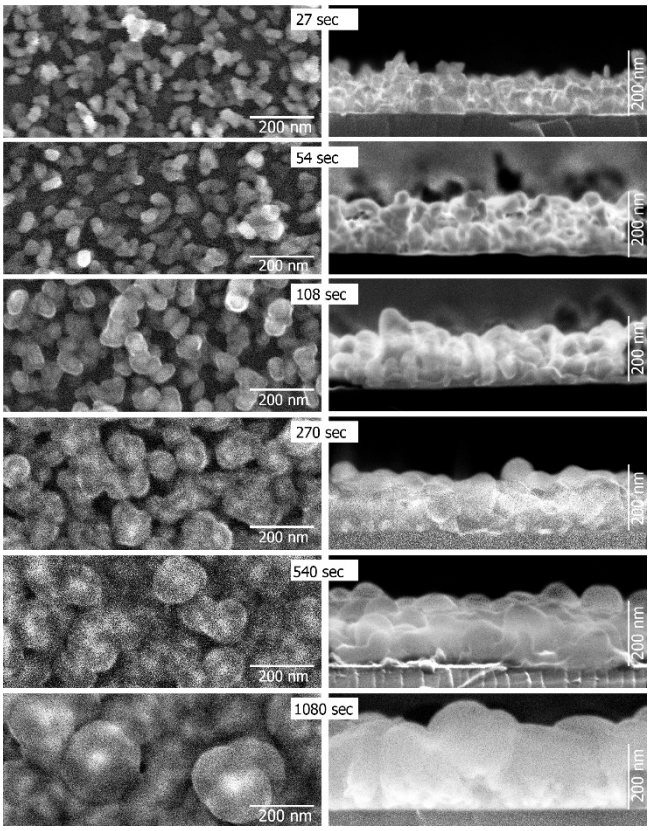

Figure 25. The top and cross-section SEM images of the Ti NPs exposed to the deposition of the hydrocarbon plasma polymer for different time.

To perform the quantitative analysis of the structural changes, the AFM analysis was performed. For comparison, plasma polymer films deposited onto blank Si wafers were also measured. All these films were very smooth and RMS roughness of the thickest film did not exceeded 0.5 nm (at 1 μm scan size). The AFM scans of Ti NPs/*n*-hexane nanostructures are shown in Figure 26. These results correlate well with the morphological changes observed previously by SEM. At first sight, the size of the surface features monotonically increases with the exposure time. However, the detailed statistical analysis of the AFM data shows the nonlinear behavior of the main surface parameters.

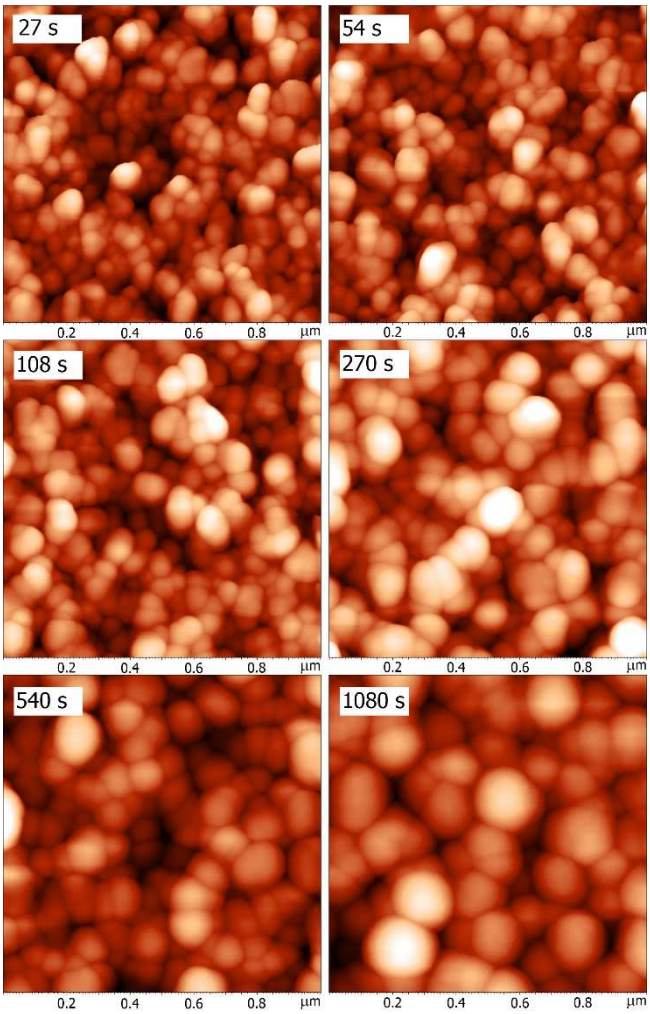

Figure 26. AFM scans of the Ti/n-hexane nanostructured coatings.

As evidenced in Figure 27, the RMS roughness *w* of the coatings exposed to the deposition for 28 and 54 s almost did not change and its value was similar to the uncovered NPs. Further increase of the treatment time led to the overall smoothening of the surface and to the linear decrease of the RMS roughness. This is also confirmed by the negative value of the growth exponent β = -0.16. For comparison, thin films of *n*-hexane plasma polymer deposited on Si wafers were also measured by AFM. In this case, the increase of the deposition time led to a slight increase of *w* from 0.28 to 0.47 nm. The analysis of the growth exponents revealed a difference in the growth mechanism. The correlation length ξ is another important component which can bring the additional information about the topographical changes in the lateral direction. Figure 27 b summarizes all the data of ξ for both nanocomposites and thin films on Si. In addition, the dynamic exponent z, which describes the temporal evolution of the correlation length, is also given.

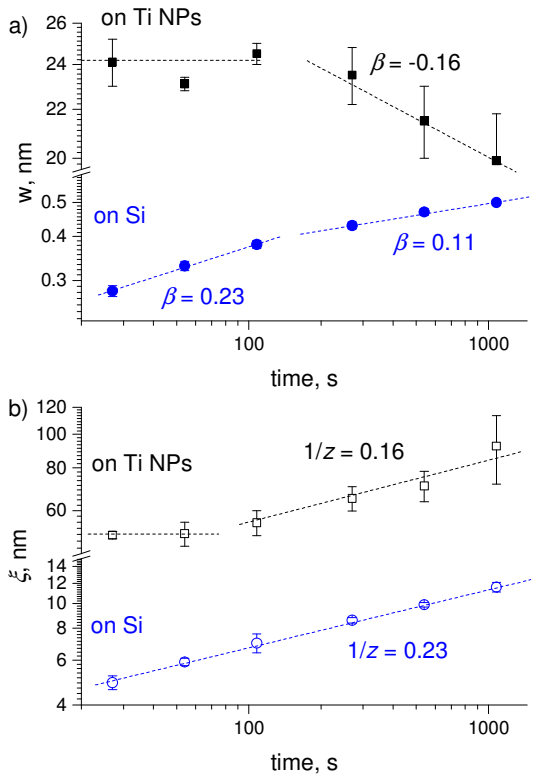

Figure 27. a) The RMS roughness *w* and b) correlation length ξ of Ti NPs/*n*-hexane plasma polymer composite (squares) and thin plasma polymer film on Si wafer (blue circle).

It can be seen that the correlation length of the plasma polymers deposited on Si wafers linearly increases from 4 to 10 nm. The corresponding dynamic exponent is equal to 1/z=0.23±0.02. In the case of Ti NPs coatings, the correlation length does not change in the beginning and then it starts to increase. The increase of the correlation length during the later stage of the deposition indicates that the structures on the surface become wider. These results confirm the previous assumption that two stages of the deposition can be distinguished. In the early stage, the plasma polymer fills the pores between the NPs. In the later stage, free space becomes completely filled and the film starts to grow on top of the surface in the normal direction to the substrate plane.

3.1.3 Atmospheric pressure dielectric barrier discharge for production of TiO_x nanoparticles and their composites

In this part of the thesis, the application of the atmospheric pressure dielectric barrier discharge (DBD) for deposition of TiO_x NP coatings will be described in detail [113]. The scheme of the experimental setup can be seen in Figure 28.

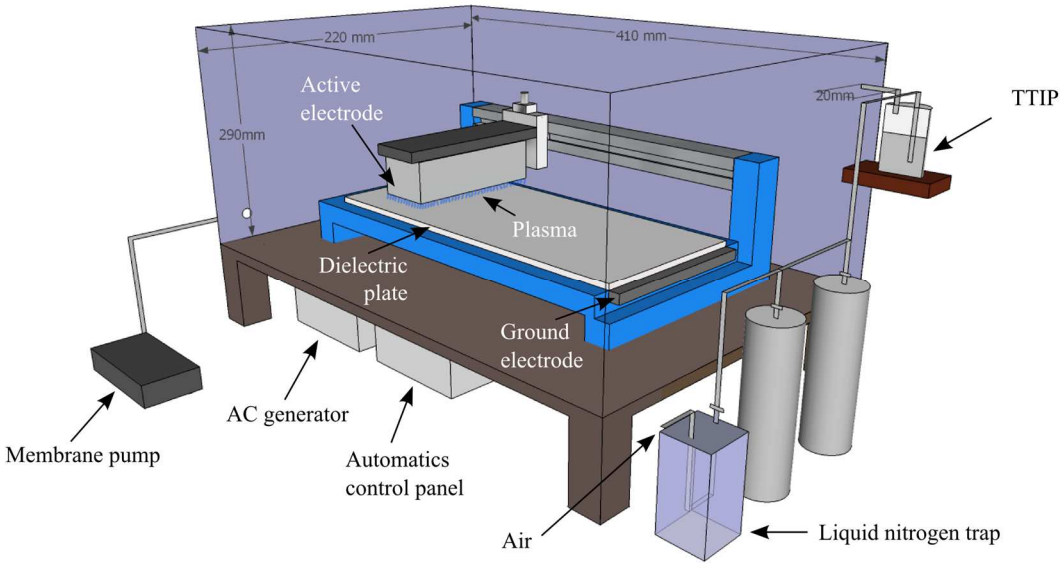

Figure 28. The scheme of the experimental setup.

Among the two commercially available liquid precursors, titanium chloride ($TiCl_4$) and titanium tetraisopropoxide (TTIP, $Ti[OCH(CH_3)_2]_4$), the second one was chosen. The monomer was placed into a bubbler flask. The flow of the carrier gas transferred the saturated vapor of the TTIP to the deposition chamber. To keep the stable partial pressure of the precursor, the bubbler flask was maintained in a water bath under the constant temperature of 25 °C. To prevent the condensation of the monomer during the transportation, the manifold between the flask and the deposition chamber was made as short as possible (2cm). The first experiments revealed that the monomer is highly reactive with residual water vapor, which was the main problem in case of using ambient air as a carrier gas. In order to prevent undesirable chemical interaction, the ambient air was dried by passing through the liquid nitrogen trap before entering the flask with the monomer. Due to the complexity of the experiment, it was decided to replace the ambient air by N_2 (80%)

and O_2 (20%) mixture i.e. with so-called synthetic air. To insure that the influence of synthetic air on the fabricated coatings is comparable to the ambient air effect, a number of samples was deposited in the corresponding gas mixtures, while the other experimental parameters were kept constant (power – 20W, gas flow – 2 slm (standard liter per minute), deposition time – 20 min). As can be seen in Table 1 and in Figure 29, the XPS composition of both coatings is almost identical.

Working gas	Ti, at. %	C, at. %	O, at. %	Si, at. %
air	16	25	57	2
N_2+O_2	14	25	59	2

Table 1: XPS elemental composition of the films deposited by DBD in dry air and in the synthetic air. Power 20 W, gas flow 2.0 slm.

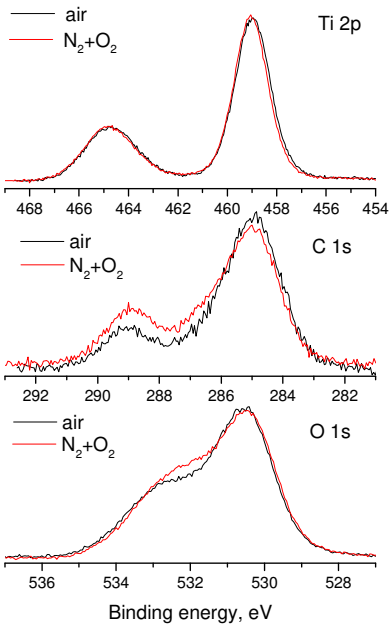

Figure 29. XPS spectra of the films deposited by DBD in dry air and in the mixture of 80% N_2+20% O_2.

In the next experiments, the coatings prepared in the synthetic air were compared to the samples produced in pure nitrogen. A series of the samples was fabricated in the N_2 atmosphere under the constant flow rate of 2slm, the power of

20W and with different deposition time. By weighing the samples before and after the deposition, the linear dependence of the growth rate on time was established (Figure 30). From these results, the constant deposition rate was calculated to be 3.1 $\mu g/cm^{-2}min^{-1}$.

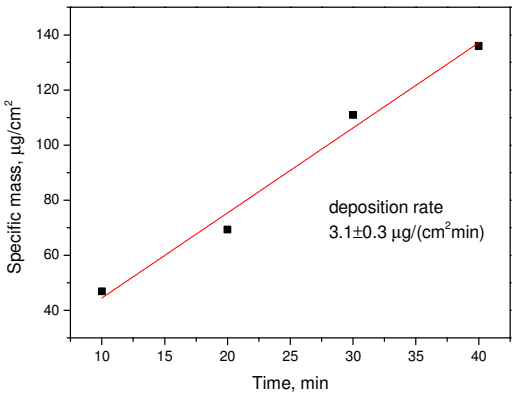

Figure 30. The mass of the deposits in dependence on the deposition time. (N_2, 20 W, 2.0 slm).

The SEM analysis of the coatings produced in N_2 revealed their very porous structure (Figure 31 a, b). The coatings consisted of spherical particles with the mean size of 40nm embedded into the irregularly shaped compact substance, which can be assigned to the plasma polymer phase. For comparison, the SEM images of the coatings deposited in dry synthetic air are presented in Figure 31 c, d. These coatings also consist of particles, but their mean size is slightly smaller (30nm). In this case, the individual particles are well detectable and almost no polymeric phase is observed. Obviously, oxygen added to the working gas serves as a reactant that etches hydrocarbon compounds and transforms them to volatile species.

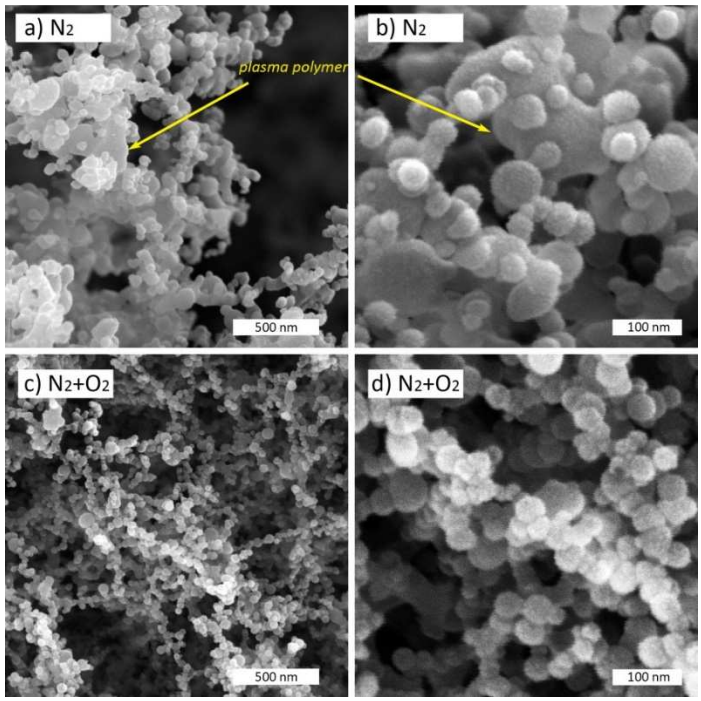

Figure 31. The SEM images of the coatings prepared by atmospheric pressure DBD with a) b) N_2 and c) d) synthetic air. Discharge power 20 W, flow rate 2.0 slm, the deposition time 20 min.

The coatings similar to the ones shown in Figure 31 were studied by XPS. The analysis of the films deposited in the synthetic air revealed that they do not contain any nitrogen and consist of titanium (14%), oxygen (59%) and carbon (23%). In addition, a slight signal from Si 2p from the substrate was observed. The deconvoluted high resolution C1s and O1s spectra are presented in Figure 32 a, b. It can be seen that the carbon peak is dominated by the C-C/C-H groups at binding energy of 285.0 eV. Oxidation of carbon during the deposition resulted in the detection of C-O, C=O and O-C=O functionalities at 286.5 eV, 288.0 eV and 289.0 eV, correspondingly. The deconvolution of the O1s spectrum was performed taking into account that oxygen in the coatings may originate from different sources including TiO_x, oxidized carbon or glass substrate. The most abundant component at 530.0 eV corresponds to the oxygen bonds in TiO_2 whereas the peak at 531.7 eV is assigned to the C-O groups. To account for the oxygen contribution from the substrate, the third SiO_2 component was added at 533.2 eV.

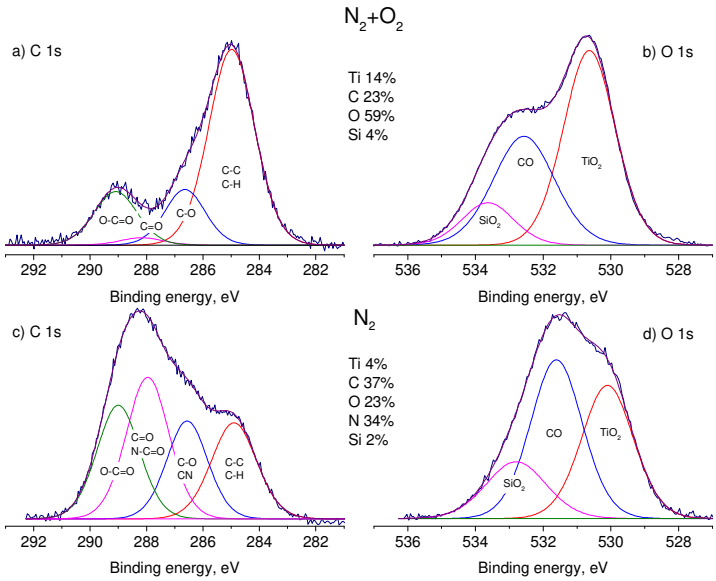

Figure 32. XPS of the coatings deposited by DBD a) b) in synthetic air; c) d) in nitrogen. Power 20 W, gas flow 2.5 slm.

The chemical composition of the coatings prepared in nitrogen is completely different. The deposits are poor in titanium (4%) and oxygen (23%). In comparison with the coatings prepared in synthetic air, there is a large increase in nitrogen and carbon content up to 34% and 37%, correspondingly. Carbon-to-nitrogen bonding environment dominates the C1s peak; thus, the major portion of nitrogen is bound to carbon in the plasma polymer phase. It has to be noted that the high-resolution XPS analysis of the plasma polymer is complicated because of the presence of many different chemical species which have similar binding energy. For example, the peak at 286.5 eV is assigned to the C-O bond but it can also bear the contribution from various carbon-to-nitrogen species such as C-N, C=N or C≡N. For simplicity, this peak was designated as CN/C-O in Figure 32. The peak at 288.0 eV is attributed to the carbonyls but it can be also overlapped with the signal from the N-C=O groups. The O 1s spectrum shows that most of oxygen is bound to carbon in the plasma polymer. These results confirm that the embedding matrix, which was observed on the SEM images, is certainly plasma polymer.

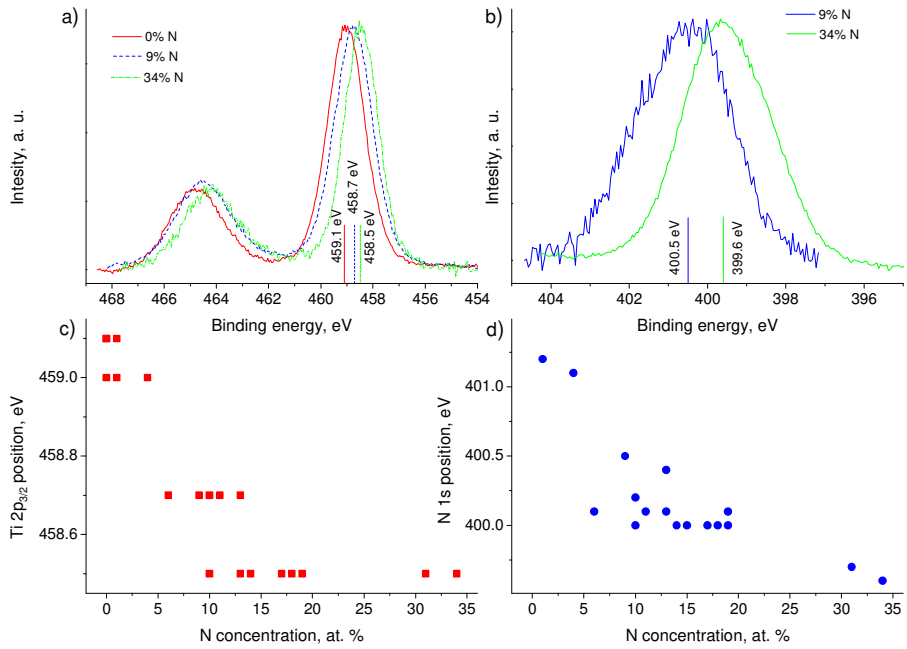

Figure 33. The Ti 2p (a, c) and N 1s (b, d) peak position in dependence on the atomic concentration of nitrogen in the deposited films

The Ti 2p and N 1s XPS spectra of all the samples were similar in shape and the only difference was found in their position, which depended on the nitrogen content in the coatings (Figure 33). It has to be noted that no shift of the O 1s or C 1s peak position was observed. The Ti 2p spectra of the coatings with different amount of nitrogen are shown in Figure 33. No signal from metallic titanium (453.7 eV) or titanium carbide (455.0 eV) was detected. No carbide peak (281.6 eV) was also observed in the C1s spectrum. This result is in a good agreement with the SIMS study provided by Maurau et al. [114] who showed that TiO_x coatings deposited by blown arc also did not contain any carbides.

The Ti 2p peak of the coatings without nitrogen is positioned at 459.1 eV (Ti 2p3/2). This binding energy corresponds to titanium bound in TiO_2. The increase of the nitrogen concentration results in the shift of the titanium peak to the lower binding energies. The minimum binding energy of 458.5 eV was observed in the coating with the highest 34% percentage of nitrogen. The overall shift of the titanium peak can be seen in Figure 33 c, where all the results are summarized. The shift of the peak position points at the change in the chemical environment of the studied element. One can suggest that the above changes are induced by the formation of the TiN bonds, the binding energy of which is usually lower as compared to titanium

oxides. However, the formation of pure titanium-nitride seems to be hardly possible taking into account the high concentration of oxygen in the coatings. To find the reason for the observed changes in the titanium spectrum, the analysis of the N 1s peak was performed. Clear dependence of the N 1s peak position on the nitrogen content can be seen in Figure 33 b, d. It is interesting that no bonds of nitrogen with titanium were detected. The binding energy of nitrogen bound in TiN is typically in the range of 395.8–397.8eV. The lowest value observed in the samples was 399.6 eV and it was assigned to nitrogen bound to carbon. The decrease of the nitrogen content is obviously accompanied by the reduction of the plasma polymer phase in the coatings. At minimum concentration of nitrogen, the N 1s peak is located at 401.0 eV that is related to oxynitride doping of TiO_2. At the same time, no presence of the NO_2 bonds observed by Gordeev et al. [115] at 404.6 eV was detected. From all aforesaid, it can be concluded that TiO_2 nanoparticles deposited by atmospheric pressure DBD in N_2 are nitrogen-doped and their chemical formula can be represented as $TiO_{2-x}N_x$.

In the next experiments, the influence of the flow rate and discharge power on the properties of the deposited coatings was investigated. The series of the samples were prepared in the mixture of N_2+O_2 at different flows under the constant power and vice versa. Three different values of the flow (0.4, 1.0, 1.8 slm) and the power (10, 20, 30 W) were tested. Unexpectedly, all the coatings have the same chemistry independently on the experimental conditions. Probably, the range of the parameters used was not sufficient to affect the plasma chemistry.

Different results were obtained when only N_2 was used as a carrier gas. As can be seen in Table 2, the increase of the discharge power induces the decrease of the carbon and nitrogen concentration. At the same time, the titanium and oxygen content increases. The small signal from Si was observed in all the samples regardless the deposition parameters and it can be explained by highly porous structure of the coatings.

Power, W	**Ti, at.%**	**C, at.%**	**O, at.%**	**N, at.%**	**Si, at.%**
8	5±1	39±3	35±3	19±2	2±2
10	4	29	40	19	8
20	11	25	50	10	4
30	13	19	55	6	7
Flow rate, slm					
0.4	13	15	59	9	4
1.0	11	28	46	11	4
1.4	9±2	32±3	42±4	13±3	3±1
1.8	4	36	25	31	4
2.5	4	37	23	34	2

Table 2: XPS elemental composition of the films deposited by DBD in N_2. Experiments with varying discharge power (N_2 0.7 slm, 20 min) and flow rate (20 W, 20 min).

The changes in the elemental composition are consistent with the changes in the high resolution C1s and O1s spectra depicted in Figure 34. The clear transformation of the chemical environment can be seen in the C 1s spectrum. The C-O, C-N and N-C=O components dominate the spectrum of the coatings prepared at 8 W while their concentration decreases with the increase of power. The analysis of the XPS high-resolution O 1s spectrum shows that most of oxygen atoms is bound with carbon in these coatings which are rich with the plasma polymer. The elevation of power leads to the significant reduction of the oxidized carbon bonds and to the simultaneous increase of the signal from TiO_2.

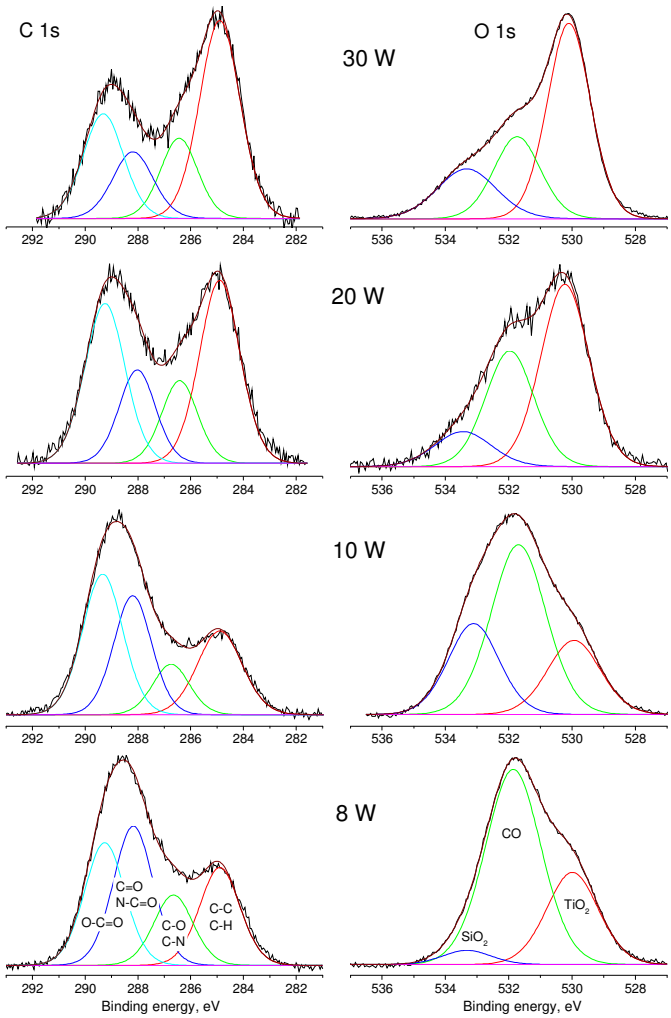

Figure 34. The C 1s (left column) and the O 1s (right column) XPS of the coatings deposited by DBD under different discharge power (N_2 0.7 slm, 20 min).

Similar results were observed in the XPS of the samples deposited with different flow rate of nitrogen. The coatings prepared at low flow rate contain the higher portion of Ti and the smaller concentration of N. The increase of the flow rate has an opposite effect and leads to the decrease of the titanium percentage from 13% to 4%, which is accompanied by the increase of nitrogen and carbon content. The changes in the elemental composition are also confirmed by the high-resolution C 1s spectra that are shown in Figure 35. It can be noted that the elevation of the nitrogen flow rate causes the decrease of the hydrocarbon components and the increase of the amount of the nitrogen-containing groups. These results are in good agreement with the changes observed in the O1s spectrum, for which the concentration of TiO_2 decreases with the higher flow of N_2.

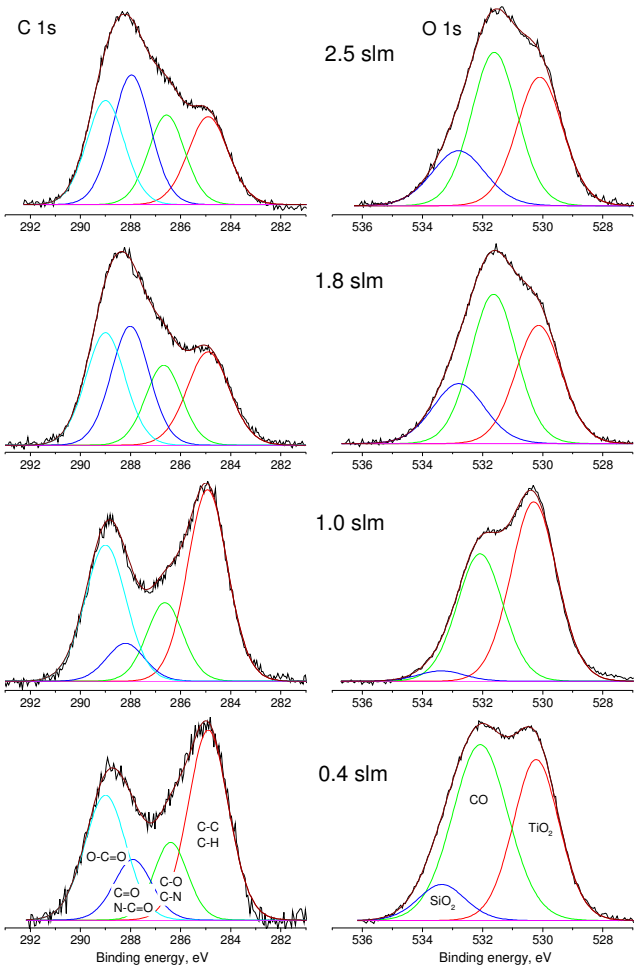

Figure 35. The C 1s (left column) and the O 1s (right column) XPS of the coatings deposited by DBD under different flows of N_2 (power 20 W, 20 min).

The observed dependences of the chemical composition of the coatings on the discharge power and the nitrogen flow rate indicate that the plasma chemistry is strongly dependent on the energy density supplied per monomer molecule, also known as a Yasuda parameter (P/F). To check this hypothesis, the dependence of the elemental composition of all the coatings prepared in nitrogen on the P/F ratio was plotted and is shown in Figure 36. It can be seen that the increase of the discharge power influences the chemistry of coatings in a similar way as the decrease of the flow. At high P/F (the monomer deficient regime), the coatings are rich with Ti and O and contain the minimum concentration of carbon and nitrogen. On the other hand, coatings prepared at the power deficient regime are more organic.

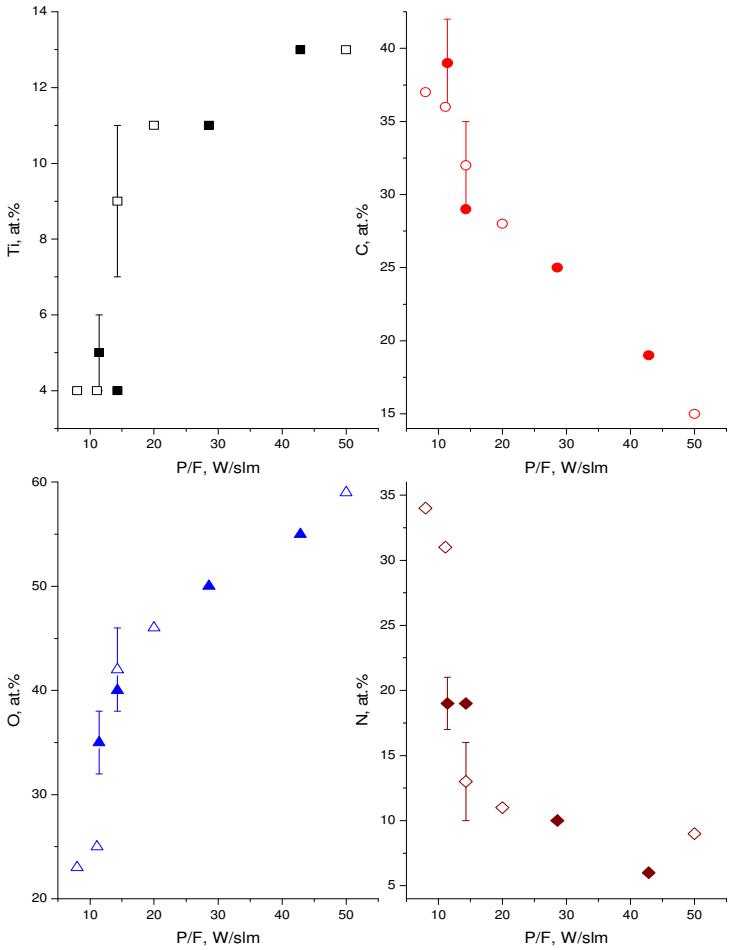

Figure 36. The elemental composition of the deposits in dependence on the power-to-flow ratio. The solid symbols correspond to the series with varying power and fixed flow (N_2 0.7 slm, 20 min), the open symbols correspond to the series with varying flow and fixed power (20 W, 20 min).

The dependence of the elemental composition is confirmed also by the deconvolution of the C 1s XPS peak of the previous sample shown in Figure 37. The increase of the P/F ratio results in the higher amount of the C-C/C-H bonds in the coatings. Taking into account the high concentration of oxygen in these coatings, one can suggest that most of oxygen is bound to titanium in TiO_2. Almost no dependence of the O-C=O bonds on the P/F ratio was revealed. The increase of the signal from hydrocarbons was accompanied by the reduction of the C-O/CN and the C=O/N-C=O groups. These changes correlate with the decrease of the total amount of nitrogen in the coating. Thus, nitrogen-containing species play the dominant role in the formation of the plasma polymer phase.

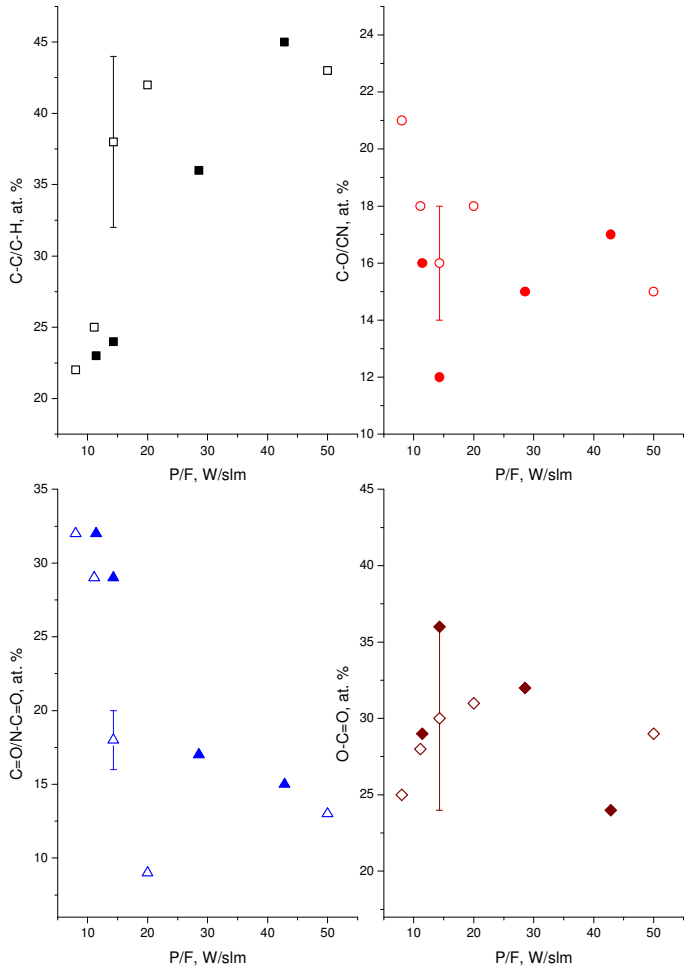

Figure 37. The dependence of various components in the C 1s spectra on the P/F ratio. The solid symbols correspond to the series with varying power and fixed flow (N_2 0.7 slm, 20 min), the open symbols correspond to the series with varying flow and fixed power (20 W, 20 min).

It was found that the morphological changes of the coatings prepared in N_2 are also correlated with the P/F ratio. The SEM cross-sections and the top views of the samples prepared at different powers and nitrogen flows but with the similar P/F ratio are shown in Figure 38. The coatings in the right column were deposited at the power of 8 W and the flow of N_2 of 0.7 slm. These experimental conditions give the P/F ratio of 11 W/slm. The SEM images in the left columns correspond to the coatings with P/F= 14. In this case, the samples were deposited at 20 W power and 1.4 slm flow of N_2. It can be seen that both coatings have almost identical porous structure. They are comprised of the particles with the mean size of 40 nm.

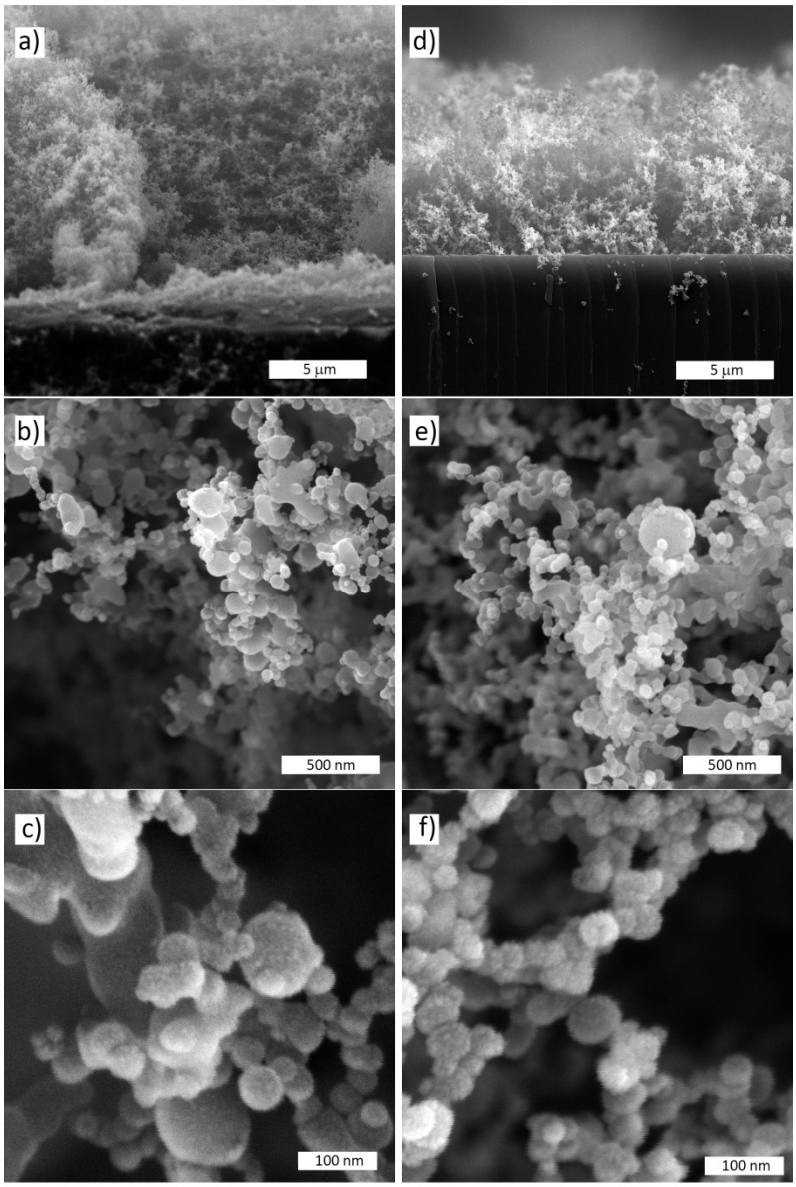

Figure 38. The cross-section a) d) and top view b) c) e) f) SEM images of the coatings deposited at 8 W, 0.7 slm N_2 (left column) and 20 W, 1.4 slm N_2 (right column). The P/F ratios are close and equal to 11 and 14 W/slm, respectively. The deposition time is 20 min for both coatings.

In contrast, Figure 39 shows the SEM images of the coatings prepared under different values of P/F. The coatings fabricated at 20 W power and 2.5 slm flow of N_2, which gives the P/F=8 W/slm, are shown in the left column. The images in the right column correspond to the coatings prepared at P/F= 43, where the highest power (30W) and one of the lowest flow rate of N_2 (0.7 slm) were used. The clear difference in the structure of the obtained deposits is seen. The coating deposited at

P/F= 8 W/slm are more compact and characterized by much less porosity than the coating prepared in the monomer deficient regime at P/F= 43 W/slm.

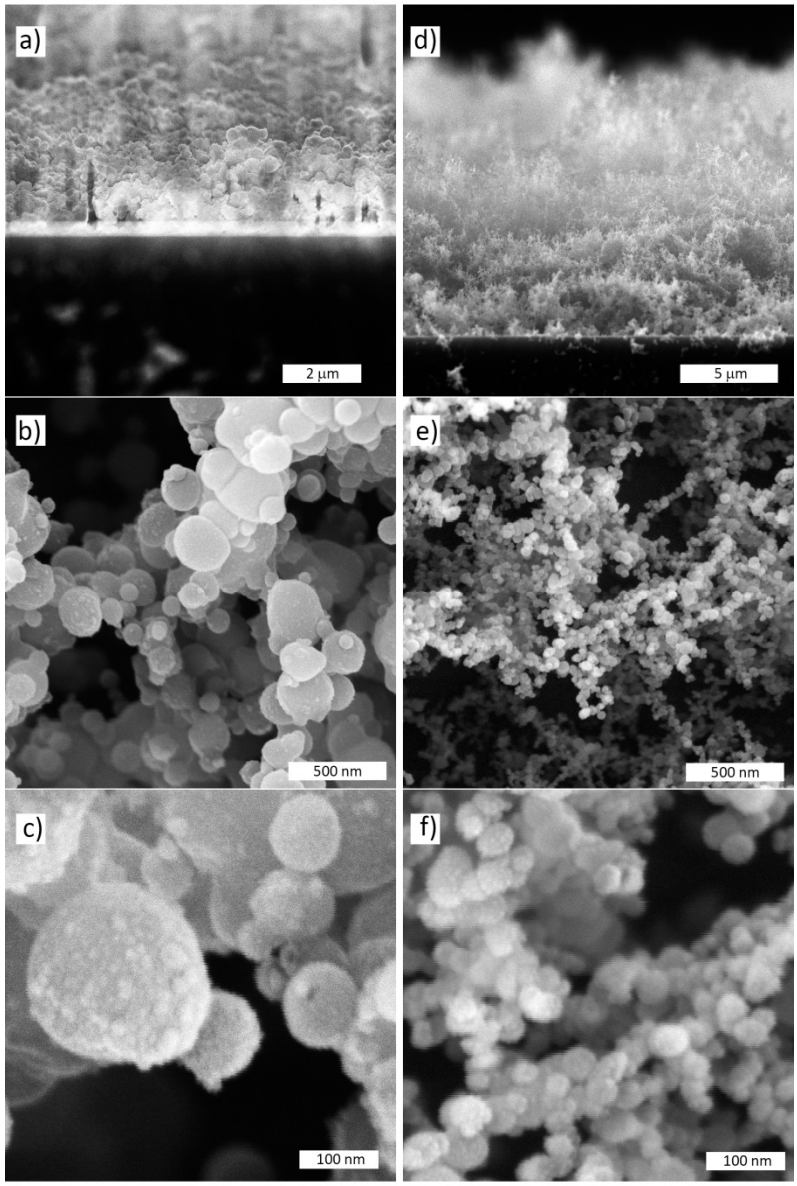

Figure 39. The SEM cross-section a) d) and top view b) c) e) f) of coatings deposited at small P/F=8 W/slm (20 W, 2.5 slm N_2, left column) and high P/F=43 W/slm (30 W, 0.7 slm N_2, right column). The deposition time is 20 min for both coatings.

The agglomeration of big spherical particulates with the average size of 110 nm can be seen in the SEM images shown in Figure 39 b, c. Knowing that the coatings deposited at such conditions are mostly organic, it can be hypothesized that such particulates have a core-shell structure in which TiO_2 particles are enveloped by thick layers of the plasma polymer. The increase of the amount of energy per

monomer molecule significantly enhances the fragmentation of the precursor. The decomposition of TTIP results in the formation of volatile hydrocarbons and $Ti(O)_4$ species. Oxidized titanium forms inorganic nuclei which subsequently grow into particles. The volatile hydrocarbon compounds can be simply removed by the gas flow. Less drastic fragmentation of the precursor in the power deficient regime leads to better incorporation of organic species into the growing deposit.

The presence of the crystalline structure in the deposited coatings was studied by X-ray Diffraction. It was revealed that all the coatings were amorphous regardless the experimental conditions. The possibility to obtain crystalline TiO_2 by means of atmospheric pressure DBD deposition using TTIP was previously investigated in [116–120]. The authors observed that samples have to be heated during or after deposition to high temperature (minimum observed temperature was 150 °C) to prepare anatase-phase TiO_2 particles. The lack of thermal impact in our case was probably the main reason for the absence of crystallinity because the substrate temperature never exceeded 70 °C.

3.2. Formation of AlO_x nanoparticles using diagnostic gas aggregation cluster source

A newly developed diagnostic gas aggregation cluster source was applied for deposition of AlO_x NPs. In contrast to the other types of GAS used in this work, the diagnostic cluster source enables to move the aggregation chamber relatively to the diagnostic port while preserving the constant aggregation length. Such configuration allows to perform in-situ measurements in different positions inside the GAS. The scheme of the experiment is shown in Figure 40.

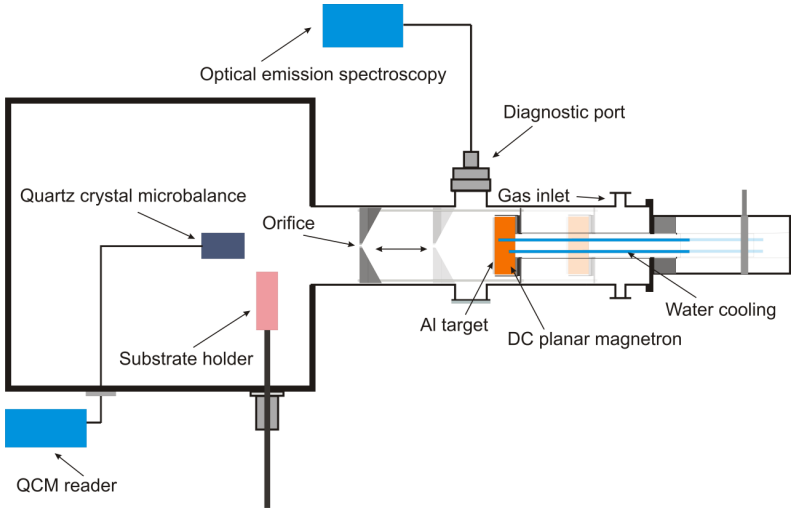

Figure 40. Scheme of the experiment.

The first stage of the experiment was devoted to searching for optimal experimental conditions which provide stable and reproducible deposition rate of Al NPs. Different values of pressure and magnetron current were tested. The deposition rate was monitored by QCM positioned 15 cm from the orifice. It was found that at constant magnetron current of 200 mA, the NPs are produced only within the range of pressures of 34-38 Pa, which corresponds to 6.0-6.3 sccm flow of Ar with the orifice diameter of 3 mm. However, even under these conditions, the deposition rate of the NPs was not stable and decreased with time (Figure 42). Similar trends in the deposition rate were observed previously during the deposition of different metallic NPs [121–123].The authors suggested that it is the presence of oxygen-containing compounds that significantly influences the deposition process of metallic NPs. It is worth noting that their investigations were performed *ex-situ*. In contrast, the use of

the diagnostic GAS allows not only to study the common deposition characteristics but also gives additional information about the initial stages of the NP formation.

In the next experiments, a certain amount of O_2 was gradually added to Ar. For each percentage of oxygen, the deposition rate and the magnetron voltage were measured until their value become stable. The obtained data were then averaged for the period of the measurement (Figure 41 a, b). Simultaneously, optical emission spectra were taken at the constant 2 cm distance from the magnetron. The most intensive spectral line of Al I at 396 nm and O I at 777 nm were chosen for the analysis. The time evolution of the aluminum and oxygen spectral lines in dependence on the oxygen percentage is presented in Figure 41 c, d. The analysis of the obtained results shows that the deposition process of NPs is extremely sensitive to even smallest concentration of oxygen in the mixture.

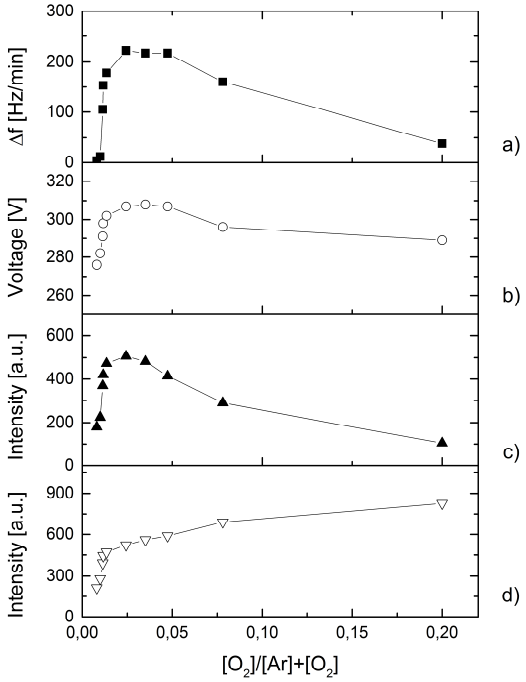

Figure 41. Representation of a) the deposition rate, b) the magnetron voltage, c) the intensity of Al I (396nm) and d) O I (777nm) atom spectral lines on the oxygen ratio in the working gas mixture.

It can be seen in Figure 41 a, b that the deposition rate and the voltage gradually increase with the oxygen concentration increasing up to about 3-5 %. The possible explanation of the observed dependence can be found in the fundamental knowledge about reactive magnetron sputtering. The introduction of small amount of

oxygen into the GAS induces the partial oxidation of the surface of the target [124]. Since the discharge is operated at constant current, the oxidation leads to the increase of the voltage and, subsequently, of the energy of Ar ions. More intensive bombardment of the target increases the amount of sputtered material and promotes the formation of NPs. The observed results are also confirmed by the in-situ OES measurements. The intensity of the Al spectral line increases with the addition of oxygen and fully repeats the trend of the deposition rate. The signal of O I shows the linear elevation. The further increase of oxygen from 5 to 20 % induces the abrupt decline of the magnetron voltage and the deposition rate of Al NPs. Apparently, such oxygen concentration is excessive and it causes the complete oxidation of the target which hinders sputtering. Simultaneously, the drop of the signal from the Al spectral line is observed. It is interesting that this trend is opposite to what was observed for the deposition of TiO_x NPs for which the voltage raised almost linearly with the addition of oxygen. The decline of the voltage under the excessive amount of oxygen can be another evidence for the formation of the oxide layer on top of the target. According to the work of Depla et.al [125], the above observed dependence is typical for reactive sputtering of aluminum and can be explained by the modification of the topmost surface of the target by implantation of reactive oxygen ions. These ions interact with atoms of the target and, as a result, the AlO_x layer is formed. Due to the difference in the electron emission yield, which is higher for AlO_x as compared with pure Al [125], the decrease of the voltage is observed.

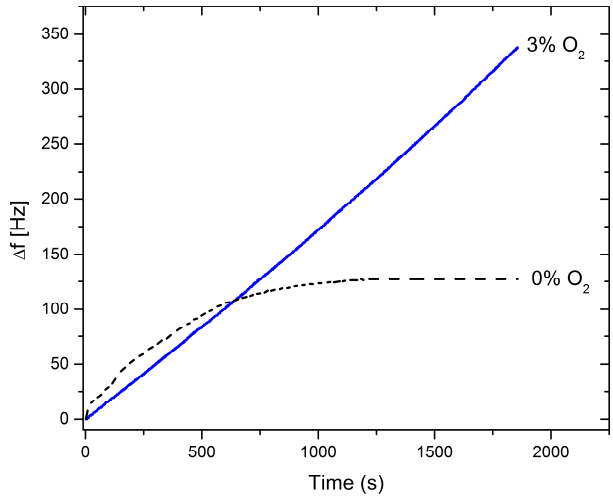

Figure 42. QCM signal proportional to the amount of deposited mass as measured using pure Ar or Ar/O_2 working gas mixture.

The addition of oxygen has an impact not only on the effective growth rate but also on the stability of the deposition process in time. The comparison of the deposition rate of Al NPs prepared without and with the addition of 3% of oxygen reveals much better stability of cluster formation in the latter case, Figure 42.

Investigation of the influence of the working gas mixture on the chemical composition of NPs was performed by XPS. The AlO_x NPs prepared at minimum concentration of O_2 (0.5 %) was compared with those deposited at 3% of oxygen in the working gas mixture. Both samples were transferred to the XPS chamber immediately after the deposition without breaking vacuum. The high resolution XPS spectrum of the oxygen-deficient sample shows that the NPs contain at least 15 % of metallic Al (74.2 eV [126]) and the rest 85 % correspond to Al_2O_3 bonds (74.4 eV) (Figure 43). On the other hand, the NPs prepared at higher content of O_2 are fully oxidized and just a single peak of Al_2O_3 is detected [127]. The presence of carbide bonds is not observed in either of the cases.

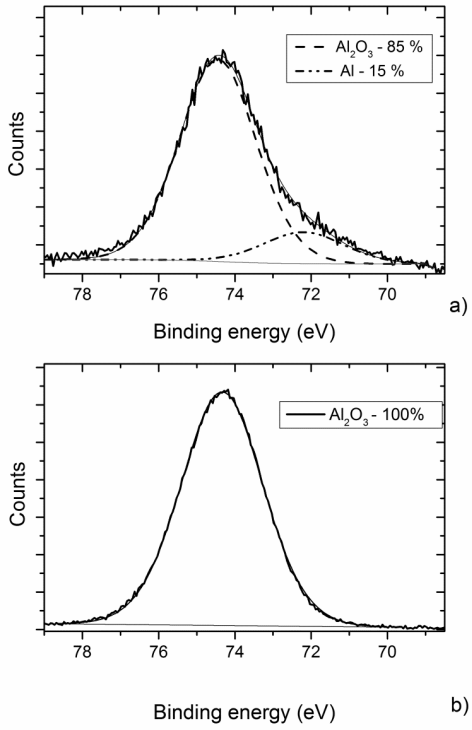

Figure 43. High resolution XPS spectra of Al/AlO NPs deposited with a) and without addition of oxygen b).

In addition to the above studied parameters, the *in-situ* investigation of the NP formation was also performed. First, the morphological evolution of the NPs

during their growth inside the GAS was studied. All the depositions were performed at the constant aggregation length of 10 cm, the magnetron current of 200 mA and the pressure in the aggregation chamber of 40 Pa. To stabilize the deposition rate of the NPs, 3% of oxygen was added to the working gas mixture. The set of the samples was deposited in the aggregation chamber at different distances from the magnetron (4, 8, 10 cm). Obviously, the closer distance to the magnetron is of high interest since it can give important information about the initial stage of the NP growth. To minimize the possible perturbations in plasma which could be induced by introducing the substrates, silicon wafers were grounded and positioned parallel to the wall of the GAS. Unfortunately, placing the samples to the distance closer than 4 cm from the magnetron immediately caused the change of the plasma parameters, which were reflected in alterations of the deposition rate. The investigation of the structure of the NPs was done by SEM.

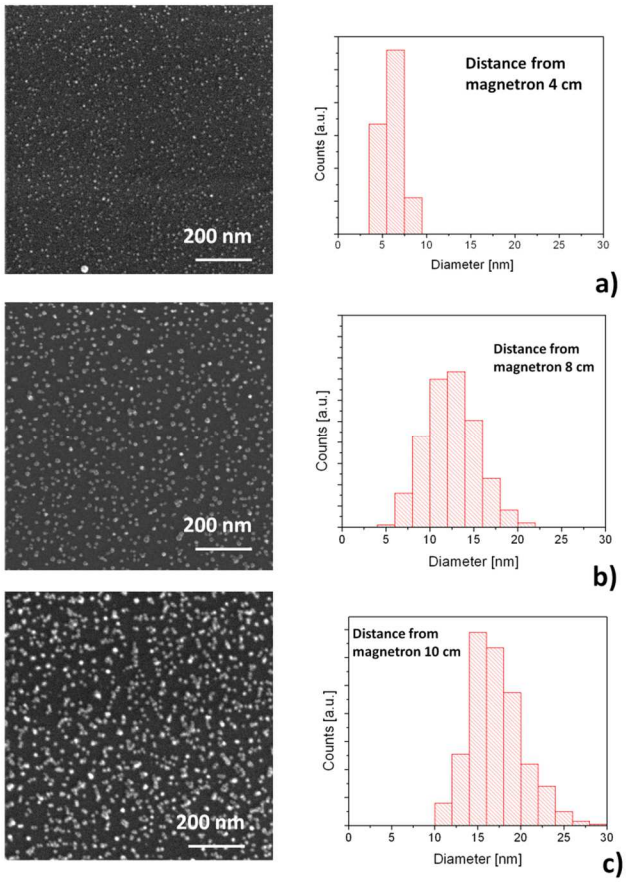

Figure 44. Top view SEM images and corresponding size histograms of NPs deposited at different distances from the target in the aggregation chamber at a) 4cm b) 8 cm and c) 10 cm from the magnetron.

It can be seen in Figure 44 that the NP size increases from 6 ± 1 nm (4cm) up to 16 ± 3 nm (10 cm) with the distance. This result confirms a theoretical hypothesis according to which the growth of NPs runs continuously on their way from the magnetron to the orifice.

The possibility to perform the study at different positions inside the GAS was also used in the OES measurements. These were performed under the same experimental conditions (44 Pa, 200 mA, 3% oxygen fraction in the Ar/O_2). The most intense spectral line of Al at 396 nm, O at 777 nm and numerous Ar spectral lines were detected. Despite very fast decrease of the intensity of the radiation with distance, the non-negligible amount of oxygen atoms was detected even at 5 cm from the magnetron. This result may indicate that the oxidation of Al NPs occurs also in the afterglow region (Figure 45).

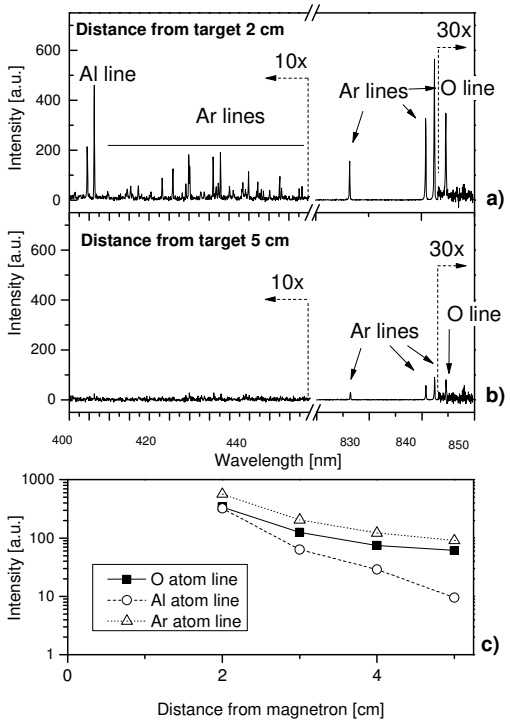

Figure 45. Optical emission spectra obtained at different distances from the magnetron during the deposition of AlO_x NPs.

3.3 SiO_x (CH) nanoparticles with tunable properties

Gas aggregation cluster sources were typically used for the production of metal or metal oxide NPs. Recently, it has been shown that the number of the possible materials are not limited to metals but GAS can be successfully applied for the fabrication of plasma polymer NPs including hydrocarbon, fluorocarbon and nitrogen-containing plasma polymer NPs [128–131]. In this part of the thesis, the possibility to prepare organosilicon NPs was investigated.

3.3.1 Application of size-differentiated organosilicon nanoparticles for deposition of biomimetic structure

The deposition of the CHSiOx NPs

In this experiment, the same type of the GAS was applied which was previously used for the deposition of Ti NPs. The scheme of the experimental setup is shown in Figure 46. The RF (13.56 MHz), water cooled, planar magnetron equipped with a 1 mm thick graphite target was used as a power source for PECVD. The holder of the electrode enabled to change the distance between the target and the orifice (without breaking vacuum) from 15 to 4 cm. The GAS was connected to the main deposition chamber that was pumped down by diffusion and rotary pumps.

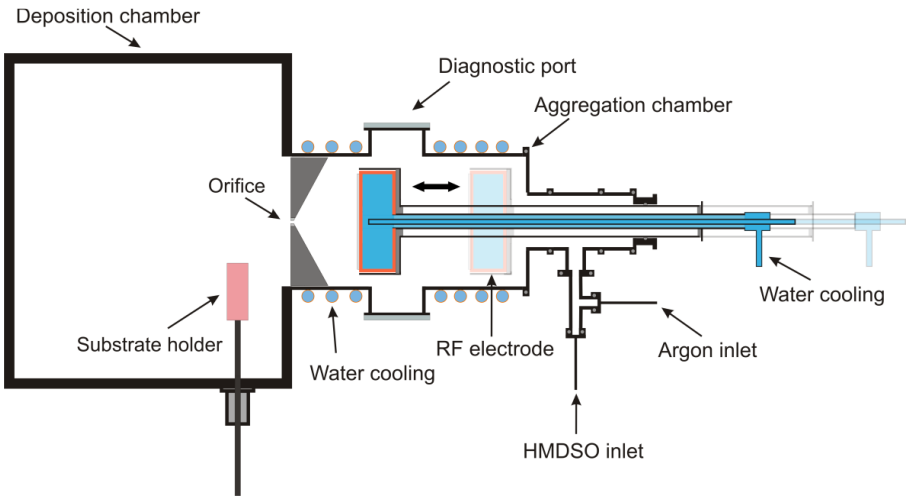

Figure 46. The scheme of the experimental setup used for deposition of the $CHSiO_x$ NPs

Various Ar/HMDSO/O_2 working gas mixtures were introduced into the gas aggregation chamber. The fraction of each component was adjusted by changing the flow rate of the corresponding gas, except for Ar the flow of which was kept constant at 2 sccm. The pressure in the deposition chamber (2 Pa) was optimized to produce high deposition rate of NPs and it was kept constant during all the following experiments. The first experiments showed that the relatively small pressure (44 Pa) and power (30W) were able to provide stable and reproducible deposition of NPs from the Ar/HMDSO (10:1) mixture. The deposition rate was calculated as amount of NPs per area and time based on the analysis of the SEM images.

In the next investigations, the influence of the discharge power, the pressure in the GAS and the aggregation length on the properties of the NPs was studied. The XPS analysis showed that the chemical composition of the coatings does not depend on the mentioned experimental conditions and it is typical for plasma polymerized HMDSO thin films. On the other hand, significant changes of the morphology of the NPs were observed.

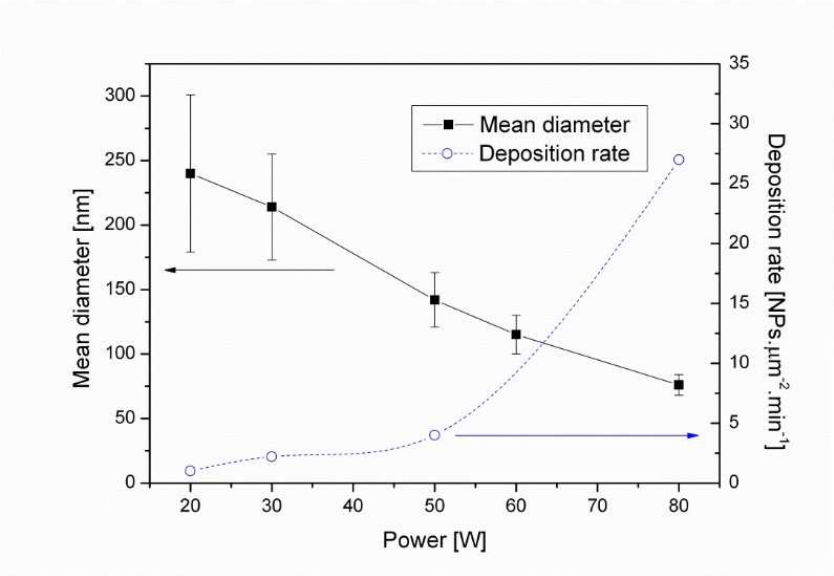

Figure 47. Dependence of the mean diameter of the NPs and their deposition rate on the power.

It was revealed that the discharge power has a very strong effect on the deposition rate and the size of the NPs. The increase of power from 20 W to 80 W led to the increase of the deposition rate from 1 to 26 NPs/$\mu m^2 \times$min which was accompanied with a threefold decrease of the mean size (Figure 47 and Figure 48).

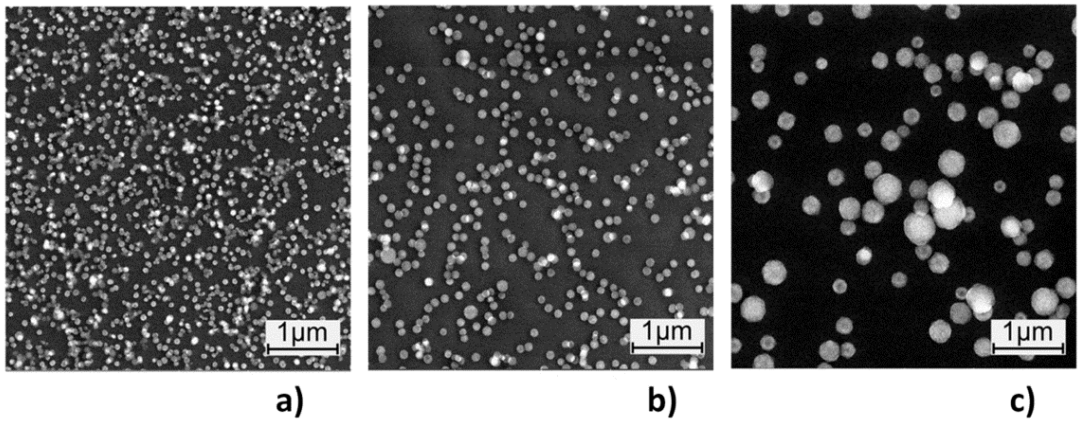

Figure 48. Top view SEM images of the NPs prepared at different power: a) 80 W; b) 50 W and 20 W.

The change of power has also an impact on the homogeneity of the coatings. The size distribution of the NPs deposited at higher power is much narrower than in case of the coatings prepared at 20 W. Such effect of power on the size distribution was also observed for the nylon-sputtered and CH_x plasma polymerized NPs [129–131] deposited by GAS. Obviously, higher power delivered to the discharge produces more active radicals which subsequently recombine and create nucleation centers for subsequent NP growth.

In the following experiments, the influence of the pressure (at constant Ar/HMDSO ratio) in the aggregation chamber on the properties of the NPs was explored. Increasing of the pressure from 25 to 92 Pa resulted in the increase of the mean NP size from 189 to 286 nm. The coatings deposited at 62 – 92 Pa were very inhomogeneous and consisted of two groups of nanoparticles with the difference in the mean size reaching 150 nm. It has to be noted that the elevation of pressure had also a negative effect on the stability of the discharge. Moreover, thick deposits of NPs were observed inside the GAS. The increase of the pressure leads to the increase of the amount of monomer molecules in plasma. Excess of the monomer probably induced the formation of big NPs that precipitated due to gravitation inside the GAS chamber. Therefore, all the next experiments were performed at moderate pressure of 44 Pa.

One of the most important parameters in the production of NPs by GAS is the aggregation length. In our experiment, the distance between the magnetron and the orifice was changed from 10 to 4 cm with increments of 1 cm. All other experimental

parameters were kept constant. The shortening of the aggregation length considerably increased the number of particles per unit area and unit time (Figure 49).

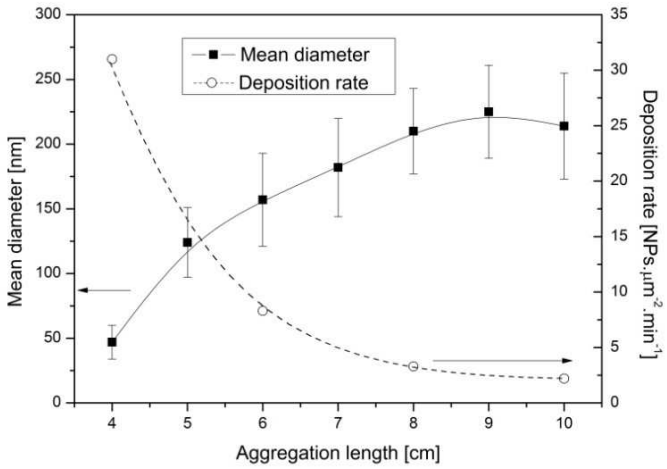

Figure 49. Dependence of the mean diameter of the NPs and their deposition rate on the aggregation length.

The increase of the deposition rate was accompanied by the reduction of the mean diameter of the NPs from 220 to 47 nm (Figure 50). Such changes indicate that the creation of new particle seeds is limited to the area close to the magnetron. The further growth of the NPs takes place during their travelling through the aggregation chamber via reaction with long living radicals and probably by coagulation processes. Therefore, the size of the NPs depends mostly on the residence time in the cluster source that is given by the gas flow and the aggregation chamber length.

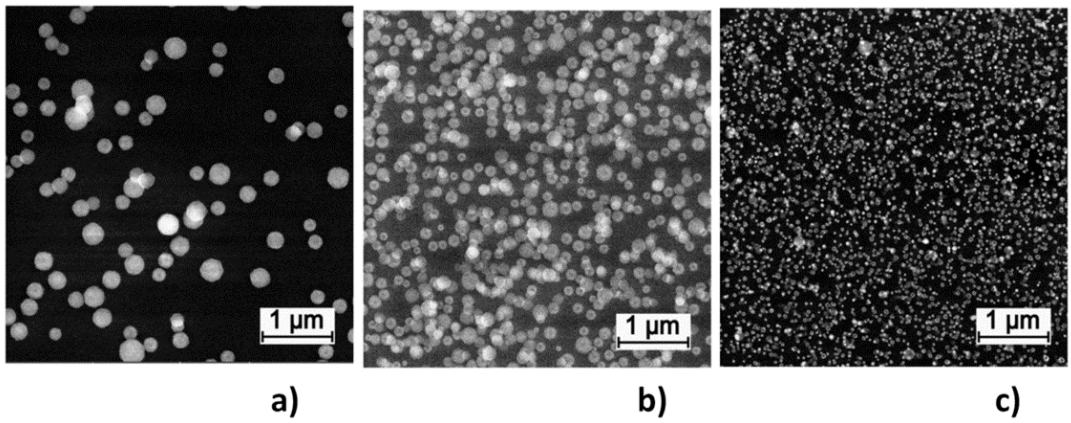

Figure 50. Top view SEM images of NPs prepared at different aggregation chamber length: a) 10 cm; b) 6 cm and c) 4 cm.

The similar effect was already observed for nylon-sputtered NPs, where the residence time was changed not only by the decrease of the aggregation length but also by the increase of the flow of the carrier gas at constant pressure in the cluster source.

The preparation of biomimetic coatings with multi-scale roughness

Biomimetic surfaces are nature-inspired structures with a huge application potential. Nowadays, these materials are actively developed and investigated. Fabrication of structured surfaces in which the size of the structural elements covers a broad range of scales is of high scientific interest. Such structure may mimic outstanding optical and wetting properties of surfaces found in nature: for example, antireflection of the eye of a nocturnal moth or self-cleaning superhydrophobic and antifogging superhydrophilic coatings characteristic for lotus leaves, rose petals, feathers of birds, gecko paws etc.

In the next experiments, NPs of different size were produced and used as building blocks for the fabrication of the surfaces with multi-scale roughness. Two different experimental approaches were tested. In the first case, the NPs of different size were deposited by changing the aggregation length. The base layer was formed by the 220 nm NPs prepared at the aggregation length of 10 cm with the fluence of 10 μm^{-2}. After that, the aggregation length was shortened to 4 cm and NPs with the mean size of 40 nm were deposited on top of the base layer. The amount of the big NPs was constant while the amount of the small NPs was changeable and controlled by the deposition time at the constant flux. The coatings were deposited with 180 μm^{-2} and 310 μm^{-2} fluence of the small NPs and are shown in Figure 51.

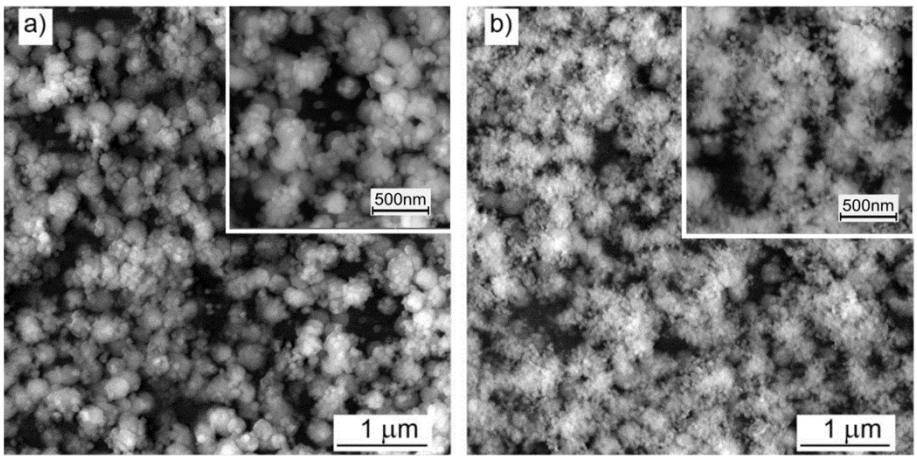

Figure 51. The top view SEM images of the coatings with dual-scale roughness deposited by overcoating of 220 nm NPs with 40 nm NPs with the fluence of: a) 180 μm^{-2} b) 310 μm^{-2}.

Another experimental approach was based on the regulation the size of NPs by the discharge power. The power was increased sequentially from 30 W to 90W in three 30 W steps. The deposition lasted for 1 min for each value of the power. It can be seen in Figure 52 that the resultant coating consists of three kinds of NPs with the size of 200, 110 and 70 nm. Thus, the coatings with multi-scale roughness can be produced using these NPs.

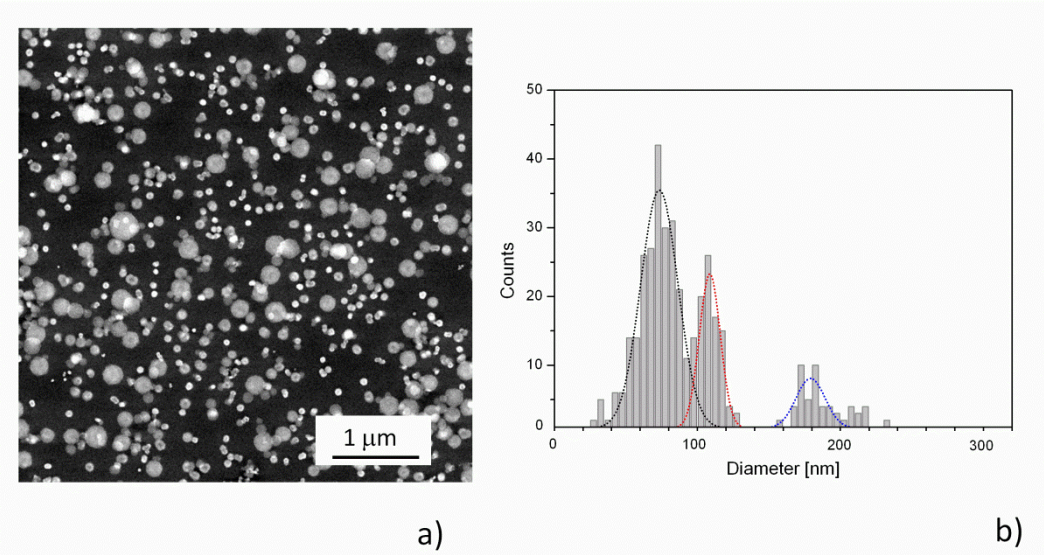

Figure 52. The top view image and the size distribution diagram of the coating made by the sequential three step deposition of 200 nm, 110 nm and 70 nm NPs at 30, 60 and 90 W discharge power, respectively, other parameters held constant.

It is well known that NPs prepared in the soft-landing regime have poor adhesion to substrates. They can be easily swept away from the surface, which impedes the implementation of such coatings in real applications. In order to solve that problem, a thin capping layer of plasma polymer was deposited over the NPs. Plasma polymers can be prepared as highly cross-linked, pinhole–free layers that are capable of fixing the loosely adhering NPs on the substrate. The chemical composition of such films can be adjusted according to the requirements of the ultimate goal.

The comprehensive investigation of the wettability behavior of the coatings consisted of the CH(SiO_x) NPs overcoated by either hydrophilic or hydrophobic thin films was done. The first part of the study was focused on the coatings with the single-scale roughness.

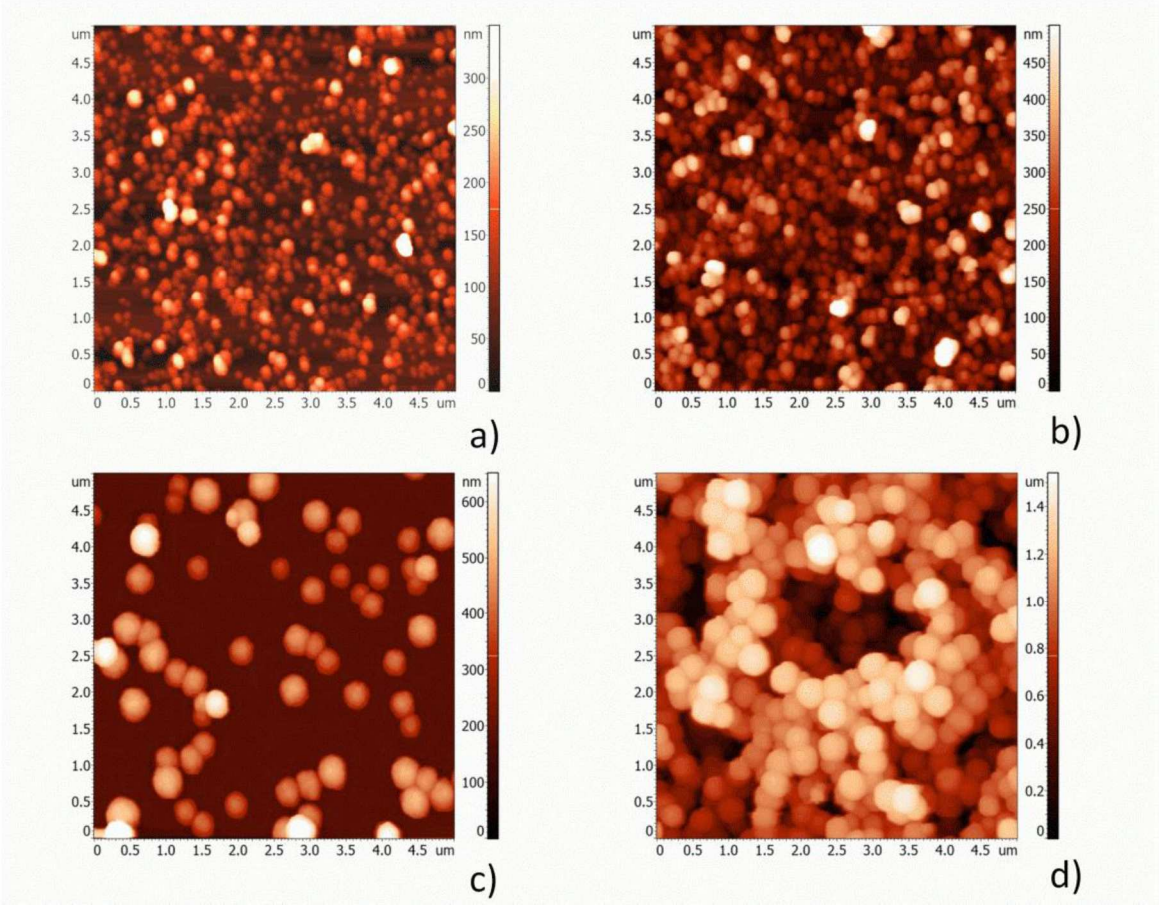

Figure 53. The AFM scans of the (C:H):SiO_x NPs overcoated with 25 nm thick SiO_x films: a) 100 NPs/μm^2 with diameter 70 nm, b) 400 NPs/μm^2 with diameter 70 nm, c) 2 NPs/μm^2 with diameter 220 nm and d) 22 NPs/μm^2 with diameter 220 nm.

The range of the samples with different amount of 220 nm and 70 nm NPs were overcoated by 25 nm thick hydrophobic (C:H)SiO_x or hydrophilic SiO_x thin films. The AFM images of the coatings covered with SiO_x thin films are shown in Figure 53. The wettability analysis of the prepared samples was made by water contact angle measurements. It was found that all coatings covered with SiO_x thin films were superhydrophilic, regardless of the amount of the NPs. On the other hand, the wetting behavior of hydrophobic coatings was more complex. In this case, the surface topography was characterized by the area ratio r, which enters the Wenzel equation [132] and can be calculated from the AFM data. Interestingly, the coatings with the same surface area ratio can be achieved by deposition of either small or big particles with appropriate fluence.

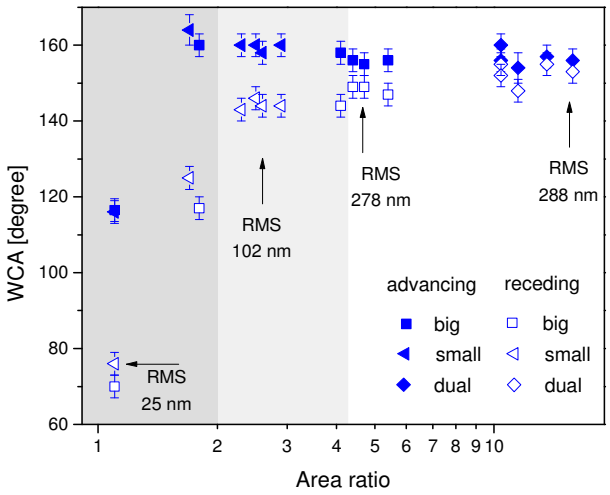

Figure 54. Advancing and receding WCA measured on the coatings consisted of small (70 nm), big (220 nm) and dual scale (constant amount of big and different amount of small) NPs subsequently overcoated with hydrophobic plasma polymer film. The shaded areas from left to right correspond to the Wenzel hydrophobic, the superhydrophobic „sticky“ and the superhydrophobic „slippery“ regime.

It can be seen in Figure 54 that the coatings with a small fraction of NPs on the surface are characterized by high water contact angle hysteresis, which declines with the increasing area ratio. Moreover, the coatings with r~2 are highly adhesive to a water droplet. The liquid droplet stays stuck to such surfaces independently on the tilt of the substrate (see Figure 55). The samples prepared with longer deposition

time are superhydrophobic with lower hysteresis of WCA. The same investigation of wettability was made on the samples with dual scale roughness. In this case, the deposition of structure composed the two different groups of particles resulted in the formation of very developed surfaces with the extremely high area ratio of r > 10. The samples were also overcoated by SiO_x or HMDSO thin films and the water contact angle was measured. Independently on the fraction of particles, the hydrophobic coatings demonstrated the self-cleaning properties with very low WCA hysteresis. At the same time, the samples coated by SiO_x were superhydrophilic.

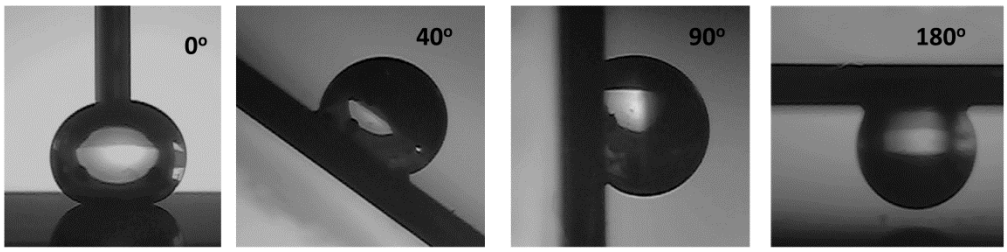

Figure 55. The images of water droplets on the "sticky" superhydrophobic surface

3.3.2 The influence of oxygen on the properties of the deposited coatings

The next step of the experiment was to investigate the possibility of deposition of SiO_x NPs using HMDSO as a precursor. For this purpose, a well-known technology of fabrication of SiO_x thin film by PECVD was applied based on the addition of oxygen to the mixture of Ar and HMDSO during the deposition [99]. The power and the composition of the Ar/HMDSO mixture were kept constant whereas the percentage of O_2 was gradually increased. The deposition time was adjusted in order to achieve comparable NPs surface density (coverage) for all the samples.

The study of the morphology revealed that the NP size does not depend significantly on the amount of added oxygen. The biggest mean diameter of 218 nm was observed for the coating deposited at minimum O_2/HMDSO ratio of 1. The elevation of the oxygen flow by 0.3 sccm has led to a slight reduction in size to 169 nm. The further increase of the O_2/HMDSO ratio has little effect on the size distribution of the NPs and their mean diameter was approximately 180 ±14 nm.

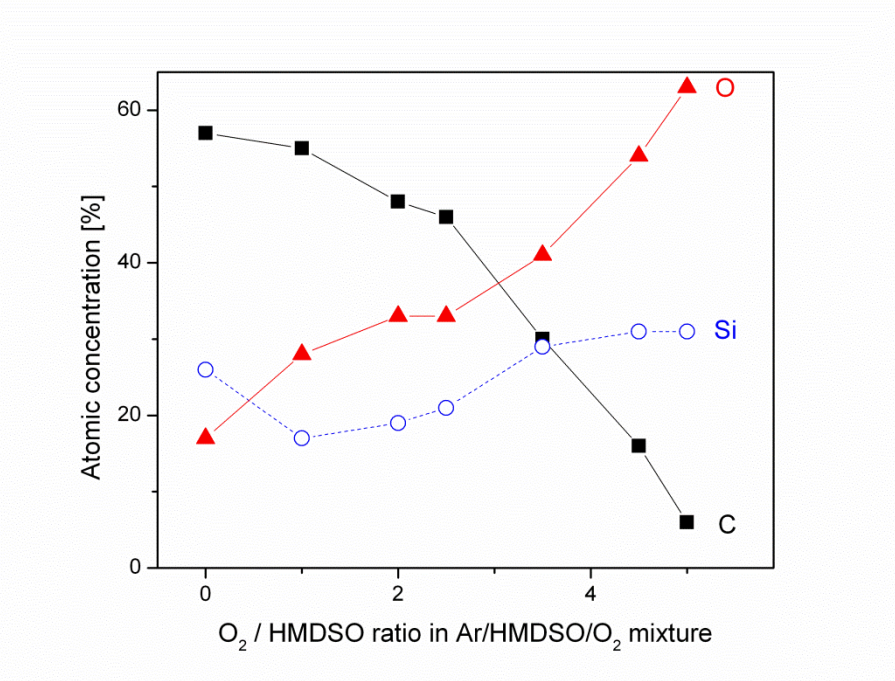

Figure 56. Chemical composition of NPs in dependence on the O_2/HMDSO ratio as determined by XPS.

In contrast to the morphological changes, the addition of oxygen into the cluster source caused the significant alteration of the chemical composition of the NPs. Figure 56 comprises the results of the XPS measurements of the NPs prepared at different O_2/HMDSO ratio. For the Ar/HMDSO mixture without oxygen, the NPs have the chemical composition typical for silicon-containing plasma polymers with plenty of hydrocarbon species. The addition of O_2 leads to the gradual growth of the silicon and oxygen content. At the same time, the concentration of carbon rapidly decreases from 57 down to 6 %. This decrease is in a good agreement with the changes of C/O-/Si and O/Si ratio (Table 3). It is obvious that the amount of carbon-containing bonds decreases with the increase of the oxygen percentage, while the oxygen-to-silicon ratio gradually increases and gains the value of 2, which corresponds to stoichiometric SiO_2. A small amount of carbon detected in this case can be explained by impurities deposited on the coatings during their transfer to XPS through the atmosphere.

O_2 / HMDSO ratio	C/O	C/Si	O/Si
0	4.00	3.42	0.84
1	1.96	3.24	1.65
2	1.45	2.53	1.74
5	0.10	0.19	2.03

Table 3 : The C/O, C/Si and O/Si ratio in dependence on the O_2/HMDSO ratio.

The changes in the chemical composition are also confirmed by the analysis of the high resolution Si 2p and C 1s spectra. First of all, it was observed that the position of the silicon peak shifted from 102.0 eV (without O_2) to 103.8 eV (O_2/HMDSO – 5:1) (Figure 57).

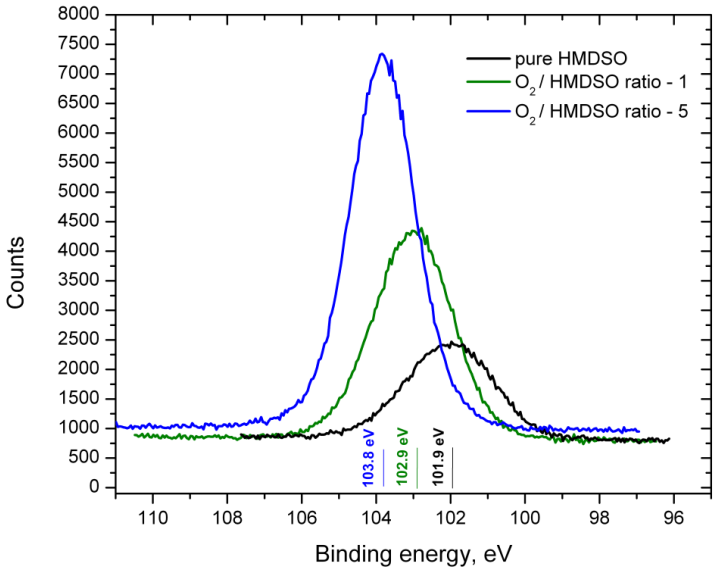

Figure 57. The evidence of the shift of the Si 2p peak with increasing of the O_2/HMDSO ratio.

This fact is an additional proof of the significant transformation of silicon surrounding environment. The variety of possible chemical bonds of silicon with oxygen and hydrocarbon species, which possess similar binding energy, is the main reason for poor resolution of individual components in the Si 2p spectrum. Therefore, the analytical approach proposed by Alexander et al. [133] was used for the quantification of high resolution spectra. The main idea is that a number of

oxygen atoms bond to silicon should be used as a key parameter, with an assumption that all atoms of Si have the valence of 4. Thus, the Si 2p high resolution spectrum was deconvoluted by four components: $Si(-O)_1$ – 101.5 eV; $Si(-O)_2$ – 102.1 eV; $Si(-O)_3$ – 102.8 eV; $Si(-O)_4$ – 103.4 eV.

It can be seen in Figure 58 that the silicon spectra of polymeric particles are dominated by the Si $(-O)_{1-3}$ components. Interestingly, even in the case of HMDSO without O_2, the Si $(-O)_4$ bonds were detected.

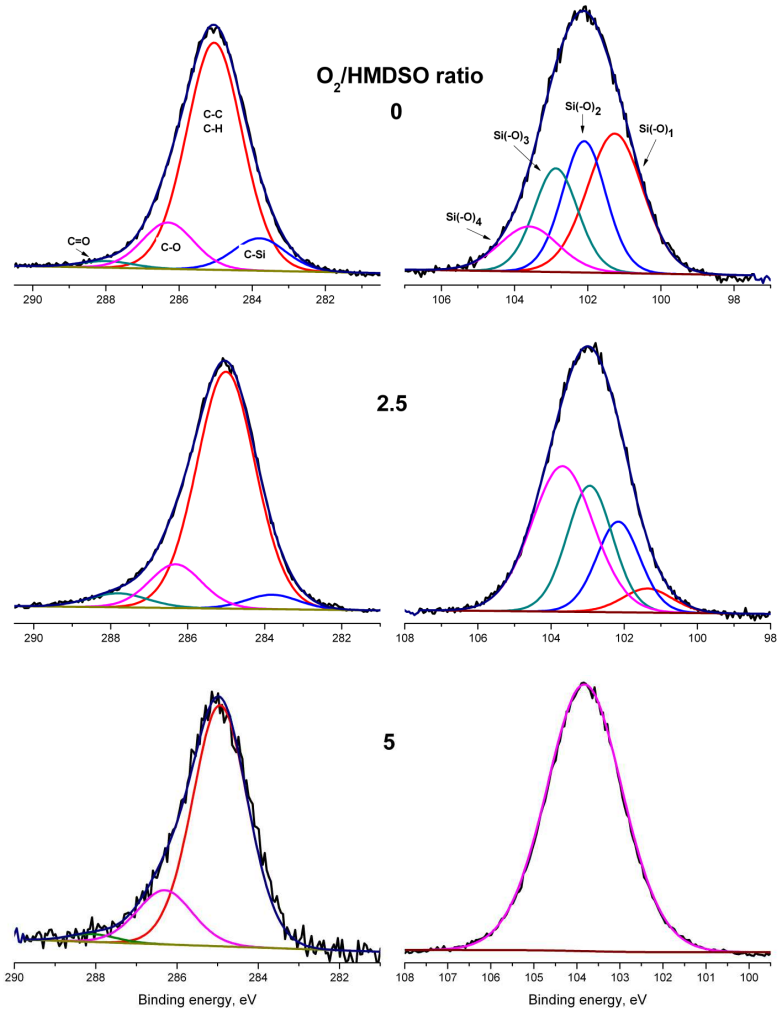

Figure 58. The high resolution C1s and Si 2p spectra of $SiO_x(CH)$ nanoparticles deposited at different O_2/HMDSO ratio.

The fitting of the C1s peak reveals four components corresponding to C-C, C-H (285.0 eV); C-O (286.5 eV); C=O (288.0 eV) and C-Si (283.6 eV) [134]. It was observed that the most abundant component originated from the hydrocarbon bonds. The small amount of the C-O and the C=O groups points at the slight oxidation of

the plasma polymer. The addition of oxygen to the gas mixture induces the increase of the Si $(-O)_4$ percentage with the simultaneous decrease of the amount of other bonds. At the maximum O_2/HMDSO ratio of 5, the Si $(-O)_4$ bonds become dominant and completely replace all other groups.

These observations were further confirmed by the FT-IR analysis of the deposited samples presented in Figure 59. For the samples prepared without O_2, the most intense absorption bands were observed for the Si-C (800 cm^{-1}, 842 cm^{-1}), the Si-O (1000-1100 cm^{-1}) and the CH_x groups (1408 cm^{-1}, 2900-2960 cm^{-1}). The addition of O_2 resulted in the significant attenuation and even disappearance of the signal from the organic components, and provided the spectrum consisting almost exclusively of the Si-O absorption band.

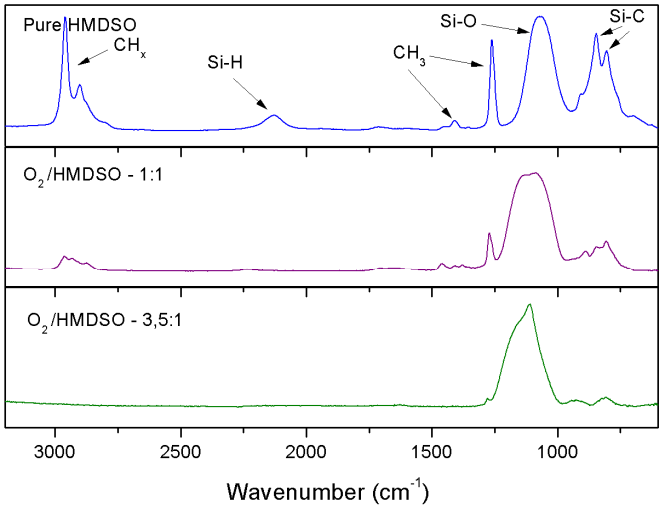

Figure 59. The FTIR spectra of NPs deposited at various O_2/HMDSO ratio.

3.4 Nanoparticles as growth seeds for glancing angle deposition of nanostructured coatings

In this experiment, the nanostructured coatings were prepared using plasma polymer particles produced by Gas Aggregation Cluster Source in combination with Glancing Angle Deposition of thin films. For both processes, RF magnetron sputtering of nylon 6,6 (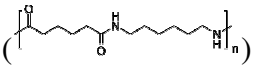) was used. A simplified scheme of the two-step experiment is described in Figure 60. For the production of NPs, the GAS with a semi-hollow magnetron was operated at 60W of RF pulsed power (frequency 1Hz, duty cycle 90%) and at 50 Pa pressure of Ar. NPs of a generalized composition of C:H:N:O were deposited onto silicon substrates.

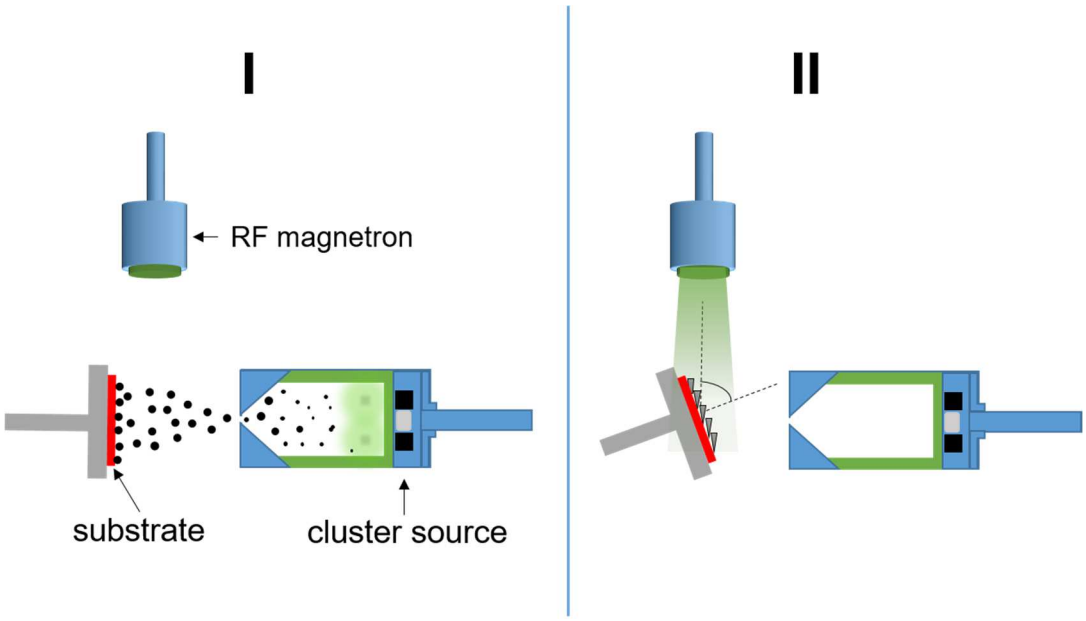

Figure 60. Schematic drawing of the two-step deposition the nylon-sputtered GLAD structures: I – the sub-monolayer of nylon-sputtered NPs was deposited; II – the layer of the NPs was subsequently overcoated by the nylon-sputtered thin film.

In the second step, thin films of plasma polymer were deposited over the seeds of the NPs at a glancing angle. A long-throw magnetron was specially designed to allow the nylon sputtering at a decreased pressure of 0.2 Pa. Nitrogen at the constant flow of 5 sccm was used as a carrier gas. Operation at lower pressure

was chosen to enhance the shadowing effect by diminishing scattering of the sputtered fragments by the carrier gas molecules. The optimal value of the RF power was found to be 40W. The use of higher power was limited because of the overheating of the polymer target at longer depositions. Since the deposition rate of the sputtered nylon films depends not only on the main discharge parameters but also on the deposition angle, the corresponding calibration procedure was done. A series of the samples was deposited at different angles, each for 10 min, and the thickness was subsequently measured by ellipsometry. Given the thickness and the deposition time, the growth rate was calculated for each of the deposition angle.

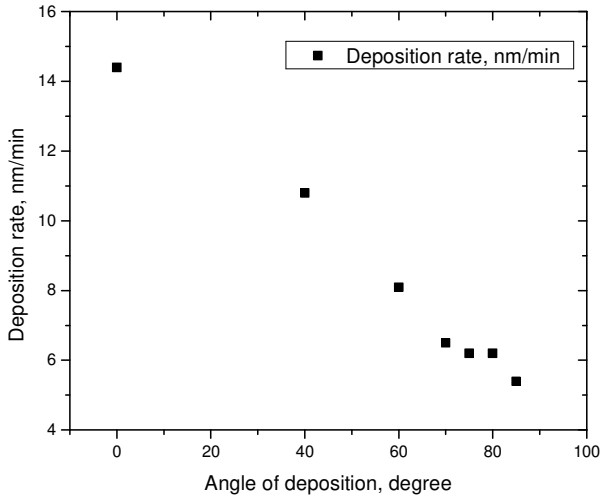

Figure 61. Deposition rate in dependence on the angle of deposition
Experimental conditions: Flow of nitrogen – 5 sccm; Power – 40 W;
Pressure – 0.2 Pa.

It can be seen in Figure 61 that the increase of the deposition angle induces the linear decrease of the deposition rate of the thin films. This result helped to adjust the deposition time in such a way that the films had the identical thicknesses of 600nm. It has to be noted that in addition to the samples with pre-seeded NPs, bare silicon wafers was also placed on the substrate holder as reference samples. Thus, both bare Si and Si pre-seeded with NPs samples were prepared at the same experimental conditions.

First, the nylon-sputtered thin films deposited on blank Si wafers were studied. For comparison, the top and the cross-section SEM images of these films prepared at 0° (left column) and 80° (right column) are shown in Figure 62. It can be

seen that the coatings produced in the normal position to the incoming flux are compact and do not show any distinct structural peculiarities. For the large deposition angle, the formation of the columnar structure is visible. However, no separate columns were detected and the films preserved the compact structure.

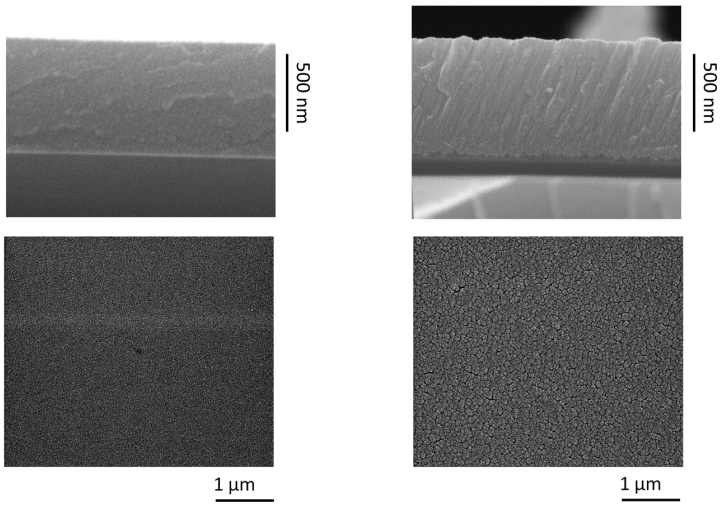

Figure 62. Top and cross-section SEM images of nylon-sputtered thin films deposited at A) 0 ° and B) 80° deposition angle on bare Si.

The additional information about the morphological changes was obtained by the AFM measurements (Figure 63). The surface structure of the films becomes more developed with the increase of the deposition angle.

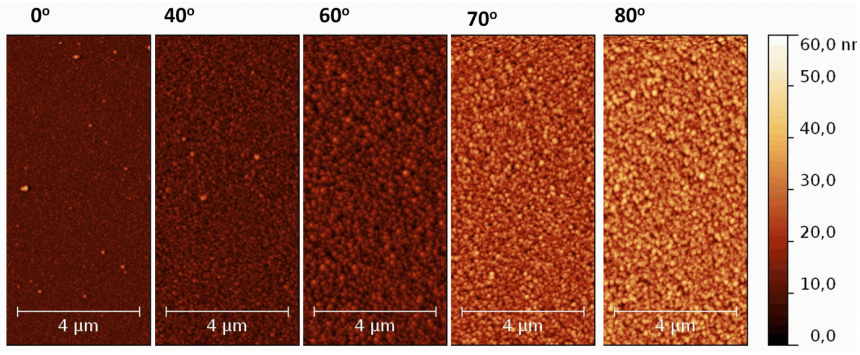

Figure 63. AFM scans of nylon-sputtered thin films deposited at different deposition angles

The root-mean-square (RMS) roughness *w* and the correlation length ξ were calculated from the AFM images for each of the samples. The analysis of Figure 64,

where all the results are summarized, shows that *w* increases from about 2 to 6 nm with the deposition angle increasing from 0 to 80 degree.

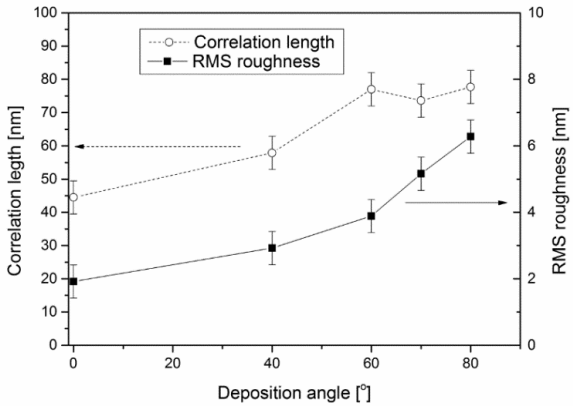

Figure 64. The correlation length and the RMS roughness in dependence on the deposition angle.

In addition to the vertical changes of the surface topography, morphological alterations in the lateral direction were also observed. It can be seen in Figure 64 that the increase of the deposition angle from 0 to 80 degree resulted in the corresponding increase of the correlation length from 45 nm to 80 nm. This result correlates with previous SEM observations, where the formation of bigger bumps on the surface of nylon-sputtered thin films deposited at highest deposition angle was observed.

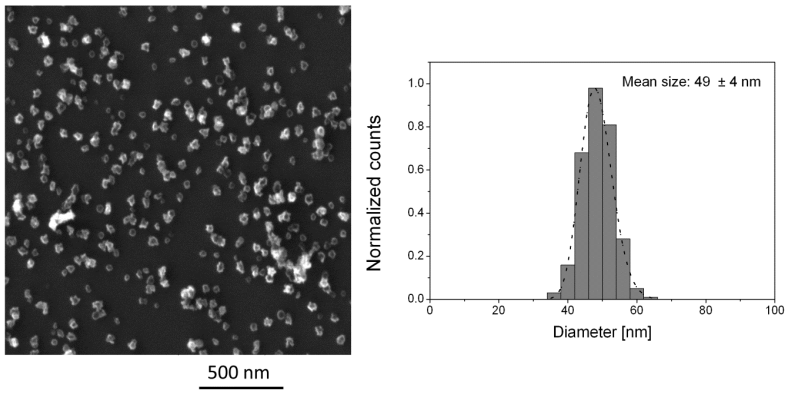

Figure 65. The top view SEM image (left picture) and the size distribution (right picture) of the nylon-sputtered NPs deposited by GAS with the semi-hollow magnetron.

In the second step, the GLAD structures were fabricated using the sub-monolayer of nylon-sputtered NPs. As was revealed by SEM analysis (Figure 65), the NP layer consisted of irregularly shaped nanoparticles with the mean size of 49±4 nm.

The subsequent overcoating of the NPs with the sputtered nylon films resulted in the formation of nanostructured coatings depicted in Figure 66. The SEM images of such coatings prepared at 0° deposition angle revealed significant texturing in comparison with structure of the films deposited on bare substrate. The presence of the NPs led to the formation of the randomly distributed tapered bumps on the surface, the mean diameter of which is much larger than the diameter of the original NPs. Despite the coatings are compact and no separated columns are detected, the distinct columnar pattern can be seen. The increase of the deposition angle makes the columnar structure more distinguishable. The conically-shaped columns are inclined with respect to the direction of the incoming material. The clear imprint of the deposition angle can be also observed on the top view images where the surface 'humps' are elongated to some extent. It can be seen in Figure 66 A) and B) that the space between the surface humps is homogeneously filled with the plasma polymer. In contrast, the coatings deposited at 80° are composed of well separated columns

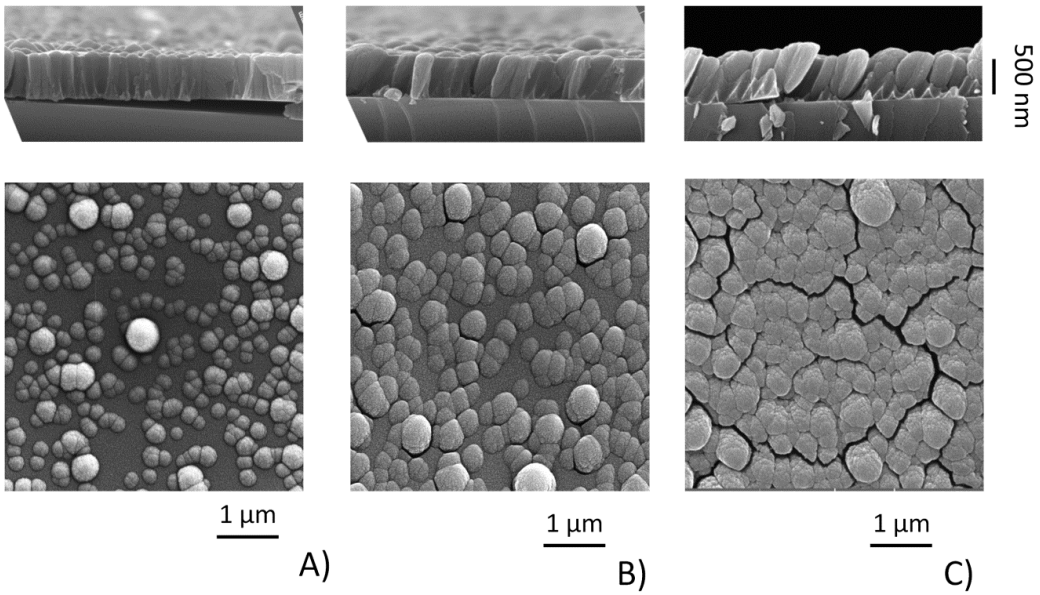

Figure 66. GLAD structures deposited on the nanoparticle pre-coated substrate at different deposition angles: A) 0°; B) 40°; C) 80°

The results of the AFM analysis of these samples are illustrated in Figure 67. In comparison with the nylon-sputtered films on bare Si, the structural changes are more prominent and cover the height scale of hundreds of nanometers . At the same time, the surface topography does not show significant variations with increasing deposition angle.

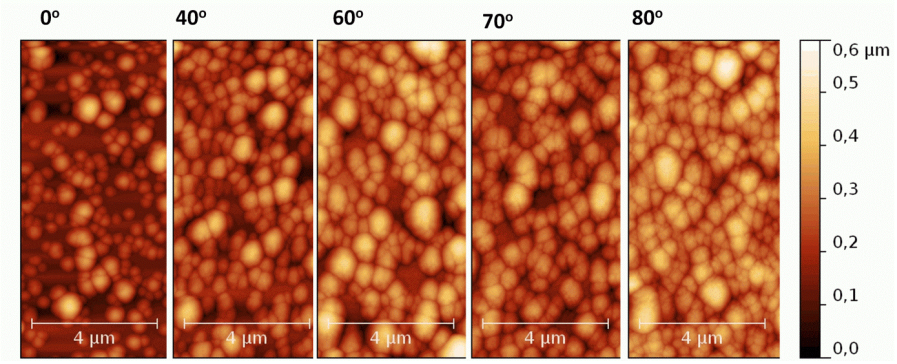

Figure 67. The AFM scans of nylon-sputtered films deposited over the NP layer at corresponding deposition angle

The RMS roughness just slightly increases from 60±6 nm (0°) to 77±4 nm (80°) (see Figure 68). In contrast, the noticeable dependence of the correlation length on the deposition angle is observed. The correlation length of the samples fabricated at 0° and 40° is similar and equal to 280±20 nm, while its value almost linearly increases for higher deposition angles and reaches 400 nm at 80°.

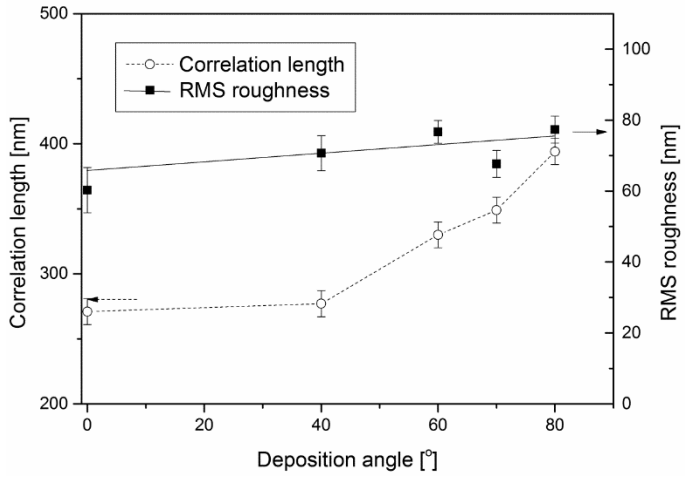

Figure 68. The correlation length and RMS roughness of the nylon-sputtered coatings deposited over the NP layer at corresponding deposition angle

The chemical composition of the GLAD coatings was studied by XPS. The coatings deposited on bare Si substrate have the same elemental composition as the ones prepared over pre-seeded NPs. It was found that 54% of total atomic content belongs to carbon and the rest 32% and 14% refer to nitrogen and oxygen, correspondingly. The invariability of the chemical composition was also confirmed by the high resolution analysis of the C1s spectra. The C1s spectra of the films prepared with and without particles at deposition angle of 80° were compared. The carbon spectrum as shown in Figure 69, was deconvoluted with four components. The C1 component corresponds to the C-C/C-H bonds positioned at 285.0 eV while the other three peaks are most probably originated from different C-O/C-N compounds. Since no differences in the chemical composition were observed it can be concluded that the growth process of the nylon-sputtered GLAD structures is influenced only by the presence of particles and by the deposition angle.

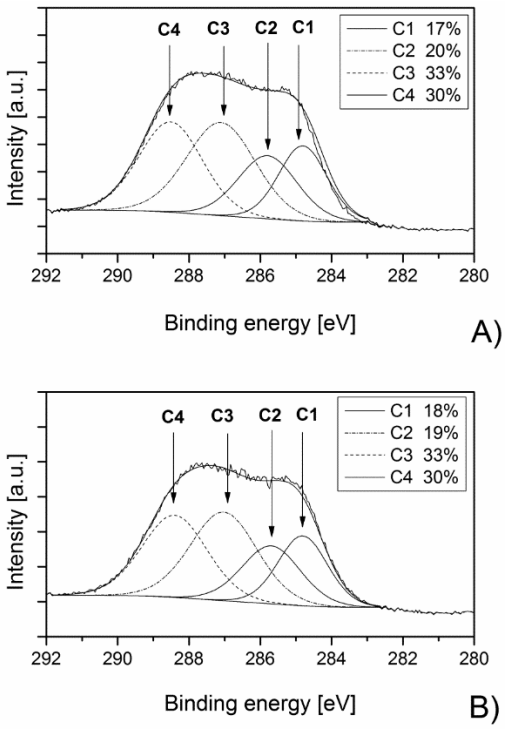

Figure 69. The comparison of the high resolution C 1s XPS spectra of nylon-sputtered thin films deposited on A) bare silicon wafer and on B) the substrate pre-seeded with small nanoparticles. For both cases the deposition angle was 80°.

3.5. Atmospheric pressure plasma jet for the deposition of nitrogen rich plasma polymer thin films

The results presented in this part of my thesis were obtained during my short term scientific mission (18.07-22.08.16) at University College Dublin, where I worked on the deposition of amino rich plasma polymer thin films by atmospheric pressure plasma jet. The scheme of the utilized experimental setup is described in detail in the experimental section 2.2.2. The liquid monomer diaminocyclohexane ($C_6H_{14}N_2$) (DACH) was used as a precursor. This type of the monomer was chosen because it has the lowest toxicity as compared to other amino-containing monomers. Silicon wafers were used as substrates. The deposition protocol consisted of two pretreatment scans with the plasma jet, nine scans of the deposition and two scans of the post treatment. The speed with which the deposition tube traversed above the substrate was fixed at 25 mm/s. The size of monomer droplets entering the discharge is a critical parameter which influences the quality of deposited films. The monomer droplet size entering the discharge was measured using a HELOS laser diffraction particle size analyzer. Droplet size distribution data indicated that the mean size of DACH droplets ranged from 5 to 22 μm. The size of the monomer droplets is large in comparison to other monomers such as organo-silicon based precursors. This is due to the relatively high surface tension and viscosity of the monomer. As can be seen in Figure 70, the volume mean diameter of the monomer droplets is dependent on the pressure of carrier gases propelling the droplets and on the flow rate of DACH monomer.

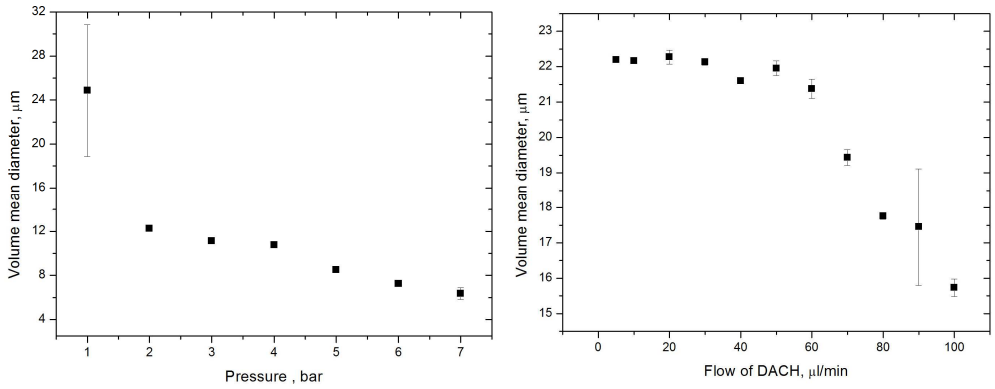

Figure 70. Dependence of volume mean diameter of monomer droplets on the pressure of carrier gases (left picture) and on the flow of DACH (right picture).

The diameter of droplets decreases from approximately 25 to 5 μm with the increasing pressure. On the other hand, the increase in the monomer flow rate from 10 to 100 μl/min decreases the droplet size from 10 to 2 μm. This is due to more efficient transfer of energy from the carrier gas to the liquid, which results in a larger percentage of smaller droplets in the distribution.

The first depositions were performed onto the substrates at room temperature with low flow of the monomer and the maximum discharge power of 8 W. As can be seen in Figure 71, the coatings are very rough and inhomogeneous. Immersion in water showed that the films are also very soluble. Obviously the discharge power is not enough to activate the sufficient number of the precursor molecules in the droplets, which leads to the lower extent of polymerization. The areas of high surface roughness indicate that large droplets reach the surface of the wafer. The smoother areas indicate that smaller droplets which reach the surface undergo some degree of polymerization. However, the energy per unit monomer was not high enough to sufficiently polymerize the monomer in order to achieve a stable performance in water. In order to promote the polymerization, the temperature of the substrates was increased up to 100° C. By heating the substrate it was possible to enhance cross-linking in the films. The deposited films were very smooth and did not show any traces of micro-droplets on the surface. Therefore, all further experiments were performed with the heated substrates.

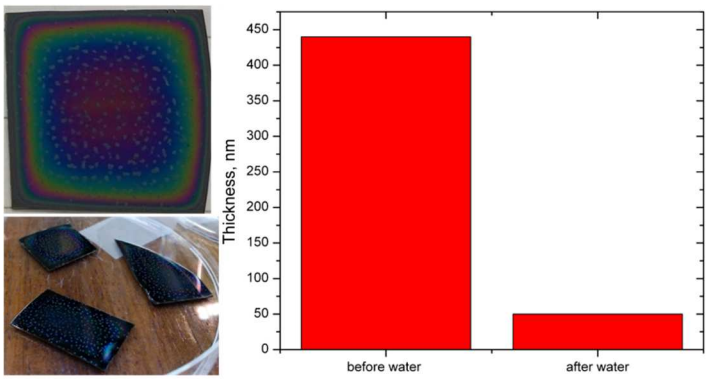

Figure 71. The photos (left) and the water stability results (right) of DACH plasma polymer films deposited onto unheated substrates (flow of DACH – 10 μl/min; discharge power – 8W).

In the next experiments, the influence of different discharge power on the properties of the deposited coatings was investigated. It is clearly seen in Figure 72

(left) that the increase of the discharge power from 4 to 8 W led to the increase of the thickness from 22 up to 67 nm. The significant changes were also observed for refractive index of the films (Figure 72 right).

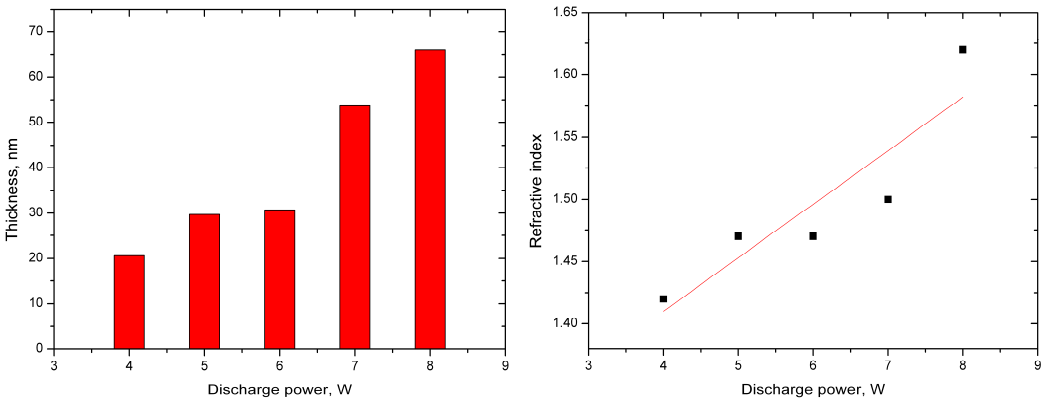

Figure 72. The dependence of thickness (left) and refractive index (right) of DACH plasma polymers on the discharge power.

The influence of the discharge power on the water stability of the coatings was also studied. As evidenced in Figure 73, the coatings deposited at higher discharge power were more stable in comparison with those fabricated at low power. These results correlate with the changes in the refractive index which was determined by ellipsometry.

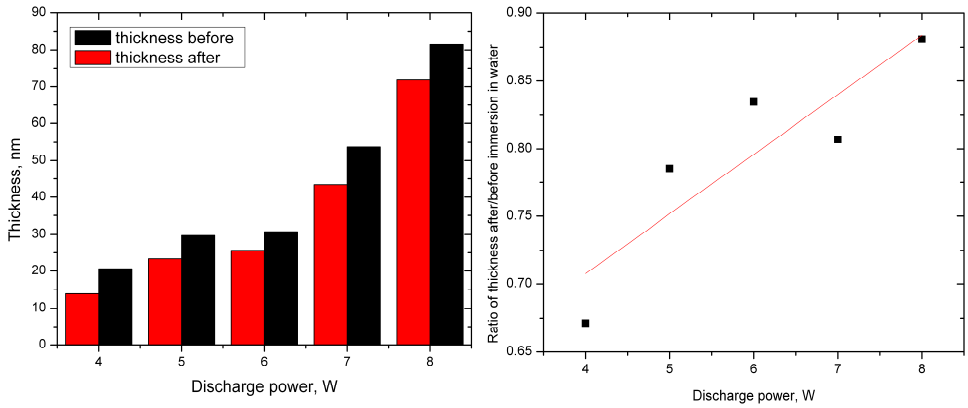

Figure 73. Thickness of DACH plasma polymer films prepared at different discharge power before and after immersion in water (left). Relative decrease of thickness upon immersion in water as the function of the discharge power (right).

It is well known that the value of the refractive index depends strongly on density and roughness of coatings. It will be shown further that, in this case, the roughness did not change significantly with the power. Hence, such variation of refractive index can be caused by the changes in films density. The higher power results in the formation of the increased number of radicals which participate in cross-linking reactions and it leads to densification of the films. The film with higher refractive index was the most stable in water.

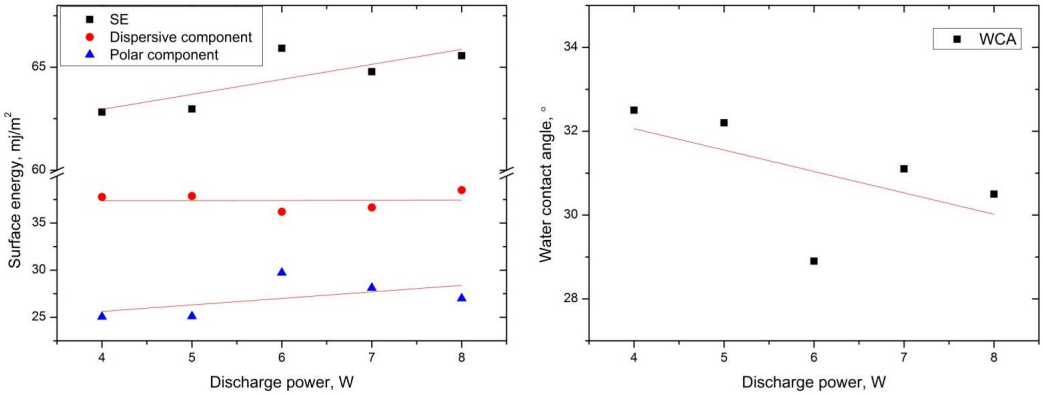

Figure 74. The dependence of the surface energy (left) and WCA (right) on the discharge power

The increase of the discharge power has also an effect on the chemical composition of the DACH plasma polymers. It can be seen in the Figure 74 that the surface energy (SE) of the coatings increased with the power, which led to a decrease of water contact angle. The SE changed due to an increase in polar component, while the values of the dispersive component did not change much.

Discharge power, W	O %	N %	C %		Flow of DACH,	O %	N %	C %
4	14	19	67		10	13	23	64
5	14	20	66		20	13	23	64
6	14	20	66		50	14	21	65
7	15	21	64		70	14	20	66
8	14	23	64		100	13	20	67

Table 4: XPS elemental composition of films deposited at different discharge power (left) or at different flow of the precursor (right)**.**

The water contact angle and surface energy results are consistent with the chemical changes observed by XPS (Table 4). The increase of the discharge power leads to the increase of nitrogen and to the decrease of the carbon content. The amount of oxygen in films is almost constant.

The deconvolution of the spectrum revealed three peak components which were assigned 1) to the C-C/C-H bonds; 2) to various CN as well as C-O bonds; 3) to the N-C=O and C=O bonds. The graphical representation of the fitted spectra is shown in Figure 75. The signal from the hydrocarbon species decreases with the increasing discharge power. At the same time, the concentration of the CN bonds increases with the power. Chemical derivatization was performed to distinguish the primary amine groups.

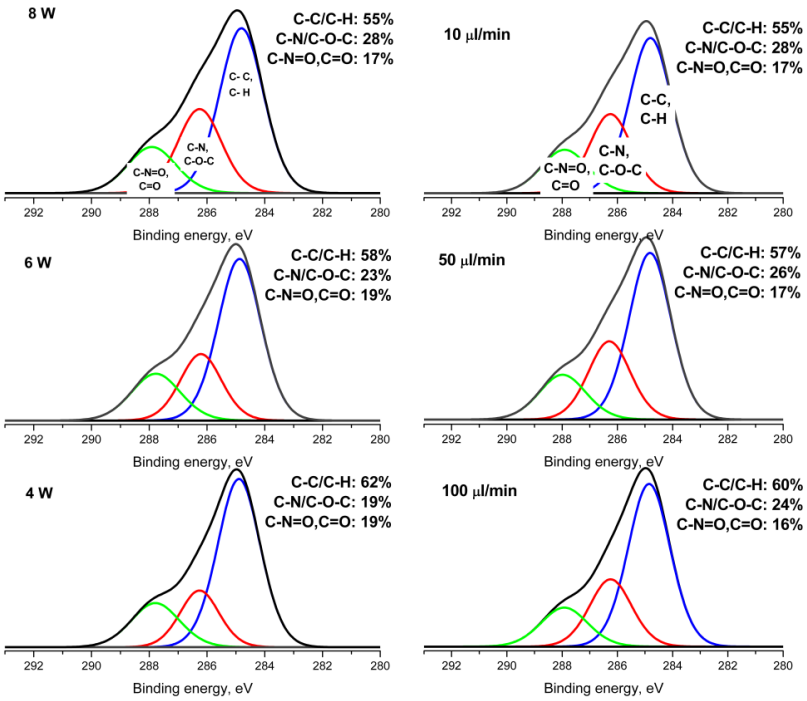

Figure 75. The C1s XPS spectra of plasma polymer film deposited at different power (left) and different flow (right)

The results allow to conclude that the amine efficiency (the number of primary amines per 100 carbon atoms, NH_2/C) and amine selectivity (the number of primary amines per 100 nitrogen atoms, NH_2/N) lie in the range of 1.1 - 2.3% and 2.8 - 6.5 %, respectively.

The morphology of the films was studied by optical profilometry. The results show that films prepared at different discharge power have similar structure. The

mean value of roughness is equal to 3.9 nm. An example of the surface map of the sample deposited at discharge power of 5 W is shown in Figure 76.

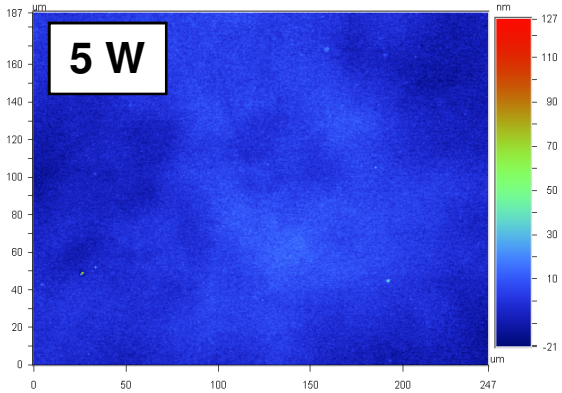

Figure 76. The surface data of the sample deposited at discharge power 5 W (RMS - 3.9 nm)

In the next experiments, the influence of different flow on the properties of the prepared coatings was investigated. In contrast to the results obtained for the samples deposited at different power, the increase of the flow has little effect on the deposition rate and the value of refractive index (Figure 77).

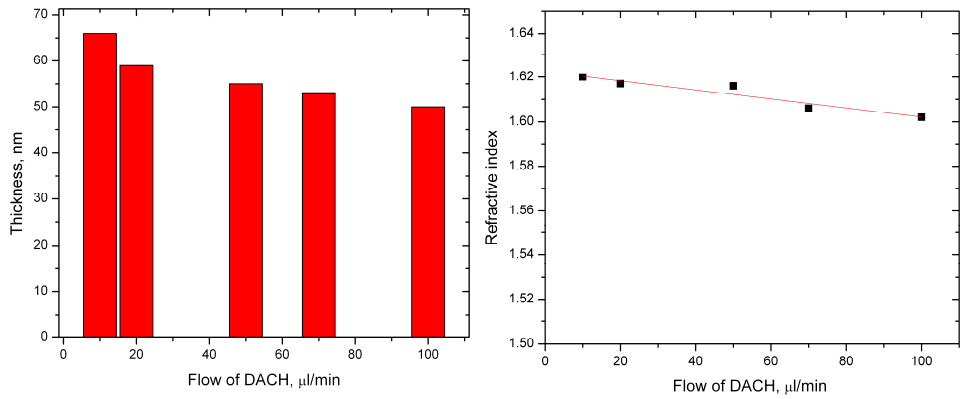

Figure 77. The dependence of thickness (left) and refractive index (right) on the flow of the precursor.

The results of WCA and SE measurements, which are shown in Figure 78, showed that the increase of the flow induces the decrease of the surface energy and increase of the water contact angle. The WCA and SE results are consistent with the changes in the XPS elemental composition (Table 4 (right part)). The sample deposited at maximum flow shows higher concentration of carbon and lowest

concentration of nitrogen in comparison with the samples prepared at low flow rates. The atomic concentration of oxygen in the films is almost similar. The analysis of the C1s high resolution spectra show that the concentration of the hydrocarbon species increases from 55 to 60 %, while the amount of the CN bonds decreases from 28 to 24 % with increasing flow of the precursor (Figure 75(right)). The amine efficiency and amine selectivity is in the range of 0.9 – 1.4 % and 2.3 - 4 %, respectively.

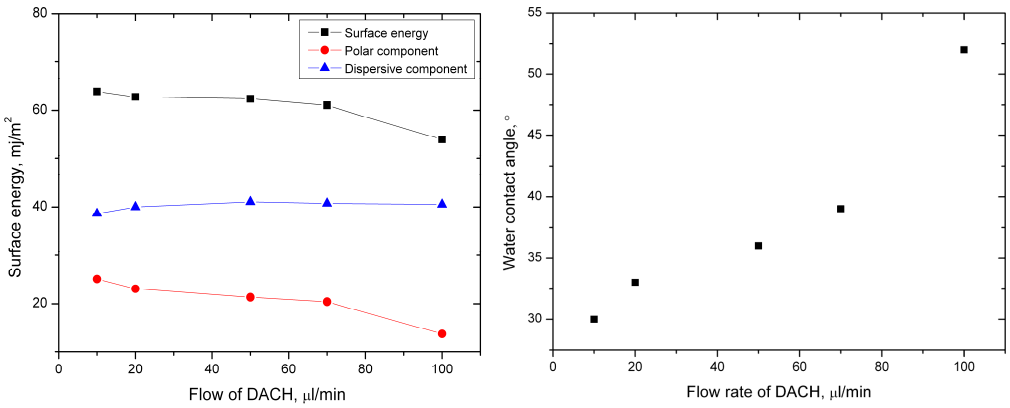

Figure 78. The dependence of the surface energy (left) and WCA (right) on the flow of the precursor.

Similar to the discharge power, the change of the flow has no significant effect on the structure of the films. The mean value of roughness is 5.7 nm.

In order to estimate the effect of aging of the coatings, the WCA and XPS studies were made on fresh samples and the ones stored at open atmosphere for 7 days. It is seen in Figure 79 that WCA increased by 12 degrees after 7-day storage time.

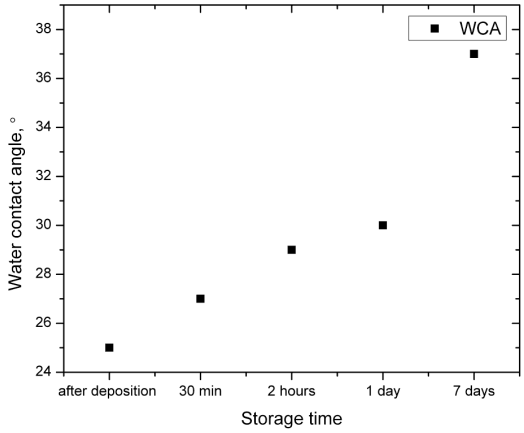

Figure 79. The dependence of WCA on the storage time at open atmosphere

The results are consistent with the changes observed in the XPS spectra. The sample which was kept at open atmosphere for 7 days contained more oxygen and carbon, and less nitrogen. The O/C ratio increased from 0.18 to 0.22. At the same time, the N/C ratio decreased from 0.35 to 0.25. It has to be noted that amino-containing plasma polymer thin films deposited at low pressure demonstrated comparable changes in chemical composition after 1 hour of storage in air.

The next step of this investigation was to test the possibility of immobilization of biomolecules on the deposited thin films. The analysis of the protein adsorption was carried out using ellipsometry. The samples were sealed inside a liquid flow cell which was positioned at the ellipsometry stage. The changes of the thickness of the protein layer were monitored at the fixed incident angle of 70°. Fibrinogen solution (with the concentration of 1 μg/ml) was introduced into the cell after 10 min of the stabilization period. It can be seen in Figure 80 that the films prepared at different experimental conditions show similar level of the protein adsorption. The maximum thickness of the adsorbed protein was 12 nm, which is 4 times higher than the value obtained for uncoated silicon wafer. Probably, the small difference in chemical composition of the films prepared with different power and flow of DACH results in the insignificant effect on the level of the protein adsorption.

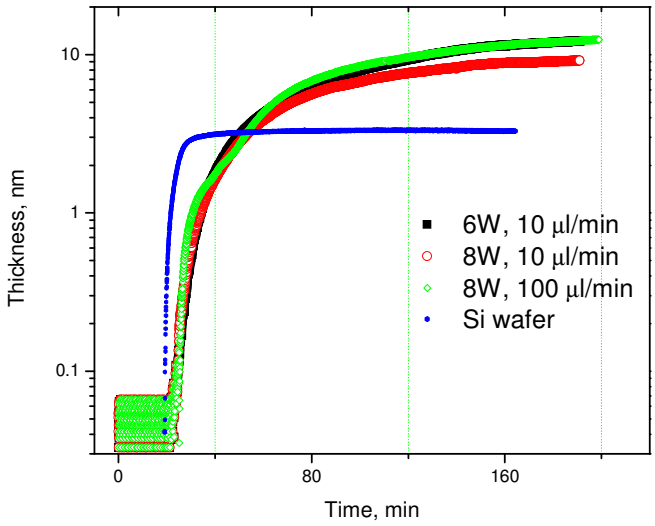

Figure 80. Ellipsometry analysis of fibrinogen adsorption on the uncoated silicon wafer substrate and amino rich plasma polymer thin films

CONCLUSIONS

- It has been shown that Ti/TiO_x NP coatings of different chemical composition can be deposited by gas aggregation cluster source.
- Ti/hydrocarbon nanostructured coatings were prepared using GAS and plasma polymerization of *n*-hexane. Two stages of the film growth have been identified. The early stage involves the penetration of active species into the pores among the Ti NPs resulting in filling of the voids with plasma polymer. The final stage occurs when the pores become filled and is characterized by smoothening of the surface.
- Atmospheric pressure DBD has been utilized for deposition of nitrogen-doped TiO_2 NPs and their composites with plasma polymer. The dependence of chemical composition and morphology of the coatings on the working gas mixture, flow of carrier gas and discharge power has been revealed.
- *Ex-situ* and *in-situ* diagnostics of the production process of AlO_x NPs by GAS have shown direct correlation between the main discharge parameters, the deposition rate and the properties of the NPs.
- SiO_x(CH) NPs with tunable properties have been deposited using GAS from mixtures of HMDSO with Ar and O_2. It has been shown in the former case that the size of the NPs can be changed by changing the aggregation length and the power delivered to the discharge. In the latter case the addition of oxygen into the working gas mixture changes the chemical composition of the NPs from SiO_x(CH) plasma polymer to inorganic SiO_x.
- Surfaces with double- and triple-scale roughness have been prepared using combinations of SiO_x(CH) NPs. Biomimetic application of these nanostructured films has been demonstrated.
- Nylon-sputtered NPs have been used as pre-seeds for GLAD of plasma polymer nanocolumnar structures.
- Atmospheric pressure plasma jet has been demonstrated as a feasible tool for deposition of nitrogen rich plasma polymer films.

BIBLIOGRAPHY

[1] W. D. Harkins, J. M. Jackson, *The Journal of Chemical Physics* 1933, *1*, 37.

[2] R. Conrad, *Transactions of the Faraday Society* 1934, *30*, 215.

[3] J. Austin, *Journal of the American Chemical Society* 1930, *52*, 3026.

[4] W. D. Harkins, *Transactions of the Faraday Society* 1934, *30*, 221.

[5] E. G. Linder, A. P. Davis, *The Journal of Physical Chemistry* 1930, *35*, 3649.

[6] M. P. v. Wilde, *Berichte der deutschen chemischen Gesellschaft* 1874, *7*, 352.

[7] H. König, G. Helwig, *Zeitschrift fr Physik* 1951, *129*, 491.

[8] A. Brockes, H. König, *Zeitschrift für Physik* 1958, *152*, 75.

[9] J. Goodman, *Journal of Polymer Science* 1960, *44*, 551.

[10] A. Bradley, J. P. Hammes, *Journal of The Electrochemical Society* 1963, *110*, 15.

[11] H. Biederman, *Plasma Polymer Films*; Imperial College Press: London, 2004.

[12] H. Biederman, Y. Osada, *Plasma Polymerization Processes*; ELSEVIER, Amsterdam, 1992.

[13] T. Williams, M. W. Hayes, *Nature* 1966, *209*, 769.

[14] A. R. Denaro, P. A. Owens, A. Crawshaw, *European Polymer Journal* 1969, *5*, 471.

[15] H. Carchano, *The Journal of Chemical Physics* 1974, *61*, 3634.

[16] A. R. Westwood, *European Polymer Journal* 1971, *7*, 363.

[17] H. U. Poll, M. Arzt, K. H. Wickleder, *European Polymer Journal* 1976, *12*, 505.

[18] H. Yasuda, T. Hsu, *Surface Science* 1978, *76*, 232.

[19] J. M. Tibbitt, R. Jensen, A. T. Bell, M. Shen, *Macromolecules* 1977, *10*, 647.

[20] M. Gazicki, H. Yasuda, *Plasma Chemistry and Plasma Processing* 1983, *3*, 279.

[21] A. Choukourov, Y. Pihosh, V. Stelmashuk, H. Biederman, D. Slavínská, M. Kormunda, L. Zajíčková, *Surface and Coatings Technology* 2002, *151–152*, 214.

[22] Y. Pihosh, H. Biederman, D. Slavinska, J. Kousal, A. Choukourov, M. Trchova, A. Mackova, A. Boldyreva, *Vacuum* 2006, *81*, 32.

[23] Y. Pihosh, H. Biederman, D. Slavinska, J. Kousal, A. Choukourov, M.

Trchova, A. Mackova, A. Boldyryeva, *Vacuum* 2006, *81*, 38.

[24] R. Harrop, P. J. Harrop, *Thin Solid Films* 1969, *3*, 109.

[25] H. Biederman, P. Bilkova, J. Jezek, P. Hlidek, D. Slavinska, *Journal of Non-Crystalline Solids* 1997, *218*, 44.

[26] H. Biederman, *Thin Solid Films* 1978, *55*, 11.

[27] L. Holland, H. Biederman, S. M. Ojha, *Thin Solid Films* 1976, *35*, 19.

[28] H. Biederman, S. M. Ojha, L. Holland, *Thin Solid Films* 1977, *41*, 329.

[29] J. M. Tibbitt, M. Shen, A. T. Bell, *Thin Solid Films* 1975, *29*, 85.

[30] T. Robertson, D. T. Morrison, *Thin Solid Films* 1975, *27*, 19.

[31] I. H. Pratt, T. C. Lausman, *Thin Solid Films* 1972, *10*, 151.

[32] D. T. Morrison, T. Robertson, *Thin Solid Films* 1973, *15*, 87.

[33] H. Biederman, M. Zeuner, J. Zalman, P. Bílková, D. Slavínská, V. Stelmasuk, A. Boldyreva, *Thin Solid Films* 2001, *392*, 208.

[34] I. Kholodkov, H. Biederman, D. Slavınská, A. Choukourov, M. Trchova, *Vacuum* 2003, *70*, 505.

[35] V. Stelmashuk, H. Biederman, D. Slavínská, M. Trchová, P. Hlidek, *Vacuum* 2004, *75*, 207.

[36] J. Kousal, J. Hanuš, a. Choukourov, P. Hlídek, H. Biederman, D. Slavínská, J. Zemek, *Surface and Coatings Technology* 2005, *200*, 472.

[37] A. Choukourov, J. Hanuš, J. Kousal, A. Grinevich, Y. Pihosh, D. Slavínská, H. Biederman, *Vacuum* 2006, *81*, 517.

[38] A. Choukourov, A. Grinevich, J. Hanuš, J. Kousal, D. Slavínská, H. Biederman, A. Bowers, L. Hanley, *Thin Solid Films* 2006, *502*, 40.

[39] O. Kylián, J. Hanuš, A. Choukourov, J. Kousal, D. Slavínská, H. Biederman, *Journal of Physics D: Applied Physics* 2009, *42*, 142001.

[40] O. Kylián, J. Kousal, A. Artemenko, A. Choukourov, M. Petr, O. Polonskyi, D. Slavinska, H. Biederman, *Surface and Coatings Technology* 2011, *205*, S558.

[41] D. Merche, N. Vandencasteele, F. Reniers, *Thin Solid Films* 2012, *520*, 4219.

[42] U. Kogelschatz, *Plasma Chemistry and Plasma Processing* 2003, *23*, 1.

[43] U. Kogelschatz, B. Eliasson, W. Egli, *Journal De Physique IV* 1997, *7*.

[44] F. Massines, N. Gherardi, A. Fornelli, S. Martin, *Surface and Coatings Technology* 2005, *200*, 1855.

[45] R. Morent, N. De Geyter, S. Van Vlierberghe, P. Dubruel, C. Leys, L.

Gengembre, E. Schacht, E. Payen, *Progress in Organic Coatings* 2009, *64*, 304.

[46] X.-L. Zhang, L.-H. Nie, Y. Xu, C. Shi, X.-F. Yang, A.-M. Zhu, *Journal of Physics D: Applied Physics* 2007, *40*, 1763.

[47] L.-H. Nie, C. Shi, Y. Xu, Q.-H. Wu, A.-M. Zhu, *Plasma Processes and Polymers* 2007, *4*, 574.

[48] O. Goossens, E. Dekempeneer, D. Vangeneugden, R. Van de Leest, C. Leys, *Surface and Coatings Technology* 2001, *142–144*, 474.

[49] N. Jiang, S. F. Qian, L. Wang, H. X. Zhang, *Thin Solid Films* 2001, *390*, 119.

[50] D. Merche, C. Poleunis, P. Bertrand, M. Sferrazza, F. Reniers, *IEEE Transactions on Plasma Science* 2009, *37*, 951.

[51] N. De Geyter, R. Morent, S. Van Vlierberghe, P. Dubruel, C. Leys, L. Gengembre, E. Schacht, E. Payen, *Progress in Organic Coatings* 2009, *64*, 230.

[52] I. Topala, N. Dumitrascu, G. Popa, *Nuclear Instruments and Methods in Physics Research, Section B: Beam Interactions with Materials and Atoms* 2009, *267*, 442.

[53] I. Vinogradov, A. Dinkelmann, A. Lunk, *Surface and Coatings Technology* 2003, *174–175*, 509.

[54] F. Fanelli, F. Fracassi, R. d'Agostino, *Plasma Processes and Polymers* 2007, *4*, 430.

[55] A. Schutze, J. Y. Jeong, S. E. Babayan, J. Park, G. S. Selwyn, R. F. Hicks, *Plasma Science, IEEE Transactions on* 1998, *26*, 1685.

[56] V. Raballand, J. Benedikt, S. Hoffmann, M. Zimmermann, a. von Keudell, *Journal of Applied Physics* 2009, *105*, 83304.

[57] S. E. Babayan, J. Y. Jeong, V. J. Tu, J. Park, G. S. Selwyn, R. F. Hicks, *Plasma Sources Science and Technology* 1998, *7*, 286.

[58] F. Truica-Marasescu, M. R. Wertheimer, *Plasma Processes and Polymers* 2008, *5*, 44.

[59] A. Vogelsang, A. Ohl, R. Foest, K. Schröder, K. D. Weltmann, *Plasma Processes and Polymers* 2011, *8*, 77.

[60] K. Inomata, A. Nobuyuki, Koinuma, Hideomi, *Jpn. J. Appl. Phys.* 1994, *33*, 197.

[61] D. Han, S. Y. Moon, *Plasma Processes and Polymers* 2015, *12*, 172.

[62] Z. Yang, T. Kikuchi, Y. Hatou, T. Kobayashi, H. Shirai, *Japanese Journal of Applied Physics* 2005, *44*, 4122.

[63] C. P. Stallard, M. M. Iqbal, M. M. Turner, D. P. Dowling, *Plasma Processes and Polymers* 2013, n/a.

[64] C. P. Stallard, P. Solar, H. Biederman, D. P. Dowling, *Plasma Processes and Polymers* 2015, n/a.

[65] B. D. Plouffe, S. K. Murthy, L. H. Lewis, *Reports on progress in physics. Physical Society (Great Britain)* 2014, *78*, 16601.

[66] S. S. Lee, W. Song, M. Cho, H. L. Puppala, P. Nguyen, H. Zhu, L. Segatori, V. L. Colvin, *ACS Nano* 2013, *7*, 9693.

[67] O. V Salata, *Journal of Nanobiotechnology* 2004, *6*, 1.

[68] K. Wegner, P. Piseri, H. V. Tafreshi, P. Milani, *Journal of Physics D: Applied Physics* 2006, *39*, R439.

[69] C. Boyer, M. R. Whittaker, V. Bulmus, J. Liu, T. P. Davis, *NPG Asia Materials* 2010, *2*, 23.

[70] X. Fan, W. Zheng, D. J. Singh, *Light: Science & Applications* 2014, *3*, e179.

[71] R. Taylor, S. Coulombe, T. Otanicar, P. Phelan, A. Gunawan, W. Lv, G. Rosengarten, R. Prasher, H. Tyagi, *Journal of Applied Physics* 2013, *113*.

[72] C. Binns, *Surface Science Reports* 2001, *44*, 1.

[73] K. Sattler, J. Muhlbach, E. Recknagel, *Physical Review Letters* 1980, *45*, 821.

[74] B. Briehl, H. M. Urbassek, *Journal of Vacuum Science & Technology A: Vacuum, Surfaces, and Films* 1999, *17*, 256.

[75] H. Haberland, *Journal of Vacuum Science & Technology A: Vacuum, Surfaces, and Films* 1994, *12*, 2925.

[76] H. Haberland, M. Karrais, M. Mall, *Z. Phys. D - Atoms, Molecules and Clusters* 1991, *20*, 413.

[77] H. Haberland, M. Karrais, M. Mall, Y. Thurner, *Journal of Vacuum Science & Technology A* 1992, *10*, 3266.

[78] B. V. Tkachuk, N. Y. Marusii, E. P. Laurs, *Vysokomol. Soed.* 1973, *A15*, 2046.

[79] E. Kny, *Journal of Vacuum Science and Technology* 1979, *16*, 359.

[80] C. Oehr, H. Suhr, *Thin Solid Films* 1987, *155*, 65.

[81] N. Morosoff, D. L. Patel, A. R. White, A. L. Crumbliss, P. S. Lugg, D. B. Brown, *Thin Solid Films* 1984, *117*, 33.

[82] S. D. Phadke, *Thin Solid Films* 1978, *48*, 319.

[83] Y. Osada, K. Yamada, I. Yoshizawa, *Thin Solid Films* 1987, *151*, 71.

[84] M. White, N. Boonthanoom, Composite metal polymer films 1977, 1.

[85] N. Boonthanom, M. White, *Thin Solid Films* 1974, *24*, 295.

[86] E. Kay, A. Dilks, U. Hetzler, *J. Macromol. Sci. Part A pure Appl. Chem.* 1978, *A12*, 1393.

[87] H. Biederman, *Vacuum* 1984, *34*, 405.

[88] H. Biederman, L. Holland, *Nuclear Instruments and Methods in Physics Research* 1983, *212*, 497.

[89] L. Martinů, *Thin Solid Films* 1986, *140*, 307.

[90] E. Kay, *Zeitschrift für Physikr Physik D Atoms, Molecules and Clusters* 1986, *3*, 251.

[91] H. Biederman, *Surface and Coatings Technology* 2011, *205*, S10.

[92] R. A. Roy, R. Messier, S. V. Krishnaswamy, *Thin Solid Films* 1983, *109*, 27.

[93] R. Lamber, S. Wetjen, N. I. Jaeger, *Physical Review B* 1995, *51*, 10968.

[94] R. Lamber, S. Wetjen, G. Schulz-Ekloff, A. Baalmann, *The Journal of Physical Chemistry* 1995, *99*, 13834.

[95] D. Salz, R. Lamber, M. Wark, A. Baalmann, N. Jaeger, *Physical Chemistry Chemical Physics* 1999, *1*, 4447.

[96] O. Kylián, O. Polonskyi, J. Kratochvíl, A. Artemenko, A. Choukourov, M. Drábik, P. Solař, D. Slavínská, H. Biederman, *Plasma Processes and Polymers* 2012, *9*, 180.

[97] O. Polonskyi, P. Solař, O. Kylián, M. Drábik, a. Artemenko, J. Kousal, J. Hanuš, J. Pešička, I. Matolínová, E. Kolíbalová, D. Slavínská, H. Biederman, *Thin Solid Films* 2012, *520*, 4155.

[98] P. Solař, O. Kylián, O. Polonskyi, a. Artemenko, D. Arzhakov, M. Drábik, D. Slavínská, M. Vandrovcová, L. Bačáková, H. Biederman, *Surface and Coatings Technology* 2012, *206*, 4335.

[99] A. Kuzminova, A. Shelemin, O. Kylián, M. Petr, J. Kratochvíl, P. Solař, H. Biederman, *Vacuum* 2014, *110*, 58.

[100] O. Kylián, J. Kratochvíl, J. Hanuš, O. Polonskyi, P. Solař, H. Biederman, *Thin Solid Films* 2014, *550*, 46.

[101] O. Kylián, M. Petr, A. Serov, P. Solař, O. Polonskyi, J. Hanuš, A. Choukourov, H. Biederman, *Vacuum* 2014, *100*, 57.

[102] A. Choukourov, I. Melnichuk, A. Shelemin, P. Solar, H. Biederman, 2015.

[103] A. Kundt, *Annalen der Physik und Chemie* 1886, *263*, 59.

[104] F. Kaempf, *Annalen der Physik* 1905, *321*, 308.

[105] M. Hawkeye, M. Brett, *Journal of Vacuum Science & Technology a* 2007, *25*, 1317.

[106] M. Volmer, A. Weber, *Z. Phys. Chem.* 1926, *119*, 277.

[107] H. Konig, G. Helwig, *Optik* 1950, *6*, 111.

[108] M. T. Tashuk, M. M. Hawkeye, M. J. Brett, Martin, P. M., Ed.; Elsevier: Oxford, UK, 2010; pp. 621–651.

[109] M. M. Hawkeye, M. T. Taschuk, M. J. Brett, *Glancing Angle Deposition of Thin Films*; John Wiley & Sons, Ltd: Chichester, UK, 2014.

[110] P. Solař, Preparation of nanostructured and nanocomposite thin films with plasma polymer matrix, Charles University in Prague, 2014.

[111] G. Sauerbrey, *Zeitschrift für Physik* 1959, *155*, 206.

[112] A. Choukourov, P. Solar, O. Polonskyi, J. Hanus, M. Drabik, O. Kylian, E. Pavlova, D. Slavinska, H. Biederman, *Plasma Processes and Polymers* 2010, *7*, 25.

[113] A. Shelemin, A. Choukourov, J. Kousal, D. Slavínská, H. Biederman, *Plasma Processes and Polymers* 2014, *11*, 864.

[114] R. Maurau, N. D. Boscher, S. Olivier, S. Bulou, T. Belmonte, J. Dutroncy, T. Sindzingre, P. Choquet, *Surface and Coatings Technology* 2013, *232*, 159.

[115] I. Gordeev, A. Choukourov, S. Milan, *Plasma Processes and Polymers* 2012, *9*, 782.

[116] H. Bai, C. Chen, C. Lin, W. Den, C. Chang, *Industrial & Engineering Chemistry Research* 2004, *43*, 7200.

[117] C. Chen, H. Bai, C. Chang, *The Journal of Physical Chemistry C* 2007, 15228.

[118] W.-J. Liu, Y.-L. Lai, *Surface and Coatings Technology* 2011, *206*, 959.

[119] C. Chen, H. Bai, S. Chang, C. Chang, W. Den, *Journal of Nanoparticle Research* 2006, *9*, 365.

[120] H. Yoshiki, T. Mitsui, *Surface and Coatings Technology* 2008, *202*, 5266.

[121] A. Marek, J. Valter, S. Kadlec, *Surface & Coatings Technology* 2011, *205*, 573.

[122] O. Polonskyi, O. Kylián, M. Drábik, J. Kousal, P. Solař, A. Artemenko, J. Čechvala, A. Choukourov, D. Slavínská, H. Biederman, *Journal of Materials Science* 2014, *49*, 3352.

[123] A. M. Ahadi, V. Zaporojtchenko, T. Peter, O. Polonskyi, T. Strunskus, F. Faupel, *Journal of Nanoparticle Research* 2013, *15*, 2125.

[124] D. Depla, G. Buyle, J. Haemers, R. De Gryse, *Surface and Coatings Technology* 2006, *200*, 4329.

[125] D. Depla, R. De Gryse, *Plasma Sources Science and Technology* 2001, *10*, 547.

[126] L. Sandrin, E. Sacher, *Applied Surface Science* 1998, *135*, 339.

[127] T. Tachibana, J. T. Glass, *Journal of Applied Physics* 1992, *72*, 5912.

[128] A. Serov, A. Choukourov, I. Melnichuk, A. Shelemin, A. Kuzminova, O. Kylián, J. Hanuš, J. Kousal, M. Drábik, D. Slavínská, H. Biederman, *Surface and Coatings Technology* 2014, *254*, 319.

[129] P. Solař, O. Polonskyi, a. Choukourov, a. Artemenko, J. Hanuš, H. Biederman, D. Slavínská, *Surface and Coatings Technology* 2011, *205*, S42.

[130] O. Polonskyi, O. Kylián, P. Solař, A. Artemenko, J. Kousal, D. Slavínská, A. Choukourov, H. Biederman, *Journal of Physics D: Applied Physics* 2012, *45*, 495301.

[131] P. Solař, I. Melnichuk, a. Artemenko, O. Polonskyi, O. Kylián, a. Choukourov, D. Slavínská, H. Biederman, *Vacuum* 2015, *111*, 124.

[132] R. N. Wenzel, *Journal of Industrial and Engineering Chemistry (Washington, D. C.)* 1936, *28*, 988.

[133] M. R. Alexander, R. D. Short, F. R. Jones, W. Michaeli, C. J. Blomfield, *Applied Surface Science* 1999, *137*, 179.

[134] L. Muehlhoff, M. J. Choyke, J. T. Yates Jr, *Journal of Applied Physics* 1986, *60*, 2842.

LIST OF TABLES

LIST OF ABBREVIATIONS

AFM	atomic force microscopy
DACH	diaminocyclohexane
DC	direct current
DLC	diamond-like carbon
FTIR	Fourier transform infra-red spectroscopy
G	Gauss
GAS	gas aggregation cluster source
GLAD	glancing angle deposition
HeNe	Helium-Neon
Hz	Hertz
IR	infra-red
NPs	nanoparticles
OES	optical emission spectroscopy
PTFE	Polytetrafluoroethylene
QCM	Quartz crystal microbalance
RF	radio frequency
RMS	root mean square
SEM	scanning electron microscopy
TEM	transmission electron microscopy
UHV	ultra-high vacuum
XPS	X-ray photoelectron microscopy

LIST OF PUBLICATIONS

Reviewed international journals

1. **A. Shelemin**, A. Choukourov, J. Kousal, D. Slavínská, H. Biederman, *Nitrogen-Doped TiO2 Nanoparticles and Their Composites with Plasma Polymer as Deposited by Atmospheric Pressure DBD*, Plasma Process. Polym., 11, 9, 864-877 (2014), doi: 10.1002/ppap.201300207

2. A. Serov, A. Choukourov, I. Melnichuk, **A. Shelemin**, A. Kuzminova, O. Kylián, J. Hanuš, J. Kousal, M. Drábik, D. Slavínská, H. Biederman, *Poly(tetrafluoroethylene) sputtering in a gas aggregation source for fabrication of nano-structured deposits*, Surface and Coatings Technology, 254, 319–326 (2014), doi: 10.1016/j.surfcoat.2014.06.014

3. A. Kuzminova, **A. Shelemin**, O. Kylián, M. Petr, J. Kratochvíl, P. Solař, H. Biederman, *From super-hydrophilic to super-hydrophobic surfaces using plasma polymerization combined with gas aggregation source of nanoparticles*, Vacuum, 110, 58-61 (2014), doi: 10.1016/j.vacuum.2014.08.014A.

4. A. Kuzminova, **A. Shelemin**, O. Kylian , A. Choukourov, H. Valentová, I. Krakovský, J. Nedbal, D. Slavínská, H. Biederman, *Study of the effect of atmospheric pressure air dielectric barrier discharge on nylon 6,6 foils*, Polymer Degradation and Stability, 110, 378-388 (2014), doi:10.1016/j.polymdegradstab.2014.10.001

5. A. Kuzminova, M. Vandrovcová, **A. Shelemin**, O. Kylián, A. Choukourov, J. Hanuš, L. Bačáková, D. Slavínská, H. Biederman: *Treatment of poly(ethylene terephthalate) foils by atmospheric pressure air dielectric barrier discharge and its influence on cell growth,* Applied Surface Science, 357, 689-695 (2015), doi:10.1016/j.apsusc.2015.09.082

6. I. Melnichuk , A. Choukourov, M. Bilek, A. Weiss ,M. Vandrovcová, L. Bačáková , J. Hanuš, J. Kousal , **A. Shelemin**, P. Solař, D. Slavínská, H.

Biederman, *Direct covalent coupling of proteins to nanostructured plasma polymers: a route to tunable cell adhesion,* 351, 537–545 (2015), doi:10.1016/j.apsusc.2015.05.162

7. A. Choukourov, I. Melnichuk, **A. Shelemin**, P. Solar, J. Hanus, D. Slavinska, H. Biederman, *Plasma polymerization on mesoporous surfaces: n-hexane on titanium nano-particles*, J. Phys. Chem. C, 119, 52, 28906-28916 (2015), doi**:** 10.1021/acs.jpcc.5b08604

8. A. Kuzminova, J. Beranova, O. Polonskyi, **A. Shelemin**, O. Kylian, A. Choukourov, D. Slavinska, H. Biederman, *Antibacterial nanocomposite coatings produced by means of gas aggregation source of silver nanoparticles*, Surface and Coatings Technology, 294, 225–230 (2016), doi: 10.1016/j.surfcoat.2016.03.097

9. **A. Shelemin**, O. Kylián, J. Hanus, A. Choukourov, I. Melnichuk, A. Serov, D. Slavínská and H. Biederman, *Preparation of metal oxide nanoparticles by gas aggregation cluster source*, Vacuum, 120, 162-169 (2015), doi: 10.1016/j.vacuum.2015.07.008

10. **A. Shelemin**, D. Nikitin, A. Choukourov, O. Kylián, J. Kousal, I. Khalakhan, I. Melnichuk, D Slavínská, H. Biederman, *Preparation of biomimetic nano-structured films with multi-scale roughness*, Journal of Physics D Applied Physics, 49, 254001-254011 (2016), doi:10.1088/0022-3727/49/25/254001

11. D. Nikitin, A. Choukourov, V. Titov, L. Kuzmicheva, I. Lipatova, E. Mezina, V. Aleksandriiskii, **A. Shelemin**, I. Khalakhan, D. Slavinska, H. Biederman, *In situ coupling of chitosan onto polypropylene foils by an Atmospheric Pressure Air Glow Discharge with a liquid cathode,* Carbohydrate Polymers, 154, 30-9 (2016), doi: 10.1016/j.carbpol.2016.08.023

12. O. Kylian, **A. Shelemin**, P. Solar, A. Choukourov, J. Hanus, M. Vaidulych, A. Kuzminova, H. Biederman, *Plasma polymers: From thin films to nanocolumnar coatings*, Thin Solid Films, (2016), doi: 10.1016/j.tsf.2016.08.054

13. J. Kousal, **A. Shelemin**, O. Kylian, D. Slavinska, H. Biederman, *In-situ monitoring of etching of bovine serum albumin using low-temperature atmospheric plasma jet*, Applied Surface Science, 392, 1049–1054 (2017), doi:10.1016/j.apsusc.2016.09.135

14. A. Choukourov, O. Kylián, M. Petr, M. Vaidulych, D. Nikitin, J. Hanuš, A. Artemenko, **A. Shelemin**, I. Gordeev, Z. Kolská, P. Solař, I. Khalakhan, A. Ryabov, J. Májek, D. Slavínská, H. Biederman, *RMS roughness-independent tuning of surface wettability by tailoring silver nanoparticles with a fluorocarbon plasma polymer*, Nanoscale, 9, 2616-2625 (2017) doi:10.1039/C6NR08428A

Conference proceedings and other publications

1. **A. Shelemin**, A. Choukourov, J. Kousal, D. Slavínská, H. Biederman, *$TiO_{2-x}N_x$ nanoparticles produced by atmospheric pressure DBD*, EU COST MP1101, Workshop on Atmospheric Plasma Processes and Sources, Bohinjska Bistrica, Slovenia, Jan 19th – 23th 2013, Oral presentation

2. **A. Shelemin**, A. Choukourov, J. Kousal, D. Slavinska, H. Biederman: *Deposition of nanoparticles in atmospheric pressure plasma*, 2nd German – Czech workshop on Nanoparticles from low temperature plasma and their applications, Prague, Czech Republic, 23-24 May 2014, Oral presentation

3. **A. Shelemin**, O. Kylián , A. Choukourov, J. Hanuš, D. Slavínská, H. Biederman: *Deposition of Al_xO_y nanoclusters by gas aggregation source*, 26th Symposium on Plasma Physics and Technology, Prague, Czech Republic, 16-19 June 2014, Poster

4. **A. Shelemin,** A. Choukourov, J. Kousal, D. Slavinska, H. Biederman, *Dielectric barrier discharge for deposition of highly porous TiO2 coatings*, 14th

International Conference on Plasma Surface Engineering, Garmisch-Partenkirchen, Germany, 15 – 19 September 2014, Poster

5. **A. Shelemin**, A. Choukourov, O. Kylián, J. Kousal, D. Slavínská and H. Biederman, *Production of $SiO_x(CH)$ nanoparticles with tuneable properties using gas aggregation cluster source*, 22nd International Symposium on Plasma Chemistry, Antwerp, Belgium, 5-10th of July 2015, Poster

6. **A. Shelemin**, H. Biederman, Charlie P. Stallard, Kevin Mc Donnell and Denis P. Dowling, *Deposition of amino-rich plasma polymer thin film by atmospheric pressure plasma jet*, Joint Conference of COST ACTIONS TD1208 "Electrical discharges with liquids for future applications" & MP1101 Biomedical Applications of Atmospheric Pressure Plasma Technology, Bertinoro, Italy, 13th-17th September 2015, Oral presentation

7. **A. Shelemin**, A. Choukourov, O. Kylian, J. Kousal, D. Slavinska, H. Biederman, *Production of $SiO_x(CH)$ nano-particles with tuneable properties using gas aggregation cluster source,* 3rd German-Czech workshop on "Nanoparticles from low temperature plasma and their application", Lubeck, Germany 19th/20th of May 2016, Oral presentation

8. **A. Shelemin**, D. Nikitin, A. Choukourov, O. Kylian, J. Kousal, D. Slavinska, H. Biederman, *Silicon-based plasma polymer nanoparticles deposited by means of a gas aggregation cluster source,* 16th Joint Vacuum Conference & 14th European Vacuum Conference, Portoroz, Slovenia, 6th-10th of June 2016, Oral presentation

9. **A. Shelemin**, P. Solar, J. Hanus, O. Kylian, O. Polonskyi, H. Biederman, *Plasma polymer nanoparticles and their application for fabrication of columnar films,* 15th International Conference on Plasma Surface Engineering, Garmisch-Partenkirchen, Germany, 12th – 16th of September 2016, Oral presentation

Conference abstracts and contributions

1. A. Kuzminova, A. Choukourov, **A. Shelemin**, O. Kylián, J. Hanuš, H. Biederman: *Effect of DBD plasma treatment on properties of poly(ethylene terephthalate) foils*, International Conference "Eco-sustainable Food Packaging Based on Polymer Nanomaterials", Roma, Italy, 26-28 February 2014
2. H. Biederman, O. Kylián, J. Hanuš, O. Polonskyi, A. Choukourov, **A. Shelemin**, A. Kuzminova, D. Slavinska, L. Hanykova: *Low pressure plasma coatings for food packaging*, International Conference "Eco-sustainable Food Packaging Based on Polymer Nanomaterials", Roma, Italy, 26-28 February 2014
3. M. Petr, O. Kylián, A. Kuzminova, J. Kratochvíl, J. Hanuš, P. Solař, T. Steinhartová, **A. Shelemin**, H. Biederman: *From Superhydrophilic to Superhydrophobic Surfaces by Plasma Polymerization*, 2nd German –Czech workshop on Nanoparticles from low temperature plasma and their applications, Prague, Czech Republic, 23-24 May 2014
4. **A. Shelemin**, A. Choukourov, J. Kousal, D. Slavinska, H. Biederman: *Deposition of nanoparticles in atmospheric pressure plasma*, 2nd German –Czech workshop on Nanoparticles from low temperature plasma and their applications, Prague, Czech Republic, 23-24 May 2014
5. O. Kylián, J. Kratochvíl, A. Kuzminova, T. Steinhartová, **A. Shelemin**, M. Petr, P. Solař, J. Hanuš, A. Choukourov, H. Biederman: *Nanoparticles, nanostructures and nanocomposites prepared by gas aggregation sources* , 2nd German –Czech workshop on Nanoparticles from low temperature plasma and their applications, Prague, Czech Republic, 23-24 May 2014
6. A. Kuzminova, J. Kratochvíl, **A. Shelemin**, O. Kylián , J. Beranová , H. Biederman : *Preparation of antibacterial silver containing nanocomposites*, 23rd Week of Doctoral Students, Prague, Czech Republic, 3-5 June 2014
7. **A. Shelemin**, O. Kylián, A. Choukourov, J. Hanuš, D. Slavínská, H. Biederman: *Al_xO_y nanoclusters prepared by means of gas aggregation cluster source*, 23rd Week of Doctoral Students, 3-5 June, Prague, Czech Republic
8. **A. Shelemin**, O. Kylián , A. Choukourov, J. Hanuš, D. Slavínská, H. Biederman: *Deposition of Al_xO_y nanoclusters by gas aggregation source*, 26th Symposium on Plasma Physics and Technology, Prague, Czech Republic, 16-19 June 2014

9. A. Kuzminova, O. Kylián, **A. Shelemin**, J. Hanuš, H. Biederman: *Plasma modification of polymeric foils by dielectric barrier discharge in air at atmospheric pressure*, 26th Symposium on Plasma Physics and Technology, Prague, Czech Republic, 16-19 June 2014
10. O. Kylián, J. Hanuš, M. Petr, A. Kuzminova, J. Kratochvíl, T. Steinhartova, **A. Shelemin**, H. Biederman: *Low pressure plasma method for fabrication of super-hydrophobic fluorine-free coatings*, 26th Symposium on Plasma Physics and Technology, Prague, Czech Republic, 16-19 June 2014
11. A. Kuzminova, J. Kousal, P. Kudrna, **A. Shelemin**, H. Biederman: *Treatment of nylon by dielectric barrier discharge in air*, ESCAMPIG XXII, Greifswald, Germany, 15-19 July 2014
12. A. Kuzminova, **A. Shelemin**, J. Hanus, O. Kylian, A. Choukourov, H. Biederman: *Treatment of polymeric foils by dielectric barrier discharge in air and its influence on their subsequent coating with silver*, 14th International Conference on Plasma Surface Engineering, Garmisch-Partenkirchen, Germany, 15 – 19 September 2014
13. O. Kylian, **A. Shelemin**, J. Kratochvil, A. Kuzminova, J. Hanus, A. Choukourov, H. Biederman: *From super-hydrophilic to super-hydrophobic surfaces using combination of PECVD with gas aggregation source of nanoparticles*, 14th International Conference on Plasma Surface Engineering, Garmisch-Partenkirchen, Germany, 15 – 19 September 2014
14. A. Shukurov, A. Serov, I. Melnichuk, **A. Shelemin**, A. Kuzminova, O. Kylián, J. Hanuš, J. Kousal, H. Biederman: *Nano-particles of fluorocarbon plasma polymer produced by an r. f. magnetron-based gas aggregation source*, 14th International Conference on Plasma Surface Engineering, Garmisch-Partenkirchen, Germany, 15 – 19 September 2014
15. **A. Shelemin**, A. Choukourov, J. Kousal, D. Slavinska, H. Biederman: *Dielectric barrier discharge for deposition of highly porous TiO2 coatings*, 14th International Conference on Plasma Surface Engineering, Garmisch-Partenkirchen, Germany, 15 – 19 September 2014
16. **A. Shelemin**, A. Choukourov, O. Kylian, J. Kousal, J. Hanus, D. Slavinska, H. Biederman: *Ti and TiO_x nanoparticles prepared by plasma based methods*, 13th European Vacuum Conference, Aveiro, Portugal, 8-12 September 2014

17. **A. Shelemin**, P. Solar, A. Choukourov, O. Kylian, D. Slavinska and H. Biederman, *Glancing angle deposition using plasma polymer nanoparticles,* 16th European Conference on Applications of Surface and Interface Analysis (ECASIA'15), Granada, Spain. September 28th - October 1st, 2015
18. J. Kousal, **A. Shelemin**, O. Kylián and H. Biederman, *In-situ ellipsometry of etching of thin films using low-temperature atmospheric plasma jet*, 16th European Conference on Applications of Surface and Interface Analysis (ECASIA'15), Granada, Spain. September 28th - October 1st, 2015
19. A. Shelemin, H. Biederman, Charlie P. Stallard, Kevin Mc Donnell and Denis P. Dowling, *Deposition of amino-rich plasma polymer thin film by atmospheric pressure plasma jet*, Joint Conference of COST ACTIONS TD1208 "Electrical discharges with liquids for future applications" & MP1101 Biomedical Applications of Atmospheric Pressure Plasma Technology, Bertinoro, Italy, 13th-17th September 2015
20. A. Shelemin, A. Shukurov, O. Kylián, J. Kousal, D. Slavínská and H. Biederman, *Production of SiOx(CH) nanoparticles with tuneable properties using gas aggregation cluster source*, 22nd International Symposium on Plasma Chemistry, Antwerp, Belgium, 5-10th of July 2015
21. A. Shelemin, P. Solar, A. Choukourov, O. Kylian, D. Slavinska and H. Biederman, *Glancing angle deposition using plasma polymer nanoparticles, 16th European Conference on Applications of Surface and Interface Analysis*, Conference on Applications of Surface and Interface Analysis (ECASIA'15), Granada, Spain, September 28th - October 1st 2015
22. J. Kousal, A. Shelemin, O. Kylián and H. Biederman, *In-situ ellipsometry of etching of thin films using low-temperature atmospheric plasma jet*, 16th European Conference on Applications of Surface and Interface Analysis (ECASIA'15), Granada, Spain. September 28th - October 1st 2015
23. A. Shukurov, I. Melnichuk, A. Shelemin, P. Solař, J. Hanuš, D. Slavínská and H. Biederman, *Nano-granular titanium films overcoated-impregnated with C:H plasma polymer*, 22nd International Symposium on Plasma Chemistry, Antwerp, Belgium, 5-10 July 2015
24. Marta Vandrovcova, A. Kuzminova, O. Kylian, A. Choukourov, A. Shelemin, D, Slavinska, L. Bacakova, H. Biederman: *The influence of plasma treated polymer*

on cell growth, 2015 EMN Biomaterials Meeting, Beijing, China, 10-13 April 2015

25. O.Kylián, A. Kuzminova, M. Vandrovcová, A. Choukourov, A. Shelemin, D. Slavínská, L. Bačáková, H. Biederman: *Treatment of poly(ethylene terephthalate) foils by atmospheric pressure air dielectric barrier discharge and its influence on cell growth*, 22nd International Symposium on Plasma Chemistry, Antwerp, Belgium, 5-10 July 2015
26. A. Kuzminova, J. Hanus, A. Shelemin, O. Kylian and H. Biederman, *Fabrication of metal oxide nanoparticles using gas aggregation source combined with an auxiliary oxygen RF plasma*, 19th International Summer School on Vacuum, Electron and Ion Technologies, Sozopol, Bulgaria, 21 − 25 September 2015
27. O. Kylián, A. Kuzminova, M. Vandrovcová, MMM. Bilek, A. Shelemin, J. Hanuš, A. Choukourov, L. Bačáková, D. Slavínská, H. Biederman: *Atmospheric pressure plasma treatments for biomedical applications*, Bioplasmas and Plasmas with Liquids, Bertinoro, Italy, 13-16 September 2015
28. M. Petr, A. Kuzminova, A. Shelemin, J. Hanus, P. Solar, O. Kylian, H. Biederman: *Super-hydrophobic and super-hydrophilic nanocomposite films*, 20th International Colloquium on Plasma Processes, Saint-Etienne, France, 1-5 June 2015
29. **A. Shelemin**, P. Solar, A. Choukourov, O. Kylián, I. Khalakhan, D. Slavínská, H. Biederman, *Application of plasma polymer nanoparticles for biomimetic coatings*, 15th International Conference on Plasma Surface Engineering, Garmisch-Partenkirchen, Germany, 12th – 16th of September 2016
30. O. Kylian, **A. Shelemin**, J. Kousal, J. Hanus, M. Vaidulych, H. Biederman, *Etching of biomolecules and polymers by low-temperature atmospheric pressure plasma jet investigated by in-situ ellipsometry*, 15th International Conference on Plasma Surface Engineering, Garmisch-Partenkirchen, Germany, 12th – 16th of September 2016

AUTHOR'S CONTRIBUTION

The author performed the installation and the modification of the the experimental arrangements used in this work. The author ran the experiments, optimized the deposition processes and prepared the samples. The author performed the diagnostic of plasma by OES and characterized the samples by XPS, FTIR, ellipsometry, and water contact angle measurements. The author is grateful to Mgr. Ivan Khalakhan, PhD for SEM measurements; RNDr. Jaroslav Kousal, PhD for help with analysis of the ellipsometric data; RNDr. Doc. Ondrej Kylian, PhD for help with optical emission spectra processing; Doc. Ing. Andrei Choukorov, PhD for assistance with AFM measurements.